

Cover Page



Universiteit Leiden



The handle <http://hdl.handle.net/1887/37175> holds various files of this Leiden University dissertation

Author: Harkes, Rolf

Title: Quantitative super-resolution microscopy

Issue Date: 2016-01-13

Quantitative Super-Resolution Microscopy

PROEFSCHRIFT

Ter verkrijging van
de graad van Doctor aan de Universiteit Leiden,
op gezag van Rector Magnificus prof. mr. C.J.J.M. Stolker,
volgens besluit van het College voor Promoties
te verdedigen op woensdag 13 januari 2016
klokke 11.15 uur

door

Rolf Harkes

geboren te Wageningen
in 1986

Promotor: Prof. dr. T. Schmidt
Promotiecommissie: Dr. G.A. Blab (Universiteit Utrecht)
Prof. dr. A. Diaspro (IIT, Genova, Italië)
Prof. dr. V. Subramaniam (Vrije Universiteit)
Prof. dr. E.R. Eliel
Prof. dr. A.J. Koster
Dr. ir. S.J.T. van Noort
Prof. dr. M.A.G.J. Orrit

© Rolf Harkes. All rights reserved.

Cover front: 3D dSTORM image of GFAP in Astrocyte

Cover back: Optical setup used for super-resolution imaging

Casimir PhD Series, Delft-Leiden, 2015-35

ISBN 978-90-8593-241-3

An electronic version of this thesis can be found at

<https://openaccess.leidenuniv.nl>

Het onderzoek beschreven in dit proefschrift is onderdeel van het wetenschappelijke programma van de Stichting voor Fundamenteel Onderzoek der Materie (FOM), die financieel wordt gesteund door de Nederlandse organisatie voor Wetenschappelijk Onderzoek (NWO).

“The only acceptable point of view appears to be the one that recognizes both sides of reality: the quantitative and the qualitative.”

Wolfgang Pauli -Writings on Physics and Philosophy-

Dedicated to Sietske Froukje Harkes-Idzinga

TABLE OF CONTENT

1. INTRODUCTION INTO SUPER-RESOLUTION

MICROSCOPY	1
1.1 Theory of microscopy	2
1.2 Super-resolution microscopy techniques	4
1.2.1 Structured illumination.....	4
1.2.2 Near-field scanning microscopy	5
1.2.3 Fluorescence	6
1.2.4 Stimulated emission depletion	6
1.3 Single molecule fluorescence	8
1.3.1 Photoactivatable fluorescent proteins	8
1.3.2 PALM STORM and fPALM.....	9
1.3.3 dSTORM	10
1.3.4 3D SMLM	11
1.4 Comparison between imaging techniques	14
1.5 Quantification of single molecule data	15
1.5.1 Nyquist-Shannon sampling theorem	15
1.5.2 Image construction	18
1.5.3 Stoichiometry and multiple detections	19
1.6 Outline of this thesis	21
1.7 References	23

2. SINGLE MOLECULE STUDY OF RAS MEMBRANE

DOMAINS REVEALS DYNAMIC BEHAVIOR	25
2.1 Introduction	26
2.2 Materials and methods	28
2.2.1 Microscope.....	28
2.2.2 Correction for double detections	28
2.2.3 Cell culture and transfection	29
2.2.4 Analysis software.....	29
2.2.5 Ripley	29
2.2.6 Bootstrapping and automatic selection	30
2.2.7 Simulation of cluster diffusion.....	30
2.3 Results	31
2.3.1 Imaging of H-CAAX in fixed COS1 cells	31
2.3.2 Imaging of H-CAAX in living COS1 cells.....	35
2.4 Discussion	42

2.5 Outlook	43
2.6 References	45
2.7 Supplementary figures	47

3. 3D DIFFUSION MEASUREMENTS OF THE GLUCOCORTICOID RECEPTOR **49**

3.1 Introduction	49
3.2 Methods	51
3.2.1 Cell culture	51
3.2.2 Single molecule imaging.....	51
3.2.3 Particle image correlation spectroscopy (PICS) analysis	52
3.2.4 Depth of field calibration	53
3.3 Results	54
3.3.1 Analytical solution for correction of fraction size in 3D diffusion with limited detection volume.....	54
3.3.2 Validation of the correction by simulations.....	57
3.3.3 Validation of the correction using experimental data	58
3.4 Conclusion	62
3.5 References	64

4. DIRECT OBSERVATION OF A-SYNUCLEIN AMYLOID AGGREGATES **67**

4.1 Introduction	68
4.2 Materials and methods	70
4.2.1 Preparation of labeled α syn fibrillar seeds	70
4.2.2 Cell culture	70
4.2.3 Atomic force microscopy (AFM)	70
4.2.4 Co-localization experiments with lysosomes.....	71
4.2.5 dSTORM experiments and data analysis.....	71
4.3 Results and discussion	74
4.3.1 Super-resolution imaging of in vitro α syn fibrils	74
4.3.2 Internalization of extracellular α syn fibrils into neuronal cells	77
4.4 References	82
4.5 Supplementary figures	84

5. FORCE SENSING AND QUANTITATIVE dSTORM ON SIGNAL TRANSDUCTION PROTEINS	85
5.1 Introduction	86
5.2 Materials and methods	89
5.2.1 Cell culture	89
5.2.2 Sample preparation	89
5.2.3 dSTORM	90
5.2.4 Image analysis	91
5.3 Results	92
5.3.1 Analysis framework	92
5.3.2 Counting molecules in focal adhesions	98
5.4 Discussion	102
5.5 Outlook	102
5.6 References	103
5.7 Supplementary materials	105
5.7.1 Relation between variance and squared mean	105
5.7.2 Simulation for a combined statistics with secondary antibody labeling.....	105
5.7.3 Error propagation on squared distances	107
SUMMARY	109
SAMENVATTING	111
PUBLICATIONS	115
CURRICULUM VITAE	116
ACKNOWLEDGEMENTS	117

CHAPTER 1

INTRODUCTION INTO SUPER-RESOLUTION MICROSCOPY

Abstract

Since the discovery of red blood cells in 1674 and bacteria in 1676 mankind has been fascinated by the microscopic world of biology. With the naked eye the limit of what can be resolved is about 50 μm , the diameter of a thin human hair. Red blood cells are about 7 μm in diameter. To observe them, Antoni van Leeuwenhoek required a microscope. It can be safely stated that the microscope represents the key technology that enabled the field of biology to understand the functioning of living matter and life as such. This statement still holds for modern life-science research where continuing developments in microscopy push scientific discoveries. In what follows we present an overview of the current developments in super-resolution microscopy. Super-resolution microscopy has been developed over the last decade from a low-temperature technique into a ubiquitous biological tool. This tool enabled biologists to study details in live cells far beyond the diffraction limit, which was so-far only possible on fixed cells with electron microscopy. We will focus here on single molecule imaging methods and discuss the technique in detail.

1.1 THEORY OF MICROSCOPY

A microscope consists of two main elements. The objective lens that collects the light coming from a sample, and the imaging lens that projects this light onto a detector. In the first microscopes, like those used by Antoni van Leeuwenhoek, the imaging lens was the eye, and the image was projected on the retina. In our modern microscopes the imaging lens is a glass lens placed at a fixed distance from a digital camera.

The modern infinity-objectives consist of a collection of different lenses to correct for aberrations. They can be represented by a single positive lens with a short focal length of a few millimeters. (Fig. 1)

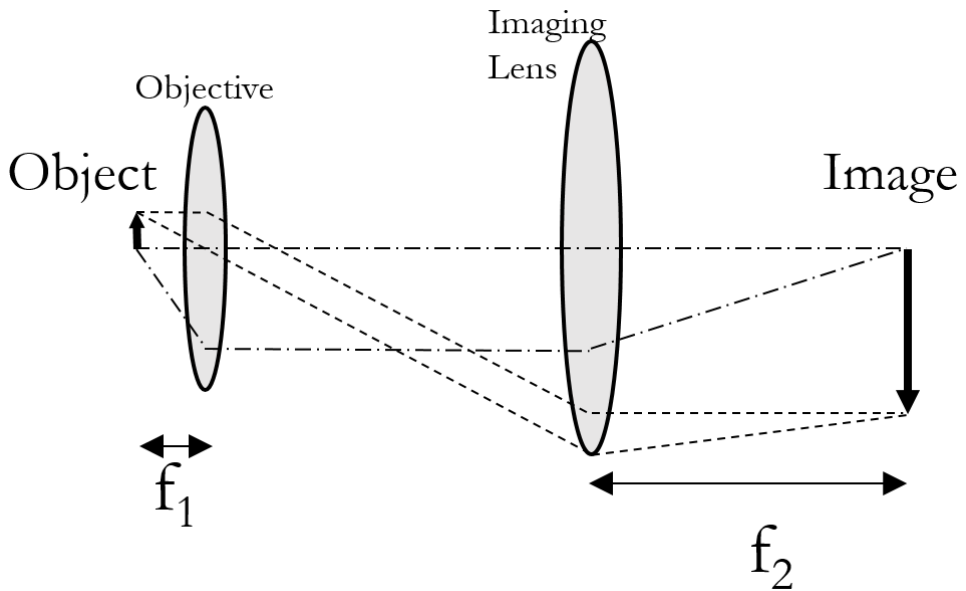


Figure 1: Schematic of a microscope. The magnification is given by f_2/f_1 . The infinity objective is represented by a single positive lens.

Light originating from a point source in the focal plane of the objective produces a spherical wave with the source at the center. Imaging this wave with the objective can be seen as sampling part of the spherical wave and converting this into a plane wave (Fig. 2).

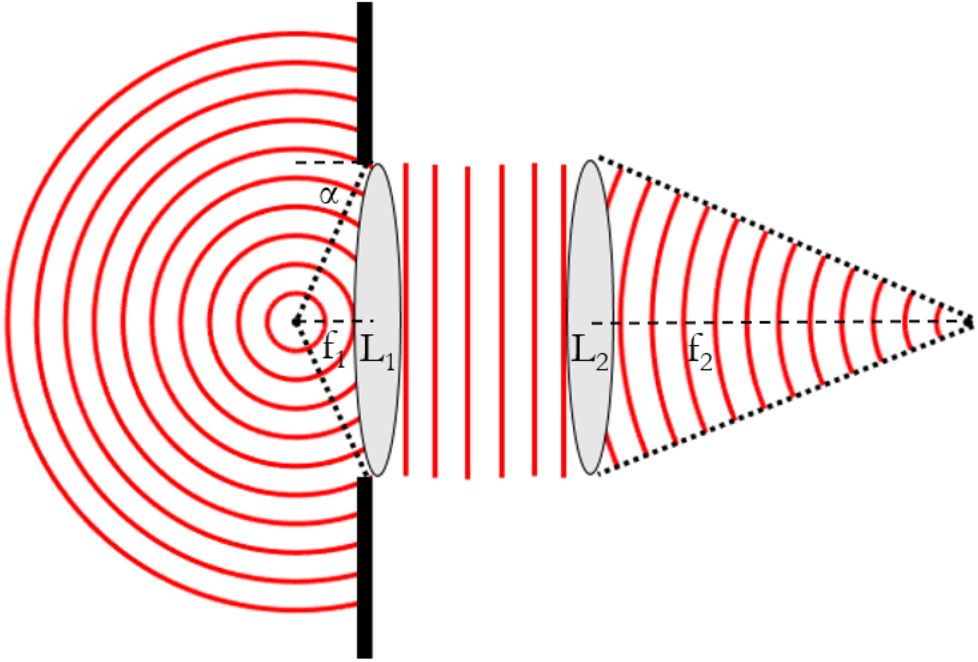


Figure 2: A part of the spherical wave emitted by a point source is captured by the objective lens (L_1) and converted into a planar wave. The imaging lens (L_2) transforms the planar wave back into a spherical wave that converges to a point. The magnification is given by $M=f_2/f_1$ and the solid angle of the spherical emission wave captured is $\Omega=2\pi(1-\cos(\alpha))$ steradian.

To image the light emitted by the point source, the imaging lens converts the plane wave back to a spherical wave that focusses the wave to a point. The waves can be seen as spherical caps with the center of the sphere at the base of the cone.

The lens operates as a circular aperture that gives rise to Fraunhofer diffraction, that generates an intensity pattern in the image plane described by an Airy function [1].

$$I(r) = I_0 \left(\frac{J_1 \left(\frac{2\pi}{M\lambda} \cdot r \cdot n \cdot \sin(\alpha) \right)}{\frac{2\pi}{M\lambda} \cdot r \cdot n \cdot \sin(\alpha)} \right)^2 \quad (1)$$

With J_1 the 1st-order Bessel function of the first kind, M the magnification, n the refractive index of the immersion medium, λ the wavelength of the incoming

1.2 Super-resolution microscopy techniques

light, α the maximum angle the objective can capture, and r the distance from the center of the image in the image plane (Fig. 2). This intensity pattern is commonly referred to as the point-spread-function (PSF) of the optical instrument.

Ernst Abbe stated in 1873 that two objects that are closer than the full-width-at-half-maximum (FWHM) of the PSF cannot be distinguished as individual objects. The half-maximum of the Bessel function, $J_1(x)$ is at $x=1.616$. The PSF calculated from eq. 1, with the magnification set to one, thus gives:

$$\begin{aligned} \frac{2\pi}{\lambda} r \cdot n \cdot \sin(\alpha) &= 2 \cdot 1.616 \\ r &= \frac{0.51 \cdot \lambda}{n \cdot \sin(\alpha)} \approx \frac{\lambda}{2NA} \end{aligned} \quad (2)$$

Equation 2 is commonly known as the Abbe limit. NA stands for the numerical aperture, a property of the objective, defined as $n \times \sin(\alpha)$. A modern objective can have a numerical aperture of as high as 1.45. Typical imaging wavelengths for visible light are around 500 nm which sets the diffraction limit to approximately 170 nm. Therefore objects separated by less than 170nm cannot be distinguished as individual objects by conventional microscopy.

1.2 SUPER-RESOLUTION MICROSCOPY TECHNIQUES

A super-resolution microscopy technique is an optical technique that can resolve structures beyond the diffraction limit of the emission wave.

1.2.1 Structured illumination

It was shown in 1963 by W. Lukosz and M. Marchand that the diffraction limit could be broken in one dimension by sacrificing resolution in the other dimension [2] By applying a grating to both the illumination and the detection path the frequency space that the microscope can explore is changed from circular to ellipsoid. They showed from the perspective of information theory that this could double the obtainable resolution of a microscope.

This idea was further explored in the nineties when the Wilson and the Gustafsson labs used Moiré-interference to directly create the grating in the illumination [3,4]. They expanded the grating to the third dimension to enhance the resolution. This resulted in a 3D super-resolution technique named Structured Illumination Microscopy (SIM). By changing the pattern in time and

imaging a sample multiple times a resolution increase of twofold is possible in each dimension as compared to normal diffraction-limited microscopy.

1.2.2 Near-field scanning microscopy

As D.W.Pohl pointed out, the diffraction limit does not play a role near to the sample. [5] A medical stethoscope can localize the heart better than 10 cm by listening to sound waves that have a wavelength of 100 m. The increased resolution is solely obtained by the narrow aperture of the stethoscope, which is at a small distance to the heart. This near-field approach can be adapted for the use of electromagnetic waves. The requirements stay the same: the aperture and the distance to the sample must be small in comparison to the wavelength of the wave. When the distance becomes large, Fraunhofer diffraction would apply and create a diffraction-limited spot in what is called the far field.

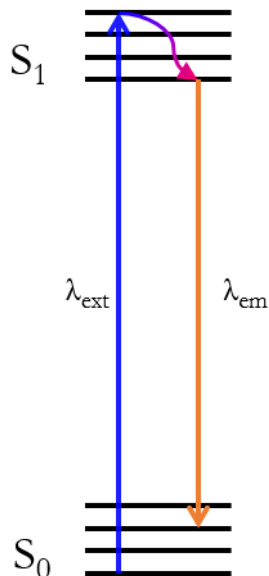
In 1972 E.A.Ash and G.Nicholls showed near-field scanning microscopy for the first time using 3 cm radio waves. [6] By scanning an aperture of 1.5 mm over a fine aluminum grating deposited on glass, they could resolve gaps of the grating that were spaced by only 0.5 mm. Hence, they showed a resolution that is 60 times below the wavelength.

Extending this technique to the visible spectrum required microfabrication of apertures out of opaque material, and micro positioning of the sample. From 1983 E.Betzig and A.Lewis worked on the development of such a system. In 1987 they presented super-resolution imaging with near-field scanning optical microscopy (NSOM) [7]. The device positioned a 150 nm diameter aperture several nanometers from the sample. A xenon arc lamp was used to illuminate the aperture. By scanning an aluminum grating on a silicon nitride membrane they resolved lines of widths 250 nm that were separated by 250 nm.

1.2 Super-resolution microscopy techniques

1.2.3 Fluorescence

The next super-resolution techniques apply specifically to fluorescence. In fluorescence, the orbital electrons of a molecule are electronically excited by light at a wavelength λ_{ex} . This excites the electron from its singlet ground state (S_0) into a singlet excited state (S_1). The excited state undergoes vibrational relaxation with lifetimes in the order of $1-5 \cdot 10^{-12}$ seconds. After relaxation the electron falls back to the singlet ground state. There are different ways of relaxation, it happens either by emitting a photon or by non-radiative relaxation. The lifetime of radiative decay (τ_f) is typically in the order of $1-5 \cdot 10^{-9}$ seconds depending on the non-radiative decay rate.



$$\tau_f = \frac{1}{\sum k - k_{nr}} \quad (3)$$

The emitted photon has a lower energy than the photon that excited the molecule. This lower wavelength λ_{em} permits a background-free detection of the signal by filtering the emission with a low-pass filter.

1.2.4 Stimulated emission depletion

In 1994 Stefan Hell and Jan Wichmann proposed a technique they called stimulated emission depletion (STED) [8]. This technique would overcome the limits of near-field imaging by using what could be called an “optical aperture” to limit the illuminated volume. Fluorophores are excited using a focused, diffraction limited, Gaussian beam. Shortly thereafter, high intensity illumination of longer wavelength will introduce an alternative non-radiative decay rate. This forces the excited molecule back into the ground state by what is called stimulated emission. By using a doughnut-shaped depletion beam that overlaps with the Gaussian excitation beam the excited fluorescent molecules at the edges of the Gaussian beam are forced back into their ground state – those molecules stay dark. This process effectively limits the volume from which molecules can emit fluorescence.

The excited fluorophore needs to encounter a depletion photon within the time it is excited. The energy needed will be equal to the bandgap. This means the depletion beam intensity (I_s) must exceed the photon energy ($h \cdot f$) divided by the absorption cross-section (σ) and the time the fluorophore is in the excited state (τ_f).

$$I_s = \frac{hf}{\sigma\tau_f} \quad (4)$$

By increasing the intensity of the doughnut beam (I_m), the radius (r) of the area where a fluorophore will have radiative decay will get smaller. This enables the separation of fluorophores that are closer together than the Abbe limit. The formula for Abbe's diffraction limit rewrites into equation 5.

$$r = \frac{\lambda}{2NA\sqrt{1 + \frac{I_m}{I_s}}} \quad (5)$$

By scanning the small excitation volume over the sample a super-resolution image is built-up. In 2000 the group of Stefan Hell published results that show a twofold increase in resolution over normal diffraction-limited techniques [9]. By increasing the intensity of the depletion beam the excitation volume was decreased further and the resolution increased to 17 nm to-date. It should be noted that this increase of resolution comes at the cost of photodamage of the sample due to the high intensity depletion beam. The non-radiative pathway also strongly decreases the lifetime of fluorescent decay in the doughnut region. By measuring the arrival time of the emitted photons and setting a minimum time t_g for the photon arrival time, the volume that contributes to the signal could be further decreased without having to increase the intensity of the depletion beam. This technique was published in 2011 and named time gated STED [10].

A different method that enables a decrease in the intensity of the depletion beam is reversible saturable optical fluorescence transitions microscopy, or RESOLFT microscopy [11]. In RESOLFT microscopy the doughnut-shaped depletion beam reversibly switches the fluorescent molecules into an off-state, so that emission only emerges from the center of the beam. Using switchable

1.3 Single molecule fluorescence

fluorescent molecules that switch at a low intensity enables a low-intensity depletion beam.

1.3 SINGLE MOLECULE FLUORESCENCE

Another technique that breaks the diffraction limit is based on the imaging of single molecules. In 1989 W.E. Moerner's lab at IBM detected the first individual molecules by measuring their absorption spectrum at cryogenic temperature [12]. A tunable laser illuminated the sample and the detector measured the total absorption. By spectrum analysis they could show that the signal originated from a single molecule. At the same time Orrit and Bernard measured individual fluorescent molecules by their excitation spectrum, which gave a much higher signal-to-noise ratio [13].

In 1995 Takashi Funatsu et al. showed the possibility of imaging the emission of individual fluorescent molecules using a sensitive, cooled CCD detector and excitation by total internal reflection. With this system they could observe single ATP/ADP turnovers by kinesin motors [14]. A year later T. Schmidt et al. imaged individual labeled lipid molecules in an artificial lipid bilayer [15]. They stated that the individual fluorophores would act as point sources and produce a PSF on the camera. By fitting the PSF with a 2D-Gaussian the position of the molecule could be obtained to a much higher resolution than the diffraction limit. In their experiment they showed a positional accuracy of 30 nm at a temporal resolution of 7 ms. This allowed determination of the diffusion constant of individual lipids [15]. Since then this technique was used to determine the diffusion constant of many different molecules in artificial systems, in cells and even in an animal, but it was limited to a low density of fluorophores. At high densities the individual PSF's would overlap, making single molecule microscopy impossible.

1.3.1 Photoactivatable fluorescent proteins

An important discovery that enabled single molecule imaging was the photoactivatable fluorescent protein (PA-FP) named Kaede in 2002 [16]. When searching for new fluorescent proteins in the stony coral *Trachyphyllia geoffroyi*, an aliquot of a sample was accidentally left on the windowsill. The next day the Miyawaki group found it had turned from green to red. A more detailed investigation showed this photo-convertible protein had a native fluorescent state with an absorption and emission spectrum in the green wavelength region,

but the spectra switched to the red wavelengths when illuminated with near UV light (Fig. 3).

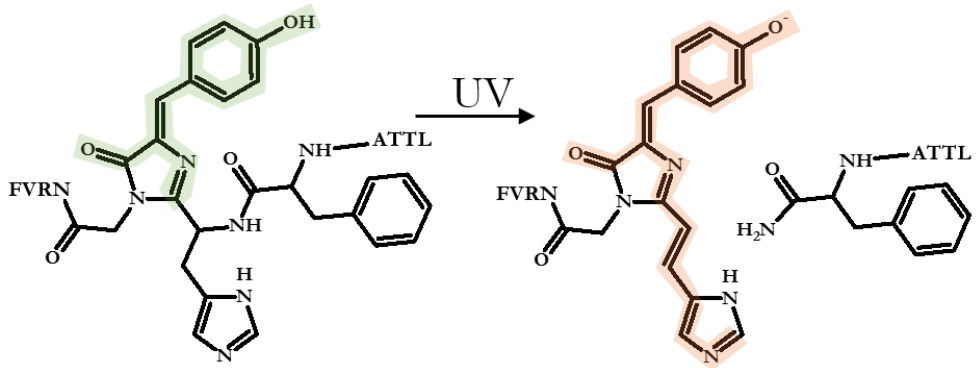


Figure 3: Structure of the chromophore of the PA-FP Kaede [17]. Phe61-His62-Tyr63-Gly64 are drawn with their surrounding amino acids LTTA-FHYG-NRVF. When illuminated with UV light the bond between phenylalanine-61 and histidine-62 is broken and the protein is converted from a green to a red state.

In 2002 the group of J. Lippincott-Schwartz genetically engineered a variant of GFP that could be photoactivated using 413 nm light to increase its fluorescence 100 times [18]

1.3.2 PALM STORM and fPALM

The necessity of spatially well separated point spread functions limited the maximum density of fluorescent molecules. Therefore single molecule detection could not result in high resolution images. The sampling density was too low to image enough single molecules in a small region to resolve small structures. This limit in sampling density is equivalent to the Nyquist-theorem as discussed later in this chapter.

By illuminating PA-FPs with low intensity UV light only a few of them will be converted. These can be localized and will subsequently bleach. This process can continue until all proteins have been converted and localized, enabling a high sampling density. Three groups independently utilized this method in 2006.

1.3 Single molecule fluorescence

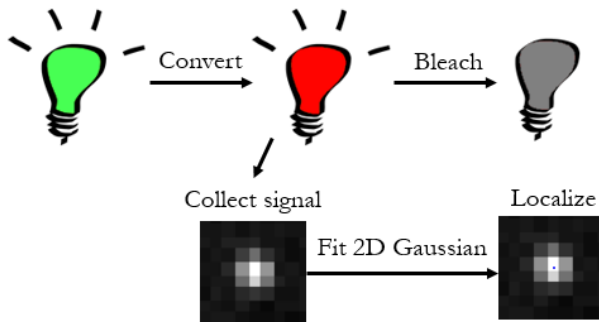


Figure 4: Schematic representation of PALM. A small population of the green form of a PA-FP is converted by low intensity UV light into the red form. These molecules are excited and the fluorescence signal is collected on a camera. By fitting a 2D Gaussian the location of the PA-FP is obtained. By repeating the cycle all PA-FP's can be localized.

Betzig et al. attached PA-FP Kaede to the lysosomal transmembrane protein CD63. By expressing this construct in cells they obtained a super-resolution image of CD63. They termed the technique photoactivated localization microscopy (PALM) [19]. S. Hess et al. localized PA-GFP on glass coverslips and termed the technique Fluorescence photoactivation localization microscopy (FPALM) [20]. The Zhuang group did not use fluorescent proteins, but used the dye Cy5. Cy5 is a fluorescent dye that can be switched between a fluorescent and a dark state by light of different wavelengths in the presence of another Cy-fluorophore in its vicinity [21]. They termed the technique stochastic optical reconstruction microscopy (STORM). With STORM they could separate two dyes on double stranded DNA that were 34 nm apart [22].

1.3.3 dSTORM

In 2008 the group of Sauer showed that the switching properties of conventional dye molecules were altered by adding reducing, thiol-containing compounds to the solution [23]. When excited, the fluorophores can undergo intersystem crossing, placing them in an excited triplet state. In this state the fluorophore can react with the reducing thiol and transfer into a long-lived dark state that is decoupled from the excitation scheme. This greatly reduces the number of molecules that are visible at the same time. The non-fluorescent fluorophores in the reduced triplet state can return to the fluorescent state by a reaction with oxygen. Changing the oxygen concentration and the thiol concentration will hence change the switching dynamics of the dye molecule. This made it possible

to use conventional antibody labeling techniques for super-resolution imaging. This technique is commonly known as direct STORM, or dSTORM.

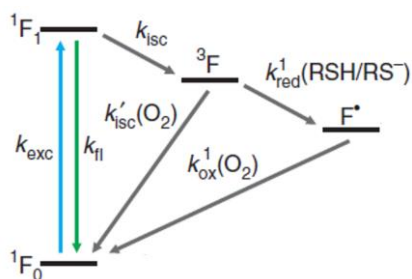


Figure 5: The energy diagram for dSTORM imaging [24]. When excited, the fluorescent dye molecule goes from the singlet ground state (1F_0) to the singlet excited state (1F_1), and falls back while emitting a photon. From the excited singlet state it can also undergo intersystem crossing (isc) to the excited triplet state (3F). By reacting with a reducing thiol (RSH) it can then go into a long lived dark state (F^\bullet). By changing the thiol and oxygen concentration the fraction of molecules in the dark state can be altered.

PALM, fPALM, STORM, and dSTORM can be summarized under the term single molecule localization microscopy (SMLM). Effectively all SMLM techniques make use of a small population of fluorophores that is in a visible “on-state” where they can be localized. The majority of fluorophores is stored in a non-visible “off-state” from where they stochastically return to the “on-state” for detection.

1.3.4 3D SMLM

The above mentioned methods permit to localize individual molecules at a precision down to about 10 nm. Their on-axis position however is inaccessible. The axial position could be obtained by realizing that the point spread function (PSF) is symmetrical in the z-direction. When the point source moves out of focus the size of its image will increase. Several ways to adapt the optical setup to enable 3D localization of a point source were presented since 1998.

Bi-plane imaging

In 1998 van Oijen et al. showed that they could resolve the axial position of a single pentacene molecule with 100 nm accuracy [25]. This was done by scanning the focal plane over the molecule and recording the PSF. The focal plane was scanned by moving the camera. By fitting the width of the PSF with respect to the camera position, the minimum can be obtained. This yields the axial position of the molecule.

1.3 Single molecule fluorescence

In 2004 the group of R.J.Ober enhanced the technique by using a 50/50 beam splitter in the emission path [26]. The two emission paths were imaged on two camera's at different focal planes. This allowed for simultaneous bi-plane imaging. In 2007 they showed this technique was applicable for 3D particle tracking [27]. However, splitting of the signal means the signal to noise is half of the 2D situation, reducing the positional accuracy in x and y by a factor $\sqrt{2}$. By aligning the two images the two fits can be combined and, depending on the precision of the alignment, part of the loss in positional accuracy can be recovered.

The group of Bewersdorf applied the bi-plane technique in 2008 to SMLM [28], naming it BP-FPALM.

Astigmatism

A cylindrical lens focusses the light only in one axis, by effectively shifting the focus of the light in one axis to a different plane. When a point source is in focus on one axis, it will be out of focus on the other axis and the PSF will be elongated in that direction. This mechanism has been the basis of focus-control in CD-players [29]. In 1994 the Verkman group published tracking of fluorescent particles in 3D using a cylindrical lens in the imaging path [30]. When the fluorophore is equally out of focus in both directions it appears round. By aligning the cylindrical lens with the camera the 3D information can be obtained by fitting a 2D Gaussian with a different width in x and y. In 2007 the technique was used to track quantum dots in living cells by Holtzer et. al. [31]. The group of Zhuang developed 3D STORM imaging using this technique in 2008 [32]. Since the signal of a single fluorophore is spread out over a larger area the signal to noise per pixel drops and the positional accuracy in x and y is reduced.

Double-helix point spread function

In 2008 Pavani and Piestun showed that the shape of the PSF can be altered using a phase-only spatial light modulator in the imaging path [33]. They engineered a double helix PSF where the relative orientation of the two points contains the z-information (see Fig.6)

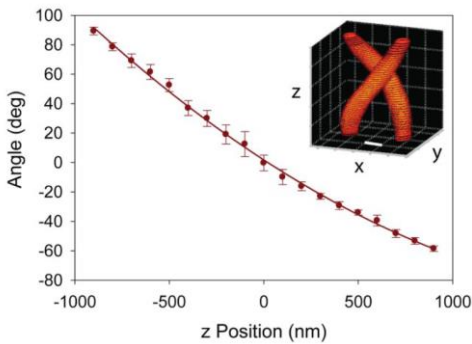


Figure 6: The helical point spread function from [34] The angle between the two detected points of the PSF changes when the axial position of the fluorophore changes.

The x-y position is found by interpolating the two points. In 2009 the group of Moerner showed the application to SMLM [34] and has developed the technique since. The technique needs a method to alter the PSF and will lose photons while doing this, decreasing the resolution. However, by using a custom designed phase plate the losses can be minimized. The double-helix PSF has the advantage of being accurate over a large axial region, but it requires a different fitting algorithm to retrieve x-y-z information.

Selective plane illumination

The adapted PSF allows 3D imaging of samples and enables the acquisition of data from the entire sample. When the sample is thicker than the axial length of the adapted PSF, the objective is moved to image different planes. By adding the movement to the found z-position a thick sample can still be imaged.

However, the planes that are not being imaged still receive excitation light, since the collimated beam from the objective illuminates the entire column. This means that fluorophores that are out of the imaging plane are photobleached. To overcome this problem Zanicchi et al. introduced a second objective to selectively illuminate only the focal plane of the imaging objective [35]. By moving the illuminating objective with the imaging objective only the molecules that are in focus are excited. This enables super-resolution imaging with minimal photo bleaching in three dimensions. They named this technique “individual molecule localization – selective plane illumination microscopy” IML-SPIM.

1.4 Comparison between imaging techniques

iPALM

An entirely different approach to explore the 3rd dimension was published in 2009 by the group of H.F. Hess [36]. By using a second objective the light emitted by a single fluorophore is split into two beam paths. These are combined in a 3-way interferometer that splits the signal onto three camera's. The ratio between the three signals is a measure for the axial position of the fluorophore. This enables determination of the axial position to 4 nm positional accuracy and 10 nm lateral for signal of 1500 photons/frame.

1.4 COMPARISON BETWEEN IMAGING TECHNIQUES

To compare super-resolution imaging techniques there are a few parameters that can be compared. Resolution, measurement speed, photo damage, and 3D-imaging possibility.

Structured illumination has the lowest resolution of the mentioned techniques. The maximum improvement with respect to confocal microscopy is a factor of $\sqrt{2}$. The measurement speed is very fast, since only a few images need to be taken at different structured illumination conditions. Modern optical elements can change the structured illumination conditions very rapidly. The photo damage will not be higher than for normal confocal microscopy. The technique uses standard optical techniques, hence it can be directly applied to any fluorescent sample.

NSOM can reach very high resolutions by decreasing the size of the aperture. However the detection efficiency decreases rapidly with decreasing aperture and in practice the limit is at 10-20 nm. Another drawback is the need to stay in the near field. This limits the detection to just a few nanometers from the tip, making it essentially a 2D technique.

STED has shown a resolution increase of 10-20 with respect to the diffraction limit. Since this technique uses optical scanning that is already developed for scanning confocal microscopy it can be applied to any fluorescent sample. The measurement speed scales with the number of pixels. With modern resonant scanning mirrors the frame rate can be very high. By moving the sample with respect to the objective and scanning again, the third dimension can also be imaged in slices. However, the high intensity of the depletion-beam makes it unsuitable for live cell imaging. RESOLFT has tackled this problem, but requires preparation of the sample with a suitable fluorophore.

SMLM can also improve the resolution by a factor of 10-20 with respect to the diffraction limit. However, because many fluorophores need to be detected, the measurement speed is limited to a few frames per minute. High excitation intensities make it a challenging technique when applied to live cells. The technique also requires preparation of the sample with photoactivatable proteins or photo switchable dyes. 3D-imaging is possible by various methods that adapt the point spread function of the optical setup. dSTORM works with conventional dyes, but requires switching buffer conditions that are often detrimental to cells. Adapting the buffer conditions to keep the cells alive and the dye molecules switching is a challenge.

1.5 QUANTIFICATION OF SINGLE MOLECULE DATA

The images acquired by single molecule localization microscopy (SMLM) are constructed from the determined location of many single molecules. This makes them fundamentally different from normal microscopy images, where the image is constructed from the signal of the molecules.

1.5.1 Nyquist-Shannon sampling theorem

To resolve a structure it is necessary to not only have a high positional accuracy, but also have a sufficient high sampling density. This is analogous to the Nyquist-Shannon sampling theorem for one-dimensional signals. It states that to resolve a certain frequency f_s the sampling frequency must be at least $2 f_s$. (see Fig. 7a)

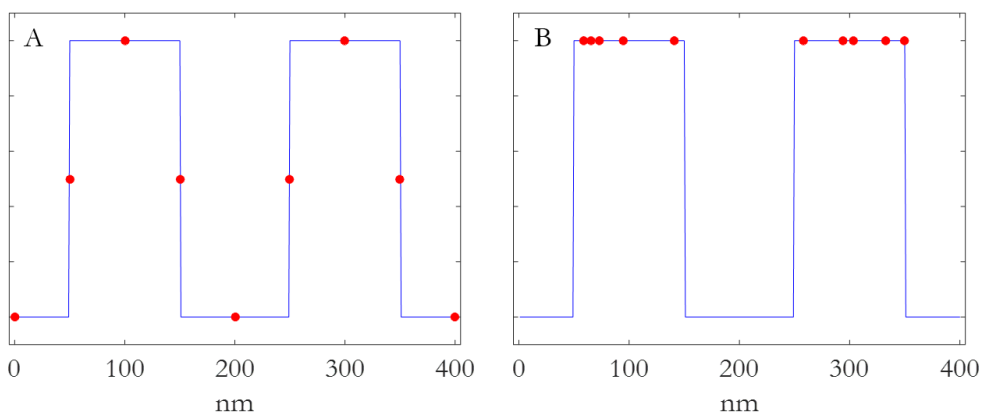


Figure 7: Sampling of a structure. A) Nyquist sampling, to resolve two 100nm structures that are 100nm apart, the sampling period needs to be smaller than 50nm.

B) Localization microscopy has no fixed sampling and only localizes the structure itself.

1.5 Quantification of single molecule data

Single molecule localization differs from normal sampling because there is no fixed sampling frequency and the detections are only on the structure itself (see Fig.7b). Therefore the Nyquist-Shannon sampling theorem is rewritten to say that the shortest detectable spatial period (T) that can still be resolved must be twice the mean molecular separation between neighbors (see Eq. 6) [37].

$$T = \frac{2}{n} \sum_{i=1}^n \text{Min}_j \left\{ (x_i - x_j)^2 \right\}^{1/2} \quad (6)$$

To resolve a 10nm structure (r) on a line, the localizations must have a mean molecular separation between neighbors of 5nm. Therefore the minimum sampling density (ρ) must be $200 \mu\text{m}^{-1}$. This scales with the imaging dimension (D) (see Eq. 7).

$$\rho = \left(\frac{2}{r} \right)^D \quad (7)$$

However, overlapping PSFs of individual molecules cannot be resolved. Therefore two detections within the distance of one PSF must be separated in time. In the optimal situation where reappearance of the molecule is random and molecules are bleached after one detection. The highest efficiency is obtained when p is $0.2/\sqrt{n}$ with p the probability of each molecule to appear. (see Fig. 8) On average there is one detection every six frames.

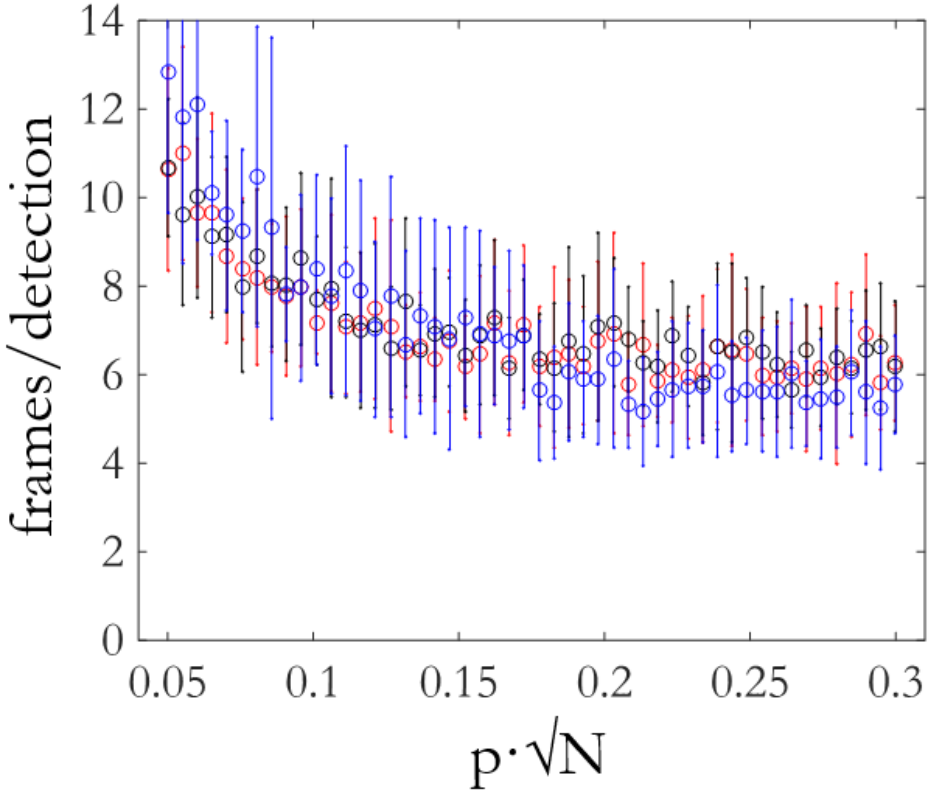


Figure 8: Simulation result of $N=100$ (blue), 200 (red), 300 (black), molecules in a PSF with different probability of appearing. For a low probability the number of frames required becomes high. At a high probability only a few frames are required to bleach all molecules. The optimal number of frames per detections depends on the probability of a molecule appearing and the number of molecules in a PSF. A probability of $0.2/\sqrt{N}$ gives the optimal value for the number of required frames per detection. However, at this value many molecules will be discarded since they appear at the same time in the PSF.

This causes a fundamental tradeoff in single molecule imaging. The spatial resolution gain comes at a temporal resolution loss. Equation 8 shows this tradeoff with t the minimal time needed, f the framerate r the resolution, and PSF the distance, surface or volume of the PSF.

$$t = \frac{6 \cdot \text{PSF}}{f} \left(\frac{2}{r}\right)^D \quad (8)$$

1.5 Quantification of single molecule data

This would mean to obtain an image with a resolution of 20nm in 2D with a 100Hz camera and a PSF with a FWHM of 240nm takes at least 27 seconds of imaging.

1.5.2 Image construction

To obtain an image from localization data the locations must be mapped onto a pixelated area. This can be done by quantizing the localizations to the pixels of the image. This is also called binning or bucketing. However, the resulting image is depending on the chosen pixel size. When the pixels are large with respect to the structure the resolution will be greatly reduced. When the pixels are small with respect to the sampling density the structure can become binary and discontinuous. (Fig.9)

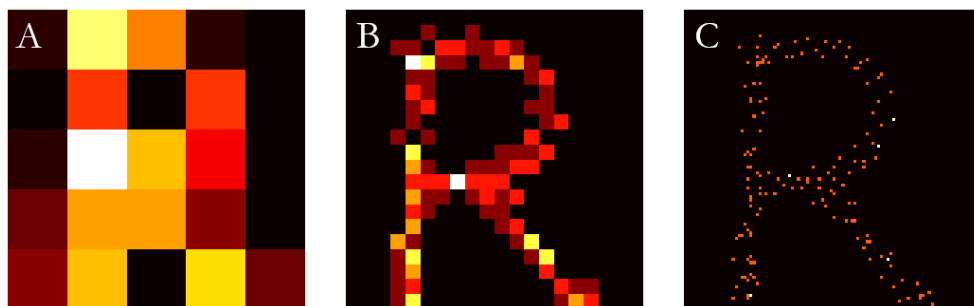


Figure 9: Three representations of the same set of 150 localizations with different size pixels.
 $A= 5 \times 5$, $B=20 \times 20$, $C=100 \times 100$

Another possibility is to construct a probability density map. The 2D-Gaussian fit to the image data (Fig.10) gives a mean and standard deviation for the value of the center of the Gaussian. The probability density of the center position can be described with a 2D-Gaussian. By summation of all probability densities the probability density to find a molecule within an area can be calculated. (Fig. 10) This has the benefit of incorporating the fitting accuracy in the image, preventing a false sense of accuracy.

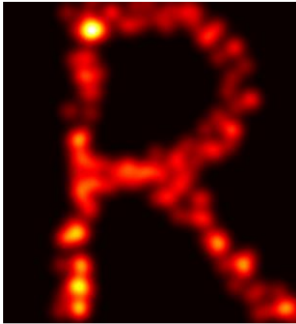


Figure 10: Probability density map of the 150 localizations from figure 5.

This effect is seen when comparing figure 9c with figure 10. Figure 9c appears to pinpoint the position of molecules; from figure 10 it is clear the position of the molecules was not determined with absolute accuracy. However, for large datasets the calculation and summation of 2D Gaussians can be time consuming.

1.5.3 Stoichiometry and multiple detections

In biology it is often important to know the exact number of proteins in a complex to understand more about the underlying mechanisms. The relative amount of a protein in a complex is called stoichiometry. SMLM would seem to be an ideal tool to determine the number of molecules present in a sample. After localizing all molecules one could determine the stoichiometry just by counting. However, the technique suffers from multiple detections of the same molecule.

When a fluorescent molecule is in the visible state, the emission will be detected by a camera. The camera takes in the order of 60-200 frames per second. When the molecule is visible for a period longer than the exposure time of the camera, it will appear in multiple frames. The common solution to this problem is to group detections that happen in the same region of the image and either remove all but one, or combine them into a single detection. This requires a parameter Δr , the radius of the circle where a second detection is considered a re-appearance of the same molecule. Often this parameter is linked to the goodness of the 2D-Gaussian fit. When molecules can diffuse it is important to increase Δr to correct for double detections. A risk with this method is the exclusion of a second molecule that happens to be within Δr of a previous detection.

dSTORM

In dSTORM the fluorescent dye will undergo transitions between a fluorescent “on-state” and a non-fluorescent “off state” (Fig. 5). As a result the same

1.5 Quantification of single molecule data

molecule can be detected multiple times, with extended dark times in between detections. To correct for this, a second parameter can be introduced, Δt , for the maximum dark-time where a new detection within Δr is considered the same molecule. However, for some dyes these dark-times can be in the order of tens of seconds, requiring Δt become very large. It also increases the chance a second molecule is excluded which appears within Δr and Δt . This effect makes molecular counting in dSTORM difficult. (see Chapter 5 for more details)

PALM

In PALM the PA-FP is cleaved by UV light, converting it into a red state. The molecule is either in a red “on state” or a green “off state”. The difference is that once a PA-FP is converted to the red state it cannot return to the green state. It can go into a triplet darkstate, but this state is reactive and will often result in a destructive reaction with triplet oxygen in a cellular environment leading to photobleaching. To prevent a molecule to be detected again after a successful return from the triplet state, Δt can be chosen such that the chance of double detections is minimal. This value will depend e.g. on the oxygen concentration.

1.6 OUTLINE OF THIS THESIS

In this thesis we use SMLM to quantitatively investigate four different proteins that play an important role in cells. By localizing the proteins to sub-diffraction limited precision we analyzed parameters such as size, diffusive behavior and stoichiometry. To do so we had to develop strategies that allowed us to obtain quantitative data in a robust way.

In **chapter 2** we show the spatial distribution of different isoforms of the rat sarcoma (Ras) protein in order to quantify their collective diffusive behavior. The spatial distributions are measured using photoactivated localization microscopy on the PA-FP mEos2, genetically tagged to the Ras isoforms. By imaging fixed cells we observed membrane domains of 65 nm in size. In living cells we observe an increase in domain size to 150 nm. By simulating cluster diffusion we were able to understand our result. The data were consistent, assuming a diffusion constant for the domains of $5 \times 10^{-4} \mu\text{m}^2/\text{s}$.

In **chapter 3** we analyzed the 3D diffusive behavior using SMLM on yellow fluorescent protein (eYFP) fused to the glucocorticoid-hormone receptor. On activation of the receptor it translocates to the nucleus and is allowed to bind to specific target sites on DNA. Since we imaged only in a thin 2D-slice of the nucleus systematic errors in quantification of the diffusive behavior were introduced. We developed a method by which those errors are corrected for. We show that the receptor is present in two fractions, which are distinct in their diffusion constant of 0.67 and $0.043 \mu\text{m}^2/\text{s}$, respectively. Furthermore we show that there was no exchange between those two fractions on the timescale between 6.5 and 150 ms.

In **chapter 4** we imaged the spatial distribution of the protein α -synuclein in cells. We showed that small preaggregated fibers were taken up by cells within 24 hours. Unlike earlier predictions we could not find any aggregation of fibers occurring after cellular uptake. On the contrary we found that aggregates decreased in size over time presumably by lysosomal degradation.

In **chapter 5** we analyzed the stoichiometry in focal adhesion complexes using dSTORM. The stochastic blinking and labeling of proteins so-far prohibited any quantitative analysis of the number of proteins in such complexes. We here developed a methodology based on second order spatial correlations to extract the number of proteins from localization data without the need for a detailed knowledge about the photophysics and labeling statistics. We applied this

1.6 Outline of this thesis

methodology to relate the local force exertion by cells to the availability of proteins at this position. For the case of talin, one of the essential proteins in focal adhesions and a potential force regulator, we found an increase of cellular force of 100 pN/talin molecule.

1.7 REFERENCES

- [1] E. Hecht, *Hecht Optics*, Second (Addison-Wesley publishing company, 1987).
- [2] W Lukosz and M Marchand, *Journal of Modern Optics* **10**, 241 (1963).
- [3] M. A. Neil, R. Juskaitis, and T. Wilson, *Opt Lett* **22**, 1905 (1997).
- [4] M. G. Gustafsson, *Proc. Natl. Acad. Sci. U.S.A.* **102**, 13081 (2005).
- [5] Pohl, Denk, and Lanz, *Appl. Phys. Lett.* (1984).
- [6] E. A. Ash and G. Nicholls, *Nature* **237**, 510 (1972).
- [7] Betzig, Isaacson, and Lewis, *Applied Physics Letters* **51**, 2088 (1987).
- [8] S. W. Hell and J. Wichmann, *Opt Lett* **19**, 780 (1994).
- [9] TA Klar, S Jakobs, M Dyba, A Egner, and SW Hell, *Proceedings of the National Academy of Sciences of the United States of America* (2000).
- [10] G. Vicidomini, G. Moneron, K. Y. Han, V. Westphal, H. Ta, M. Reuss, J. Engelhardt, C. Eggeling, and S. W. Hell, *Nat. Methods* **8**, 571 (2011).
- [11] M. Hofmann, C. Eggeling, S. Jakobs, and S. W. Hell, *Proc. Natl. Acad. Sci. U.S.A.* **102**, 17565 (2005).
- [12] WE Moerner and Kador, *Phys. Rev. Lett.* **62**, 2535 (1989).
- [13] Orrit and Bernard, *Phys. Rev. Lett.* **65**, 2716 (1990).
- [14] T. Funatsu, Y. Harada, M. Tokunaga, K. Saito, and T. Yanagida, *Nature* **374**, 555 (1995).
- [15] T. Schmidt, G. J. Schütz, W. Baumgartner, H. J. Gruber, and H. Schindler, *Proc. Natl. Acad. Sci. U.S.A.* **93**, 2926 (1996).
- [16] R. Ando, H. Hama, M. Yamamoto-Hino, H. Mizuno, and A. Miyawaki, *Proc. Natl. Acad. Sci. U.S.A.* **99**, 12651 (2002).
- [17] H. Mizuno, T. K. Mal, K. I. Tong, R. Ando, T. Furuta, M. Ikura, and A. Miyawaki, *Mol. Cell* **12**, 1051 (2003).
- [18] G. H. Patterson and J. Lippincott-Schwartz, *Science* **297**, 1873 (2002).
- [19] E. Betzig, G. Patterson, R. Sougrat, W. Lindwasser, S. Olenych, J. Bonifacino, M. Davidson, J. Lippincott-Schwartz, and H. Hess, *Science* **313**, 1642 (2006).
- [20] ST Hess, T. Girirajan, and MD Mason, *Biophysical Journal* (2006).
- [21] M. Bates, T. R. Blosser, and X. Zhuang, *Phys. Rev. Lett.* **94**, 108101 (2005).
- [22] M. J. Rust, M. Bates, and X. Zhuang, *Nat. Methods* **3**, 793 (2006).
- [23] M. Heilemann, S. van de Linde, M. Schüttelpe, R. Kasper, B. Seefeldt, A. Mukherjee, P. Tinnefeld, and M. Sauer, *Angew. Chem. Int. Ed. Engl.* **47**, 6172 (2008).
- [24] M. Heilemann, S. van de Linde, A. Mukherjee, and M. Sauer, *Angew. Chem. Int. Ed. Engl.* **48**, 6903 (2009).
- [25] V. A. Oijen, J Köhler, J Schmidt, M Müller, and GJ Brakenhoff, *Chemical Physics Letters* **292**, 183 (1998).
- [26] P. Prabhat, S. Ram, E. S. Ward, and R. J. Ober, *IEEE Trans Nanobioscience* **3**, 237 (2004).
- [27] S. Ram, J. Chao, P. Prabhat, S. Ward, and R. Ober, (2007).
- [28] M. F. Juette, T. J. Gould, M. D. Lessard, M. J. Mlodzianoski, B. S. Nagpure, B. T. Bennett, S. T. Hess, and J. Bewersdorf, *Nat. Methods* **5**, 527 (2008).
- [29] C. Simons and H. Lam, (1977).

1.7 References

- [30] H. Kao and A. Verkman, *Biophysical Journal* **67**, 12911300 (1994).
- [31] L. Holtzer, T. Meckel, and T. Schmidt, *Applied Physics Letters* **90**, 053902 (2007).
- [32] B. Huang, W. Wang, M. Bates, and X. Zhuang, *Science (New York, N.Y.)* **319**, 810 (2008).
- [33] S. R. Pavani and R. Piestun, *Opt Express* **16**, 3484 (2008).
- [34] S. R. Pavani, M. A. Thompson, J. S. Biteen, S. J. Lord, N. Liu, R. J. Twieg, R. Piestun, and W. E. Moerner, *Proc. Natl. Acad. Sci. U.S.A.* **106**, 2995 (2009).
- [35] F. Zancchi, Z. Lavagnino, M. Donnorso, A. Bue, L. Furia, M. Faretta, and A. Diaspro, *Nature Methods* **8**, 1047 (2011).
- [36] G. Shtengel, J. A. Galbraith, C. G. Galbraith, J. Lippincott-Schwartz, J. M. Gillette, S. Manley, R. Sougrat, C. M. Waterman, P. Kanchanawong, M. W. Davidson, R. D. Fetter, and H. F. Hess, *Proc. Natl. Acad. Sci. U.S.A.* **106**, 3125 (2009).
- [37] H. Shroff, C. G. Galbraith, J. A. Galbraith, and E. Betzig, *Nat. Methods* **5**, 417 (2008).

CHAPTER 2

SINGLE MOLECULE STUDY OF RAS MEMBRANE DOMAINS REVEALS DYNAMIC BEHAVIOR¹

Abstract

It has been conjectured that the differential behavior of the various isoforms of the small GTPase Ras is related to their spatial and temporal organization in the plasma membrane. Indeed, earlier experiments by fluorescence photobleaching, single molecule tracking, fixed cell super-resolution microscopy and cryo electron microscopy showed that Ras proteins are localized in membrane nano-domains. It showed the domains differ in size depending on the specific isoform characterized by the specific membrane anchor. Here we performed live-cell super-resolution imaging with 18 nm positional accuracy on the membrane anchors of the various Ras isoforms. Comparison between live-cell and fixed-cell super-resolution microscopy on the membrane anchor of H-Ras showed broadening of the apparent domain size. We show that domain mobility of $5 \cdot 10^{-4} \mu\text{m}^2/\text{s}$ can quantitatively explain the broadening of the apparent domain size with observation time.

¹This chapter is based on: R. Harkes, V.I.P. Keizer, M.J.M. Schaaf and T.Schmidt, Single molecule study of Ras-membrane domains reveals dynamic behavior. Submitted to Biophysical Journal

2.1 INTRODUCTION

Ras proteins are small GTPases that reside in the cytosolic leaflet of the plasma membrane [1]. The discovery of mutated, constitutively active Ras proteins in several cancers triggered extensive research into the Ras-family of proteins [2–4]. Ras proteins are active in the GTP-bound form and signal towards several pathways including Raf [5–8] and MAPK [9,10]. The activation of Ras by membrane-bound receptor proteins like the insulin receptor is mediated by guanine nucleotide exchange factors (GEFs) that release GDP from Ras and therefore allow binding of GTP [11]. GTPase activating proteins (GAPs) on the other hand deactivate Ras by promoting the conversion of GTP to GDP [12,13]. For an efficient and reliable working of this activation/deactivation cycle it is advantageous when membrane receptors, Ras, GEFs and GAPs are spatially organized to facilitate the interaction of Ras with the various regulatory proteins crucial to Ras signaling.

The Ras family of proteins consists of three different isoforms: the H-Ras, N-Ras and K-Ras. Expression of mutants of these isoforms vary for different types of cancer [14]. This indicates a different function for each of these isoforms in normal cells. It is interesting to note that the GTPase domain of all Ras isoforms is almost identical, but the various isoforms serve different functionalities. The difference in functionality seems to rely on the last 25 amino acids on the C-terminus, that have a homology of less than 15% and form the so-called hyper variable region (HVR) of Ras [15]. The C-terminal domain is further post translationally modified to contain hydrophobic lipid anchors that protrude the inner leaflet of the plasma membrane. Whereas H-Ras has three such anchors, the N-Ras isoform has two and K-Ras has one hydrophobic anchor on top of a 10 amino acid long positively charged lysine stretch [14]. Given the large similarity when excluding the HVR, it can be speculated that the different functionalities of Ras isoforms are associated with a differential localization into the plasma membrane as dictated by their lipid anchor. Association to different local membrane environments might in turn influence their interaction with GEFs and GAPs.

The plasma membrane of cells has long been modeled according to Singer & Nicholsons fluid-mosaic [16]. In this model the membrane is described as a uniform, two dimensional liquid that enables membrane proteins to diffuse freely. The last decades have seen compelling experimental evidence of a more heterogeneous and dynamic picture of the plasma membrane. E.g. for Ras earlier

studies from our lab and others showed that the diffusion for both H-Ras and K-Ras is confined to domains that have a size on the order of 200 nm [17] [18]. Likewise, with the development of optical super-resolution techniques localization of membrane-bound proteins in fixed cells has been investigated [19] Those experiments showed clustering of membrane proteins into domains of a size that was found compatible with the earlier findings using single molecule tracking.

Here, photoactivatable localization microscopy (PALM) is applied to directly observe the clustering of membrane anchors in living cells. To investigate their organization on the plasma membrane we transiently expressed the C terminal domain of the various Ras isoforms linked to mEos2 and the N terminal domain of Src linked to mEos2. mEos2 is a photoconvertible fluorescent protein that enables us to utilize optical super-resolution microscopy and to visualize plasma membrane domains and their dynamics. We show that membrane domains have a size of 40-50 nm, corroborating earlier electron microscopy data, that those domains are mobile within the plasma membrane, and must be stable for at least 7 s.

2.2 MATERIALS AND METHODS

2.2.1 Microscope

For excitation of the green fluorescent state of the photoactivatable protein mEos2, a 488nm DPSS-laser (Coherent) was used. The red state was excited using a 532nm DPSS-laser (Cobolt). Photoconversion of mEos2 was initiated by a 405nm diode laser (Crystalaser). The laser beams were overlaid by dichroic mirrors, passed an acousto-optic tunable filter (AOTF_nC-400.650, aa optics) and fed into a mono-mode fiber before coupled into the microscope.

The microscope (Axiovert S100, Zeiss) was equipped with a 100x, 1.4NA oil-immersion objective (Zeiss). Lasers were coupled into the back port. The emission light was passed through a 4-channel dichroic mirror ZT405/488/561/638rpc (Chroma) and a dual channel emission filter ZET561/640m (chroma). The image was finally focused onto a sCMOS camera (orca flash 4.0V2, Hamamatsu).

To image live cells the medium was replaced by pure dulbecco's modified eagle medium (DMEM). Cells were mounted in a custom made holder for a stage incubator (TokaiHit incubater stage INUBG2ESFP-ZILCS). For life cell measurements the device was set to 37°C and 5% CO₂ atmosphere.

During search for transfected cells the 488 nm intensity was kept at 100 W/cm². To detect individual molecules on a fairly flat part of the apical membrane we regularly chose a region on top of the nucleus. Activation and photoswitching intensities with 405 nm were set between 0 and 20 W/cm², depending on the expression level and prior activation. Imaging with 532 nm was done at 3 kW/cm² for 3000 frames. Cells were illuminated for 10 ms per frame at a frame rate of 79 Hz.

2.2.2 Correction for double detections

One issue in localization microscopy when used to quantify local distributions is the potential sequential detection of molecules in multiple frames due to insufficient photobleaching. In imaging, double counting would lead to artifacts and would lead to an apparent clustering. There are various methods to minimize double detections in stochastic imaging [20]. Here we used a windowed-filtering where sequential detections within the localization precision of a molecule were removed for a time-window of 10 frames, i.e. 0.13 s of total exposure. mEos2 has been shown to have a typical off time of 0.1 ± 0.01 s at 1kW/cm² excitation

intensity and 100 mW/cm^2 activation intensity [21]. Assuming that those intensities are still in the linear regime, we predict a double-count probability of $\exp(-3 \cdot 0.13/0.1) = 0.02$ at an excitation intensity of 3 kW/cm^2 for the 10-frame exclusion window chosen.

2.2.3 Cell culture and transfection

Plasmids

Plasmids were cloned by inserting the membrane targeting domain of human Ras at the c-terminus of mEos2 N11K / E70K / H74N / V123T / T158H / H121Y. For srcN15 the sequence was attached to the n-terminus.

H-CAAX : -GCMSCKCVLS
N-CAAX : -GCMGLPCVVM
K-CAAX : -KKKKKKSKTKCVIM
SRCN15 : -MGSSKSKPKDPSQRRNNNN-

Cells

COS-1 cells were grown in growth medium; DMEM without phenol red (Life Technologies) supplemented with 10% FCS under conditions of 37 degrees Celsius and 5% CO₂. Prior to transfection cells were plated in 6-wells plate on coverslip glasses. Transient transfection was carried out using FuGENE HD transfection agent (Promega), following manufacture's procedure, but allowing for 3hrs incubation time of the DNA plasmid and transfection reagent. Two days post transfection cells were imaged in conditions similar to culturing conditions.

Fixation of cells was done by incubation for 15 minutes in 4% paraformaldehyde in phosphate buffered saline at room temperature.

2.2.4 Analysis software

Fluorescence images were taken with up to 3000 images per measurement. The fluorescence signal on the sCMOS from individual molecules was fitted with a 2 dimensional Gaussian using a custom LSE algorithm in Matlab [22].

2.2.5 Ripley

Ripley's analysis [23] was performed in Matlab with edge correction as suggested by Diggle. [24]

2.2.6 Bootstrapping and automatic selection

Ripley's analysis is sensitive to artifacts originating from edge effects. To obtain statistics, and to deal with these artifacts we used a bootstrapping method. We calculated Ripley's curves for small regions-of-interest of $1 \times 1 \mu\text{m}^2$ in size. When the curve would not rise above 50 nm the square would be considered random and discarded from the analysis.

When such an area is located on the edge of a cell there will be no large distances. The effect of this is that the value of $L(r)$ - r curve will not decrease back to 0 for large radii, but instead end above zero. In further analysis also those curves were discarded.

Therefore Ripley's $L(r)$ - r curves were removed based on two properties:

- 1) The last 90% in r must be between -30 and 30 nm
- 2) From $r = 260$ nm to the end, the curve must decrease

These criteria showed effective removal of ROI's at the edge of a simulated point pattern (see supplemental Fig S1).

2.2.7 Simulation of cluster diffusion

6000 freely diffusing objects together with 60 randomly positioned clusters of 50 objects each were generated. The 60 clusters were allowed to diffuse with a given diffusion constant and a mean lifetime from an exponential distribution. When a cluster reached its lifetime the points were allocated to the 6000 freely diffusing objects, and a new position was chosen as a formation location for a new cluster. The nearest objects were taken from the freely diffusing fraction and reallocated to the cluster. From this simulation 3000 frames of 2 realizations were selected.

2.3 RESULTS

2.3.1 Imaging of H-CAAX in fixed COS1 cells

The nanoscopic distribution of the membrane-anchoring domain of Ras, the so-called CAAX-domain, was studied in the cytosolic leaflet of the plasma membrane using photo-activatable localization microscopy (PALM). We fused the sequence of the green-to-red photo-convertible fluorescent protein mEos2 to the anchoring domains of the various Ras isoforms leading to the H-CAAX-mEos, N-CAAX-mEos, and K-CAAX-mEos constructs, respectively (see Fig.1a). COS1 cells were transiently transfected with the constructs. Transfected cells showed a clear localization of the fluorescent constructs to the plasma membrane confirming earlier results for the CAAX-YFP constructs [25] in 3T3-fibroblasts.

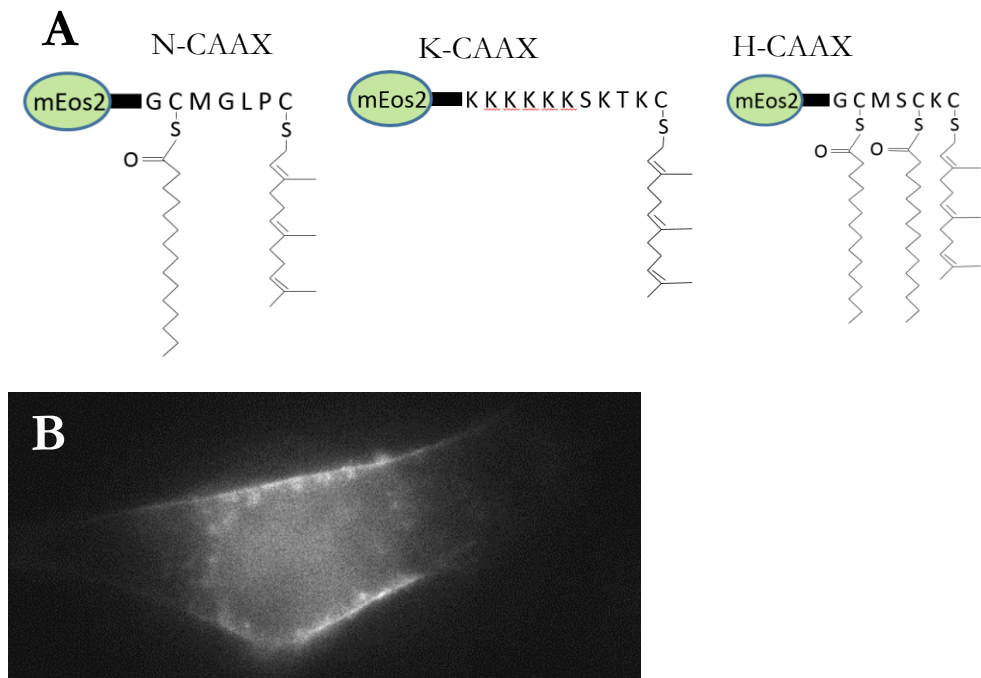


Figure 1: A) Schematic representation of the different CAAX constructs.

B) Fluorescent image of H-CAAX-mEos2 clearly shows membrane localizations in Cos1 cells. Excitation 488nm, 100W/cm², 10ms.

2.3 Results

The membrane localization is exemplified for H-CAAX-mEos in Figure 1b when imaged on a confocal microscope for excitation of the green form of mEos at 488nm.

Subsequently cells were imaged on a camera-based wide-field single molecule imaging setup for super-resolution PALM microscopy. In PALM only a small subset of fluorescent molecules are activated in each frame, thereby temporally separating the fluorescent emission of individual molecules and allowing to distinguish the signals from individual molecules. The signals are subsequently fit to the point-spread-function of the microscope. From the fit the location of each individual molecule is determined to high accuracy. Using mEos2, activation is achieved by a photoconversion of a few molecules ($< 0.1/\mu\text{m}^2$) to the red form by low-intensity 405 nm light ($1\text{-}50 \text{ W}/\text{cm}^2$ for 10 ms). Subsequently individual H-CAAX-mEos in the red form were imaged using high intensity illumination of $3 \text{ kW}/\text{cm}^2$ at 532 nm. The mean signal detected from individual H-CAAX-mEos molecules was 300 ± 130 photons per illumination time of 10 ms. This signal permitted to localize individual H-CAAX-mEos to a precision of 17 nm (Fig. 2), as predicted theoretically [26].

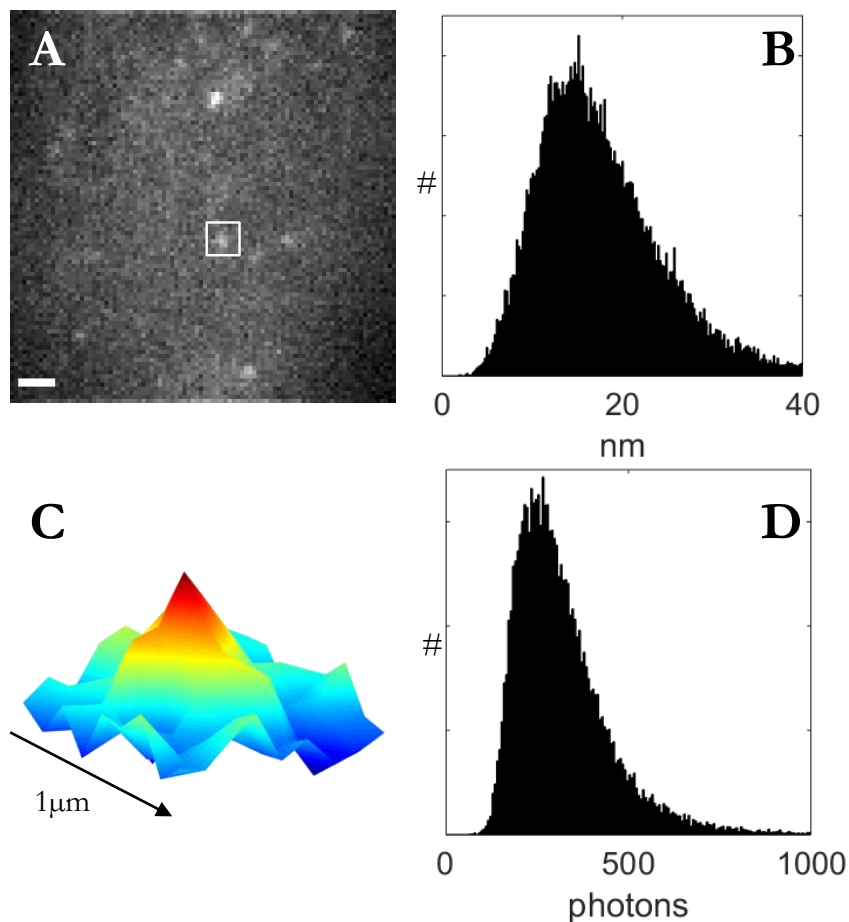


Figure 2: Characteristic properties of the optical setup

A) Frame with the signal of several mEos2 molecules. Scale bar = $2\mu\text{m}$

B) Histogram of the sigma of positional accuracy. Mean 18 nm

C) Zoom-in of white square to show Gaussian intensity.

D) Histogram of the intensity of localizations. Mean 317 photons.

2.3 Results

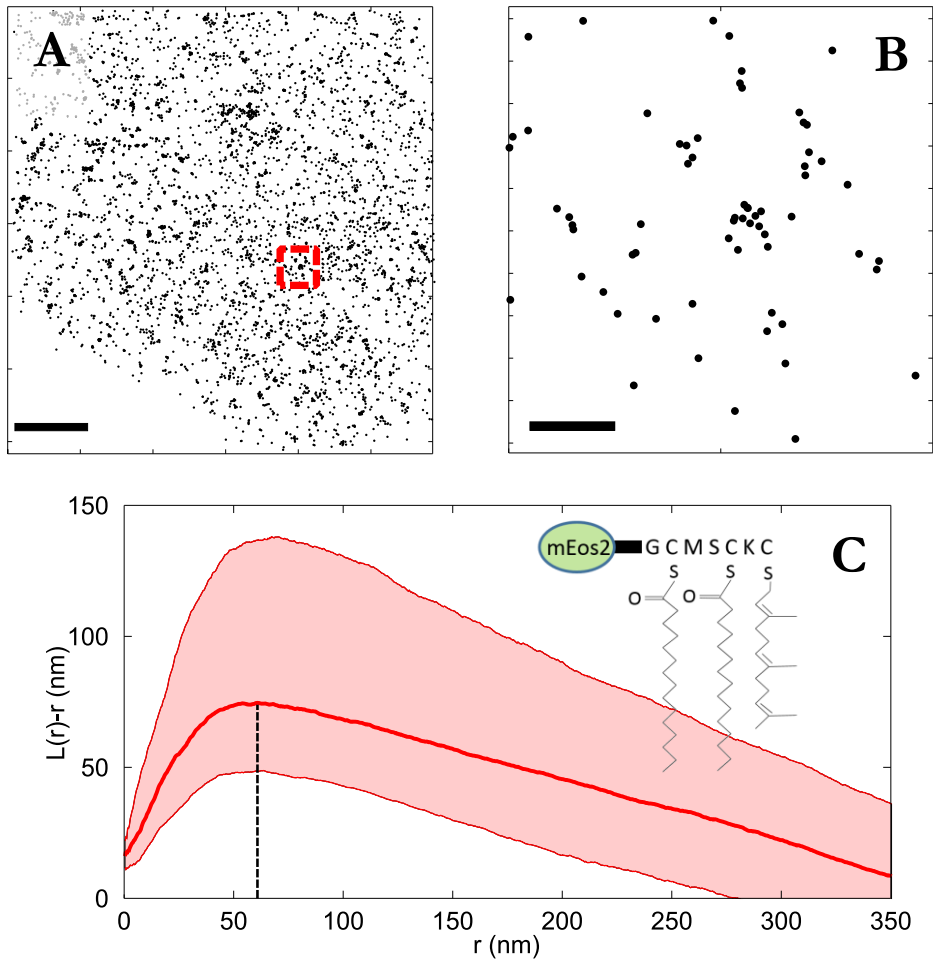


Figure 3: 5406 independent positions on the apical side of a fixed COS1 cell, that were detected within one measurement of 38 s (3000 frames) are shown for the H-CAAX-mEos2 construct

A) Localization of H-CAAX-mEos2 in fixed COS1 cells. Scalebar: $2\mu\text{m}$.

B) Zoom-in of the red square. Clustering is observed in small domains. Scalebar: 200nm.

C) Ripley's analysis on 7 cells. 51244 localizations were used. For each cell 1000 subsets of $1 \times 1 \mu\text{m}$ were analyzed. The solid line is the median of all analyses, the shaded area contains 75% of all analyses. The maximum of $L(r)-r$ appears at 65 ± 3 nm. $22 \pm 2\%$ of the molecules were distributed at random.

In figure 3 the localization data for H-CAAX-mEos2 clearly shows a large inhomogeneity in the spatial distribution of the protein on large (1 μm ; figure 3a) and small (0.1 μm ; figure 3b) length scales, indicative for clustering of H-CAAX.

To quantify the inhomogeneity we used a variant of Ripley's spatial statistics analysis [23]. In Ripley's analysis the mean number of neighbouring molecules up to a given distance, r , is compared to a spatially random situation (see chapter 2.2: materials and method). Deviation of Ripley's curve from zero is indicative of a spatially non-homogeneous distribution with clustering for positive, and depletion for negative deviation from zero. The position of the maximum corresponds to the typical size of a cluster [23]. The accuracy of the analysis was estimated by a bootstrapping strategy. For each image of $10 \times 10 \mu\text{m}^2$ we extracted 1000 randomly positioned, partially overlapping spatial subsets of $1 \times 1 \mu\text{m}^2$ in size for which Ripley's analysis was performed. The mean (solid line) and 75% quantile (shaded areas) of such bootstrap analysis applied to the data in figure 3a is shown in figure 3c. H-CAAX showed a significant deviation from a random distribution. For a random distribution it has been shown that the absolute value of Ripley's function $|L(r)-r|$ does not exceed a value of 10 nm [19]. For H-CAAX the Ripley curve assumes a maximum for a distance of 65 ± 3 nm. Further, we found that $22 \pm 2\%$ of the H-CAAX molecules were randomly distributed. Those results corroborate our earlier findings by PALM [19] on a similar construct in which the membrane anchor was fused to dendra2 (for both, H-CAAX-dendra2 and the full HRas-dendra2), when taking into account the significant increase in positional accuracy from 40 nm in the earlier studies to 18 nm in the current study. The increase in localization accuracy was due to the use of the optimized mEos2 construct and the use of a sCMOS camera. From our data the typical size of H-CAAX domains is estimated to be $65 - 2 \times 18 = 29$ nm, taking into account the localization accuracy of 18 nm and the apparent typical domain size of 65 nm from the position of the maximum of Ripley's curve in figure 3C. Our result is in excellent agreement with the cryo-electron microscopy findings by Prior et al. [27] where a typical clustering length scale of 22 nm was reported.

2.3.2 Imaging of H-CAAX in living COS1 cells

We realized that the estimated membrane domain size that was found for fixed cells was significantly smaller (65 nm apparent size) compared to earlier findings by single molecule tracking (180-210 nm) [25]. Here we address the question on

2.3 Results

whether and how the typical clustering size was modified by the fixation method. Therefore we performed PALM measurements on live cells for all constructs.

A super-resolution image taken on the apical membrane of a living COS-1 cell when transfected with H-CAAX is shown in figure 4. The image was constructed from a 3000-frame image stack that lasted 38 s in total. In comparison to the results on fixed cells shown in figure 3, a significant broadening of Ripley's curve was apparent. The position of the maximum of Ripley's curve shifted significantly to 183 ± 7 nm.

Similar results were obtained for the other constructs (K-CAAX:figure 5b, N-CAAX:figure 5c, and yet another membrane anchor from the src family of kinases:figure 5d). The maximum of Ripley's curve was 160 ± 4 , 180 ± 12 and 172 ± 11 nm for K-CAAX, N-CAAX and src, respectively. The bootstrapping suggest that K-CAAX clustered on a larger portion of the plasma membrane than the other constructs.

The positions of the maxima found for the Ripley's curves in live-cell PALM are in excellent agreement to our earlier findings using live-cell single molecule tracking (H-CAAX: 219 nm; K-CAAX: 206 nm) [25]. In those experiments, the length scale of clustering was estimated from diffusion measurements in which the mean-squared displacement displayed behaviour of confined diffusion.

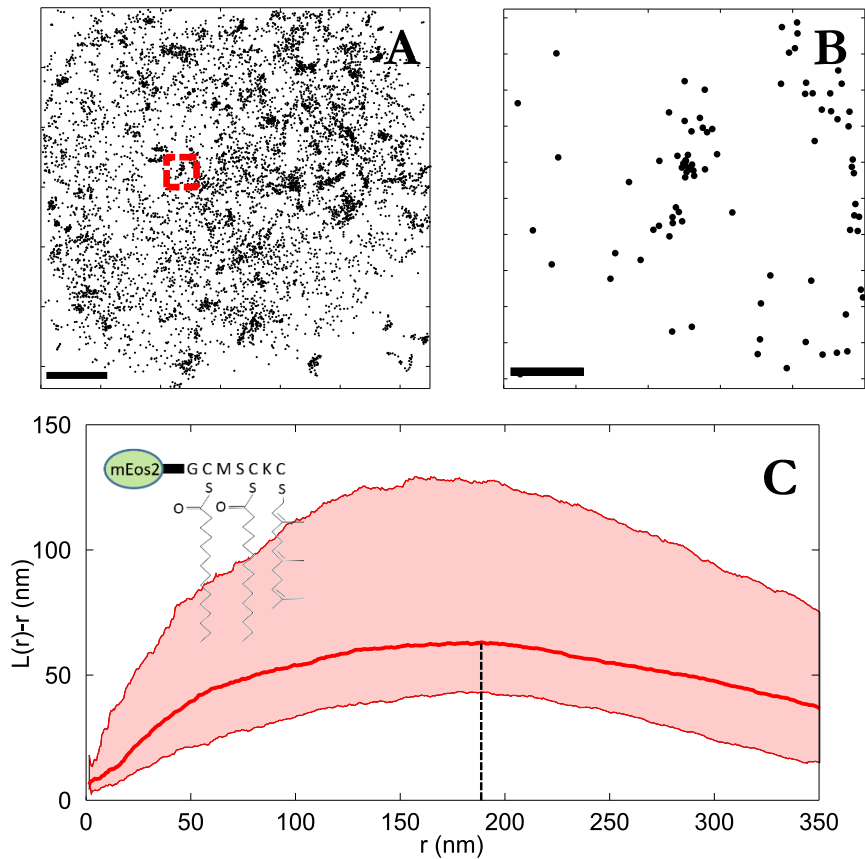


Figure 4: Typical result of H-CAAX-mEos2 in living COS1 cells.

A) Localization of H-CAAX-mEos2 in living COS1 cells. Imaging time 38 seconds. Scale bar: 2 μm.

B) Zoom in to the red square. Clustering is observed in domains on different scales. Scale bar: 200 nm.

C) Ripley's analysis on 9 cells. For each cell 1000 subsets of $1 \times 1 \mu\text{m}$ were analyzed. The solid line is the median, and the shaded area reflects the 75% interval. The position of the maximum is localized at 183 ± 7 nm

2.3 Results

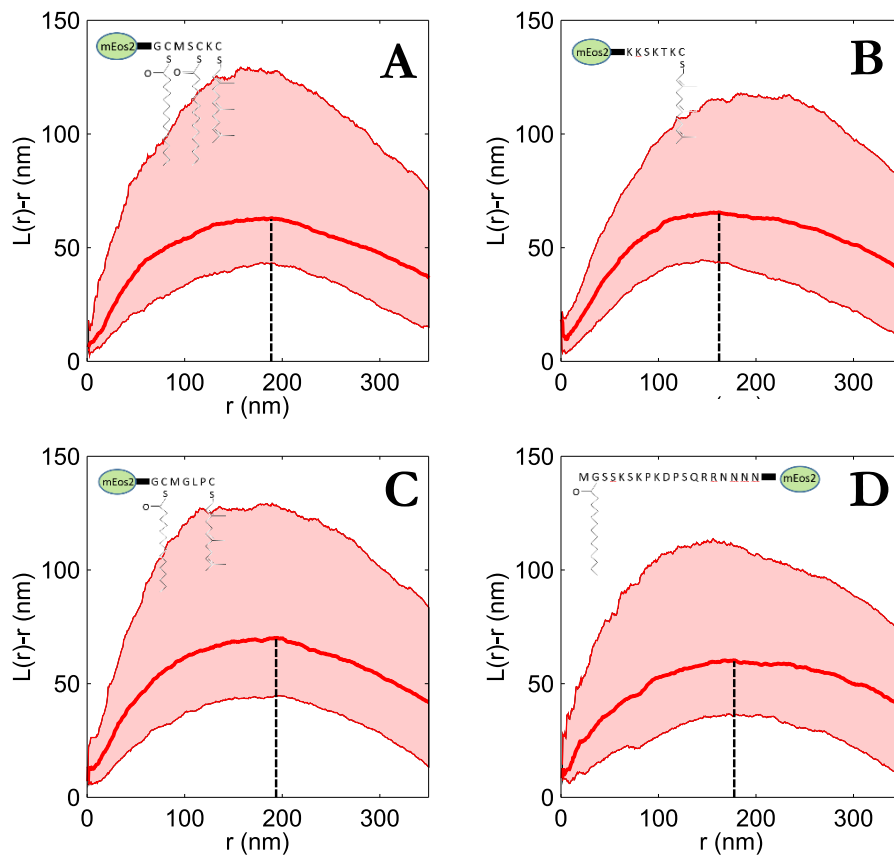


Figure 5: Ripley curves of various membrane anchors.

A) H-CAAX position of the maximum 183 ± 7 nm; random population $57 \pm 1\%$.

B) K-CAAX position of the maximum 160 ± 4 nm; random population $37 \pm 1\%$

C) N-CAAX position of the maximum 180 ± 12 nm; random population $50 \pm 1\%$

D) SRC-N15 position of the maximum 172 ± 11 nm; random population $50 \pm 1\%$

We further designed experiments to understand the significant difference we found between results on H-CAAX obtained in experiments on fixed cells (position of the maximum 65 nm) in comparison to live-cell measurements (180 nm). It should be mentioned that sample drift, although increased from 20 to 50 nm/min in the live-cell situation as determined by observation of fiducial markers, was too small to explain the difference.

Ripley's analysis assumes that the spatial pattern is stable during the course of the experiment. In fixed-cell experiments the distribution of the domains is frozen at the time point of fixation. However, in live-cell experiments any domain dynamics will lead to a broadening of Ripley's curve and to a shift of the position of its maximum to higher values. It has been proposed that plasma membrane domains are mobile, dynamic entities with a lifetime of at least 1 s [28] If they are responsible for the observed clustering of Ras and its membrane anchors we can expect the membrane anchors to behave similarly. For domains that are mobile we predicted that the position of the maximum of Ripley's curve would increase with the observation time.

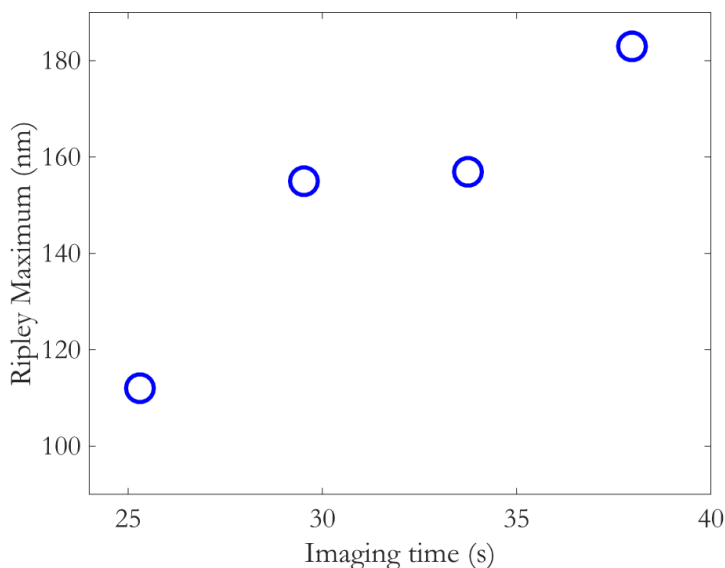


Figure 6: The effect of shorter imaging time on the position of the maximum of Ripley's curve. For shorter times the domains appear smaller.

To test this hypothesis we analysed the data on live-cell H-CAAX in an observationtime dependent manner. We first restricted analysis to the initial 2000 images (25 s) and then subsequently added additional image frames. The

2.3 Results

shortest time window (25 s) was given by the minimum number of positions N_{\min} required to obtain a given spatial resolution Δr as set by the Nyquist theorem, $N_{\min} = \alpha(2L/\Delta r)^2$, given an image size of L^2 covered by domains that contain only a fraction α . Aiming for a resolution of $\Delta r = 60$ nm in an image of size $(6 \times 6) \mu\text{m}^2$ at a coverage of 10%, $N_{\min} = 4000$. The data of HRAs obtained from such analysis are shown in figure 6. As predicted for mobile domains the Ripley curves broaden with increase in observation time and the maximum of the curves shifted towards larger values. The position of the maximum for the shortest interval of 25 s was 112 nm, whereas it was 183 nm for the full 38 s image stack.

In order to quantitatively understand our experimental findings we performed Monte Carlo simulations. 6000 freely diffusing objects together with 60 randomly positioned clusters of 50 objects each were generated and subsequently allowed to diffuse, create and dissolve, such that the average number of clusters was kept constant (see chapter 2.2 materials and methods). Subsequently Ripley's analysis was applied on the simulated image stack. Results of those simulations are shown in figure 7. We found that the lifetime of the clusters must be at least in the order of the minimum observation time (data not shown). For stable clusters that were allowed to diffuse, the maximum of Ripley's curves shifted non-linearly towards larger values when the observation time was increased. The broadening and shift was dependent on the diffusion constant of the domains (data not shown).

Taking our experimental findings as limits, the increase in domain size in living cells was recovered in the simulations by allowing domains of actual size of 65 nm to diffuse. By setting the diffusion constant to $D_{\text{domain}} = 5\text{-}7 \cdot 10^{-4} \mu\text{m}^2/\text{s}$ and the domain lifetime larger than 7 s we could observe the same maximum in the Ripley curves as shown in figure 5 for live cells.

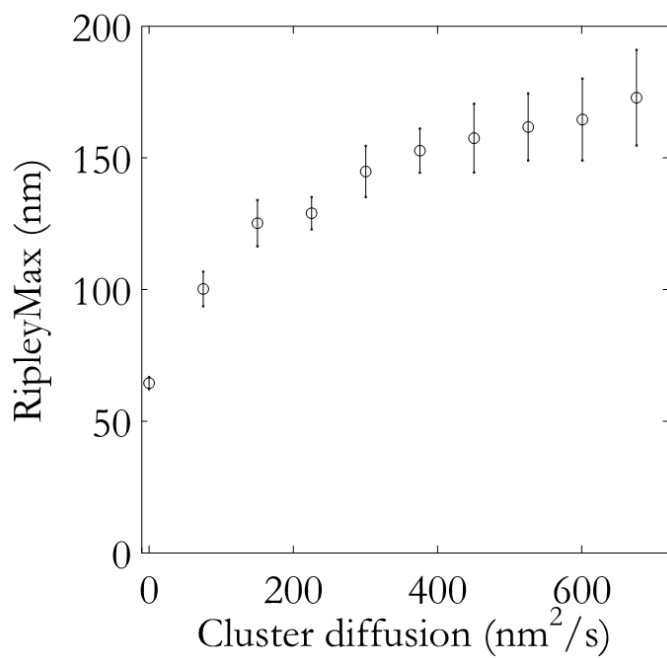


Figure 7: Monte-Carlo simulation showing the effect of cluster diffusion on maximum of Ripley's analysis.

2.4 DISCUSSION

The differential sensitivity and specificity of signaling by the various Ras isoforms has initiated a long discussion in the literature [29]. The general idea that emerged was that the differential behavior is controlled by the specificity of the membrane anchors in different isoforms. Thereby specificity might be controlled by the localization to specific nano-domains on the cytosolic side of the plasma membrane. Ras-specific nano-domains have been inferred from early fluorescence photobleaching recovery experiments [18], later single molecule tracking [30], fixed-cell super-resolution imaging [19] and cryo-electron microscopy [27]. Although the existence of Ras nano-domains is undisputed, the molecular origin, size, and dynamic behavior has so far not been addressed. Since all techniques mentioned above need special preparation methods a quantitative agreement between the results could not be achieved.

Our live-cell data, at least in part, is able to alleviate the inconsistencies found in literature. We found that nano-domains indeed exist in the live-cell situation. We further found that domains are mobile and had a lifetime of at least 7 s. Their mobility readily explains the difference in size as obtained by cryoEM and fixed-cell PALM when compared to single molecule tracking and live-cell PALM.

Our simulations indicate that domain mobility is characterized by diffusion with a diffusion constant of $D_{\text{domain}} = 5 \times 10^{-4} \mu\text{m}^2/\text{s}$. It appears interesting to note, that this diffusion constant is much smaller than that predicted for a cylindrical object in a 2-dimensional sheet as determined by the Saffman-Delbrück model [31]. From previous protein diffusion values of $0.1 \mu\text{m}^2/\text{s}$ [30] for single proteins with an approximate radius of 1 nm we can derive a membrane viscosity of 8.4 Pa·s. This predicts a diffusion constant of an object of size 29 nm to be $6.6 \times 10^{-2} \mu\text{m}^2/\text{s}$.

The significant difference in the observed diffusion constant with this prediction permits speculation about the molecular origin of the nano-domains. I.e. it appears very unlikely that domains reflect lipid inhomogeneities, like lipid rafts [32], in an otherwise homogeneous, unstructured lipid environment. Rather, our data point to an interpretation that Ras nano-domains reflect structuring of the membrane by some underlying, potentially cytoskeletal structure. This speculation is supported by earlier experimental findings by single molecule tracking in which the existence of membrane nano-domains was found to be independent of cholesterol extraction, however was dependent on breakdown of the actin cyto and membrane skeleton by the drug latrunculin [25].

Hence, it is not too surprising that size and lifetime of the nano-domains is not significantly different for the different membrane anchors, a result that has been likewise found in earlier single molecule tracking experiments. [30] In order to prove the existence of distinct nano-domains, specific for the different membrane anchors, future dual-color experimental strategies will have to be employed in which colocalization or cross-correlation between the colors is analyzed. With the developments described in the current report, such experiments appear feasible.

2.5 OUTLOOK

Imaging of Ras nano-domains using fluorescence microscopy is a challenging task. Not only due to the small size, but also because of sparse labeling of the clusters. Experiments done on fixed 3T3 cells with H-CAAX-eYFP using STED microscopy resulted in fast bleaching of the fluorophores inside the cluster. Since STED is a scanning technique the signal is obtained the first time the spot moves over the cluster. This is presented as single horizontal line that becomes less intense from left to right. We did not move on to live cell microscopy using STED.

The observed broadening of Ripley's curve when more frames are taken into account is a potential tool to detect the diffusion of a small cluster of molecules. This effect has been shown in simulations and for the membrane anchor H-CAAX. To further prove this method it would be recommended to perform a control experiment where the sensitivity to cluster diffusion can be quantified. By crosslinking five GM1-mEos2 proteins using CtxB, stable clusters of photoconvertible fluorescent proteins can be created. One could then vary the framerate to increase the effect of diffusion on the broadening of Ripley's curve.

A recently discovered problem with mEos2 is the self-clustering on the plasma membrane. At its discovery in 2009 [33] it was reported that mEos2 showed a relative high tendency to form dimers. This was measured by polarization measurements on increasing concentrations of protein. Dendra2, another photoactivatable fluorescent protein, showed loss in polarization at 12 μM , mEos2 showed loss in polarization at 0.5 μM . Since 0.5 μM is still well below the concentrations in our experiments it gave no reason for concern. However in experiments on the membrane, the 2D confinement greatly increases the probability of interaction [34] Furthermore, Magenau et al. [35] showed that mEos2 influences membrane clustering of several probes. To quantify this effect

2.5 Outlook

it would be required to compare experiments using for example Dendra2 and mEos2.

2.6 REFERENCES

- [1] D. DeFeo, M. A. Gonda, H. A. Young, E. H. Chang, D. R. Lowy, E. M. Scolnick, and R. W. Ellis, *Proc. Natl. Acad. Sci. U.S.A.* **78**, 3328 (1981).
- [2] R. W. Sweet, S. Yokoyama, T. Kamata, J. R. Feramisco, M. Rosenberg, and M. Gross, *Nature* **311**, 273 (1984).
- [3] J. B. Gibbs, I. S. Sigal, M. Poe, and E. M. Scolnick, *Proc. Natl. Acad. Sci. U.S.A.* **81**, 5704 (1984).
- [4] J. P. McGrath, D. J. Capon, D. V. Goeddel, and A. D. Levinson, *Nature* **310**, 644 (1984).
- [5] X. F. Zhang, J. Settleman, J. M. Kyriakis, E. Takeuchi-Suzuki, S. J. Elledge, M. S. Marshall, J. T. Bruder, U. R. Rapp, and J. Avruch, *Nature* **364**, 308 (1993).
- [6] P. H. Warne, P. R. Viciano, and J. Downward, *Nature* **364**, 352 (1993).
- [7] S. A. Moodie, B. M. Willumsen, M. J. Weber, and A. Wolfman, *Science* **260**, 1658 (1993).
- [8] A. B. Vojtek, S. M. Hollenberg, and J. A. Cooper, *Cell* **74**, 205 (1993).
- [9] SJ Leever and CJ Marshall, *The EMBO Journal* (1992).
- [10] K. W. Wood, C. Sarnecki, T. M. Roberts, and J. Blenis, *Cell* **68**, 1041 (1992).
- [11] E. Y. Skolnik, A. Batzer, N. Li, C. H. Lee, E. Lowenstein, M. Mohammadi, B. Margolis, and J. Schlessinger, *Science* **260**, 1953 (1993).
- [12] U. S. Vogel, R. A. Dixon, M. D. Schaber, R. E. Diehl, M. S. Marshall, E. M. Scolnick, I. S. Sigal, and J. B. Gibbs, *Nature* **335**, 90 (1988).
- [13] H. Adari, D. R. Lowy, B. M. Willumsen, C. J. Der, and F. McCormick, *Science* **240**, 518 (1988).
- [14] AE Karnoub and RA Weinberg, *Nature Reviews Molecular Cell Biology* (2008).
- [15] Hancock, (2003).
- [16] S. Singer and G. Nicolson, *Science* **175**, 720 (1972).
- [17] P. H. Lommerse, B. E. Snaar-Jagalska, H. P. Spaank, and T. Schmidt, *J. Cell. Sci.* **118**, 1799 (2005).
- [18] H Niv, O Gutman, Y Kloog, and YI Henis, *The Journal of Cell Biology* (2002).
- [19] A. Pezzarossa, F. Zosel, and T. Schmidt, *Biophys. J.* **108**, 1870 (2015).
- [20] P. Annibale, S. Vanni, M. Scarselli, U. Rothlisberger, and A. Radenovic, *PLoS ONE* **6**, e22678 (2011).
- [21] P. Annibale, S. Vanni, M. Scarselli, U. Rothlisberger, and A. Radenovic, *Nature Methods* **8**, 527 (2011).
- [22] T. Schmidt, G. J. Schütz, W. Baumgartner, H. J. Gruber, and H. Schindler, *Proc. Natl. Acad. Sci. U.S.A.* **93**, 2926 (1996).
- [23] B. Ripley, *Journal of Applied Probability* **13**, 255 (1976).
- [24] P. J. Diggle, *Statistical Analysis of Spatial Point Patterns* (Academic Press, 1983).
- [25] P. Lommerse, G. Blab, L. Cognet, G. Harms, E. Snaar-Jagalska, H. Spaank, and T. Schmidt, *Biophysical Journal* **86**, 609 (2004).
- [26] N Bobroff, *Review of Scientific Instruments* (1986).

2.6 References

- [27] I. Prior, C. Muncke, R. Parton, and J. Hancock, *The Journal of Cell Biology* **160**, (2003).
- [28] A. Kusumi, C. Nakada, K. Ritchie, K. Murase, K. Suzuki, H. Murakoshi, R. S. Kasai, J. Kondo, and T. Fujiwara, *Annu Rev Biophys Biomol Struct* **34**, 351 (2005).
- [29] O. Rocks, A. Peyker, and P. I. Bastiaens, *Curr. Opin. Cell Biol.* **18**, 351 (2006).
- [30] P. H. Lommerse, K. Vastenhoud, N. J. Pirinen, A. I. Magee, H. P. Spalink, and T. Schmidt, *Biophys. J.* **91**, 1090 (2006).
- [31] P. G. Saffman and M. Delbrück, *Proc. Natl. Acad. Sci. U.S.A.* **72**, 3111 (1975).
- [32] K. Simons and E. Ikonen, *Nature* **387**, 569 (1997).
- [33] S. McKinney, C. Murphy, K. Hazelwood, M. Davidson, and L. Looger, *Nature Methods* **6**, 131 (2009).
- [34] M. Schmick and P. I. Bastiaens, *Cell* **156**, 1132 (2014).
- [35] A. Magenau, D. M. Owen, Y. Yamamoto, J. Tran, J. M. Kwiatek, R. G. Parton, and K. Gaus, *Mol. Membr. Biol.* **32**, 11 (2015).

2.7 SUPPLEMENTARY FIGURES

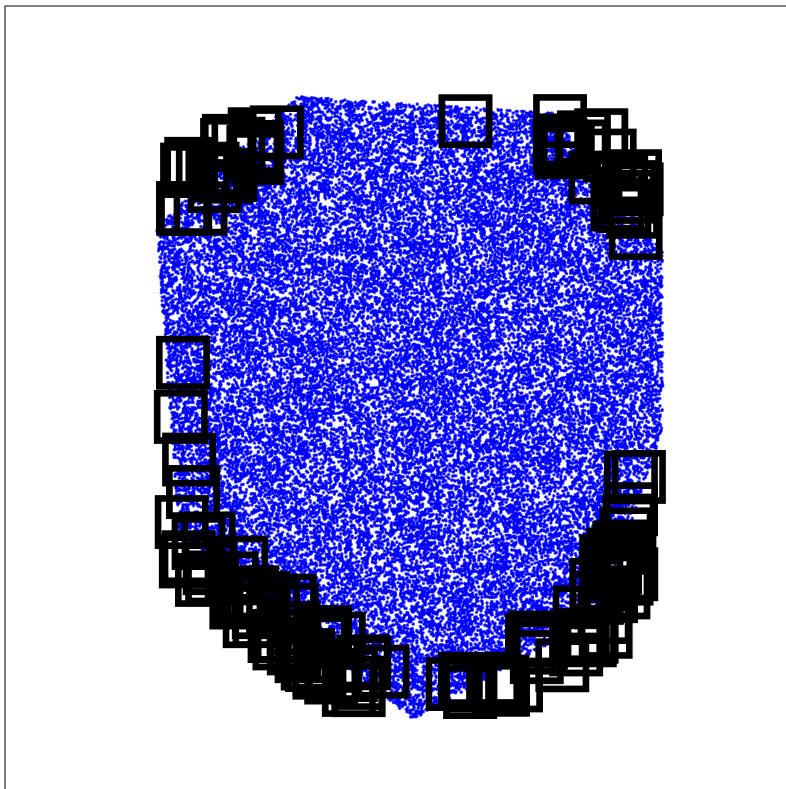


Figure S1: 40.000 random distributed points in a polygonal area. 1000 Ripley analysis were performed. The black squares represent the curves where the last 90% of the curve rose above the 30nm offset. At straight edges the distribution, thanks to the edge correction, is too random to rise above the 30nm offset.

CHAPTER 3

3D DIFFUSION MEASUREMENTS OF THE GLUCOCORTICOID RECEPTOR¹

Abstract

Single molecule imaging of proteins in a 2D environment like membranes has been frequently used to extract diffusive properties of multiple fractions of receptors. In a 3D environment the apparent fractions however change with observation time due to the movements of molecules out of the depth-of-field of the microscope. Here we developed a mathematical framework that allowed us to correct for the change in fraction size due to the limited detection volume in 3D single molecule imaging. We applied our findings on the mobility of activated glucocorticoid receptors in the cell nucleus, and found a freely diffusing fraction of 0.49 ± 0.02 . Our analysis further showed that interchange between this mobile fraction and an immobile fraction does not occur on time scales shorter than 150 ms.

3.1 INTRODUCTION

Since the initial camera-based observation of the diffusion of individual molecules in artificial membranes [1], single molecule imaging technology has yielded a plethora of novel insights into the behavior of proteins and other membrane constituents *in vitro* [2–4], *in cellulo* [5–11] and *in vivo* [12]. Single molecule microscopy has been of great importance to quantify the diffusive properties of membrane constituents. Diffusive properties consequently report faithfully about the local structural properties of the membrane, the activation state of signaling pathways [13], transport of membrane components [14], or cellular regulation processes [15,16]. For a homogeneous system in equilibrium, one would predict that the ensemble-averaged mobility is hence governed by

¹This chapter is based on: R. Harkes, V.I.P. Keizer, M.J.M. Schaaf and T.Schmidt, Depth-of-focus correction in single molecule data allows analysis of 3D diffusion of the glucocorticoid receptor in the nucleus. (PLOS ONE, 2015)

3.1 Introduction

multiple populations, each reflecting a distinct molecular state of its components. Indeed, experimental verifications of this prediction have ubiquitously been found. Whether particle-averaged mean-squared displacement analysis [17], molecular step-width distributions [18] or molecular squared-displacement distributions [19] were analyzed, multiple populations have always been found in the analysis of receptor mobility in cells.

Given that single molecule imaging permits to follow processes in time, there have been many attempts to find transitions between states that is to say, transitions in diffusive behavior. Those should show up as change in the fraction size of different mobility when changing the time of observation. Using gold [14] or quantum-dot labeling [20] of individual components, or by labeling larger structure like liposomes [21] long time scales could be covered and switching behavior has been observed.

Spurred by the success of single molecule imaging in membrane biology and biophysics, in recent years the technology has been further developed to permit single molecule observations of proteins in the 3D environment inside live eukaryotic cells [18,22,23]. In those experiments individual proteins were imaged over time, their position analyzed in 3D to sub-wavelength accuracy [24], and subsequently the mobility analyzed by step-length analysis. Similar to the membrane constituents, mobility of cytosolic proteins appeared inhomogeneous and fractions of different mobility were identified. Various research groups [18,22,23] realized that, unlike when imaging on the 2D membrane surface, the apparent fraction size of the various components depends on observation time. This is due to movements of molecules out of the depth-of-field of the observation volume: fast molecules will disappear faster compared to slow molecules (see Fig. 1). Given typical values for the depth-of-field of 1 μm for both wide-field [18,23] or selective-plane [22] illumination and typical diffusion constants of cytosolic proteins of 10 $\mu\text{m}^2/\text{s}$, the residency time of a molecule within the observation volumes reduces to <50 ms. Hence, in those earlier reports fraction sizes for short time-lags of 6.5 ms and 20 ms, respectively, were reported to avoid any 3D artifact [18,22,23].

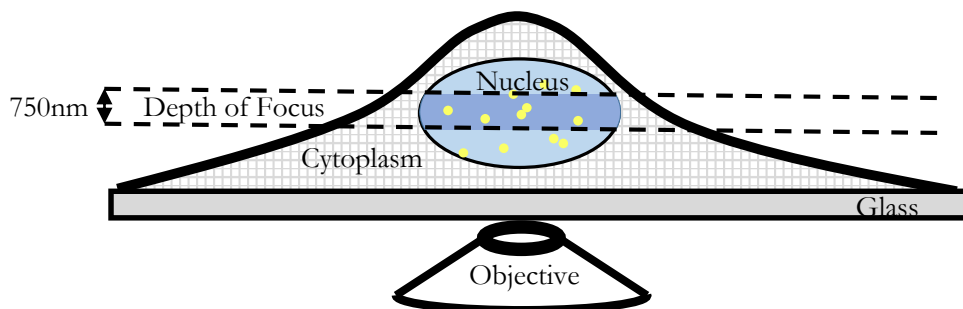


Figure 1: Imaging of diffusing fluorophores inside the nucleus. Since the depth of focus ($DOF = 750 \text{ nm}$) is shallow, molecules can diffuse in and out of the observation volume. This will deplete the relative contribution of the fast diffusing fraction to the analysis.

Here we present a mathematical framework that can correct for the change in fraction size due to the limited detection volume in 3D single molecule imaging. We applied our findings to data on the mobility of activated glucocorticoid receptors (GR) in the nucleus of monkey kidney (COS-1) cells. Our analysis showed that fraction sizes remain constant in the time-lag range from 6.5 ms to 150 ms, thus showing that switching between fractions occurs on longer time scales.

3.2 METHODS

3.2.1 Cell culture

To measure the diffusive properties of GR-eYFP COS-1 cells (acquired from ATCC) were cultured on coverslip glasses and transfected using X-tremeGENE (Roche, 500 ng DNA / 10 cm²) according to the manufacturers protocol. Three to six hours prior to measurement 1 μM dexamethasone (final concentration, Sigma-Aldrich) was added to the cells. Measurements were carried out at 37 $^{\circ}\text{C}$.

3.2.2 Single molecule imaging

Imaging of individual GR-eYFP was performed as described earlier [23]. In brief 1200, frames per cell were taken on an inverted wide-field fluorescence microscope (Axiovert 100TV) using a 100x/1.4NA oil-immersion objective (Zeiss). A region of interest of 50x50 pixels was selected (pixel size of 202 nm in the image plane). Cells were illuminated with 514 nm by a DPSL laser at an intensity of 2 kW/cm² (Coherent Sapphire). The exposure time was kept

3.2 Methods

constant at 3 ms and the time lag between two images varied between 6.25 and 75 ms by means of an acusto-optical tunable filter (AA optoelectronics). 45 cells were measured with 6.25 ms time lag between frames. 20 cells were measured with 25 ms lag time between frames. 16 cells were measured with 50 ms between frames. 16 cells were measured with 75 ms between frames.

The fluorescence signal from individual eYFP molecules was captured on an emCCD (Princeton Instruments, Trenton, NJ) using a combination of filters (DCLP530, HQ570/80 (Chroma Technology, Brattleboro, VT) and OG530-3 (Schott, Mainz, Germany). In order to obtain short acquisition times between frames of 6.25 ms the camera was run in kinetics-mode that permitted to capture 8 consecutive frames on the camera chip before being digitized. Subsequently, signals were fitted with a 2 dimensional Gaussian using a custom algorithm in Matlab [25]. The position of the molecules was obtained from the fitting parameters to an average accuracy of 34 ± 9 nm. The 2D distance between localizations could therefore be obtained with an accuracy of 68 nm.

3.2.3 Particle image correlation spectroscopy (PICS) analysis

At high densities a tracking algorithm mixes trajectories. The previously described method of particle image-correlation spectroscopy (PICS) circumvents this problem and is often used to analyze membrane diffusion [26].

In PICS the cumulative distribution function (cdf) of squared distances between frames separated at a given time-lag is calculated from the position data (fig 5D). The drop of the cdf at short distances reflects the mobility of molecules [26]. For a mobility characterized by diffusion the drop follows an exponential [19]. As has been reported earlier by us [27], the drop is faithfully described by a bi-exponential, which reflects the bi-modal behavior of the receptor: a freely diffusing receptor and an immobile, bound receptor.

For each measurement multiple time-lags are obtained by correlating not only subsequent frames but also further frames. However, due to photo bleaching the gap between frames cannot be increased indefinitely. Hence, the 6.25 ms dataset was analysed up to 5 steps (6.25-31.25 ms), the 25 ms dataset was analysed up to 4 steps (25-100 ms), the 50 and 75 ms datasets were analysed up to 2 steps (50-150 ms).

3.2.4 Depth of field calibration

The depth of field (DOF) is defined by the axial offset of a point-object from the focal plane at which the width is increased by a factor $\sqrt{2}$ [28]

$$\sigma(z) = \sigma_0 \sqrt{1 + \left(\frac{z}{DOF}\right)^2} \quad (1)$$

Eq (1) shows how the width, σ , of the PSF changes with the axial distance z from the focal plane. σ_0 is the width at the focal plane. Combining Eq. (1) with the expression for the width at focus one obtains an equation for DOF, which only includes σ_0 and the wavelength of light, λ :

$$DOF = 2 \frac{\pi * \sigma_0^2}{\lambda} \quad (2)$$

To experimentally obtain the DOF, eYFP molecules were coated on a glass slide. The sample was imaged for different axial positions of the objective by means of a piezo-actuator (PiFoc, PI). The fluorescent signal of single eYFP molecules was subsequently fitted [1]. From the fit the peak-width was obtained. The relation between axial position and peak-width was subsequently fitted as given by eq. (1) [25]. From this experiment the width at focus of $\sigma_0 = 263$ nm and the $DOF = 750$ nm, as defined by the axial position at which the width increases by $\sqrt{2}$, was determined (figure 2). The experimentally determined DOF is in agreement with that predicted from eq. (2) of 790 nm, given the experimental value for σ_0 and the emission wavelength of eYFP (550 nm).

3.3 Results

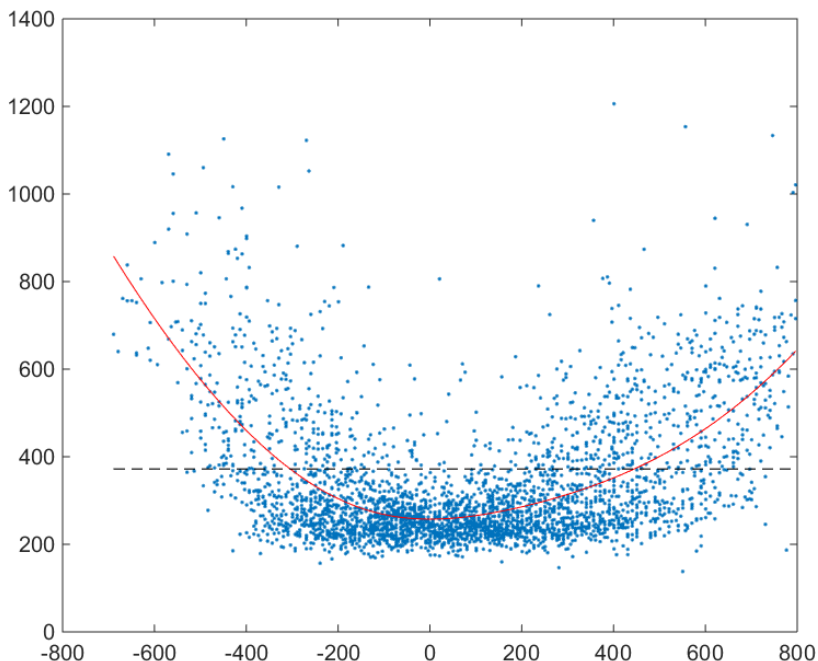


Figure 2: Calibration of the depth of field (DOF). eYFP was coated on a glass slide and the objective was moved by a piezo scanner. The resulting peak-widths were fitted as previously described [25]. The data were subsequently fit to eq. (1) yielding the signal width at focus, $\sigma_0 = 263$ nm and the DOF = 750 nm. All data characterized by a width larger than $\sqrt{2} \times 263$ nm = 372 nm (dashed line) were discarded from further analysis

In all further analysis localizations originating from fluorescent signal of width larger than $\sqrt{2} \times 263$ nm = 372 nm were discarded.

3.3 RESULTS

3.3.1 Analytical solution for correction of fraction size in 3D diffusion with limited detection volume

Since the width of the point-spread-function (PSF) increases with increasing distance to the focal plane, the signal from an out-of-focus object will be spread out over a larger region of the detector and the signal to noise ratio will decrease concomitantly. Therefore the detectability of a molecule is limited to a small distance from the focus defining the depth of field (DOF). The DOF was

measured to be 750 nm (Fig 2). With respect to detailed mobility analysis that includes various fractions, the limited DOF will result in a bias towards the slowest fraction. Fast diffusing molecules will have a higher chance of diffusing out of the DOF than slow diffusing molecules. Therefore they will have a smaller contribution to the cumulative distance distribution.

In what follows we derive an analytical solution for a system that consist of two fractions of diffusing objects characterized by diffusion constants D_1 and D_2 , and fractions α and $1-\alpha$, respectively. The description can easily be expanded to include more fractions.

For a molecule that is localized at axial position z_0 the probability density for its axial location z after a time t , with a diffusion constant of D is given by:

$$pdf(z, z_0, D, t) = \frac{1}{\sqrt{4\pi Dt}} e^{-\frac{(z-z_0)^2}{4Dt}} \quad (3)$$

Hence, the probability to stay within the DOF of length L is given by:

$$\begin{aligned} & \int_0^L \frac{1}{\sqrt{4 * \pi * D * t}} e^{-\frac{(z-z_0)^2}{4*D*t}} dz \\ &= \frac{1}{2} \left(erf \left(\frac{z_0}{\sqrt{4 * D * t}} \right) + erf \left(\frac{L - z_0}{\sqrt{4 * D * t}} \right) \right) \end{aligned} \quad (4)$$

with erf being the error function. Further integration over the start position z_0 from 0 to L results in the average probability to stay within the DOF:

$$\bar{P}(L, D, t) = erf \left(\frac{L}{\sqrt{4 * D * t}} \right) + \frac{\sqrt{4 * D * t}}{L\sqrt{\pi}} \left(e^{-\frac{L^2}{4*D*t}} - 1 \right) \quad (5)$$

Which finally leads to:

$$\bar{P} = erf(f) + \frac{1}{f\sqrt{\pi}} (e^{-f^2} - 1), f = \frac{L}{\sqrt{4 * D * t}} \quad (6)$$

3.3 Results

Eq. (6) describes the probability for a molecule that started inside the DOF to still reside within DOF after time t . Figure 3 shows the functional form for a realistic DOF of 750 nm and imaging time from 6.4 to 100 ms. The probability strongly depends on D , reducing even for short imaging times of 6.4 ms from $P(0.1\mu\text{m}^2/\text{s})=0.96$ to $P(2\mu\text{m}^2/\text{s})=0.83$, the range of diffusion constants typically reported. Following eq. (6) this effect becomes even more pronounced for longer imaging times.

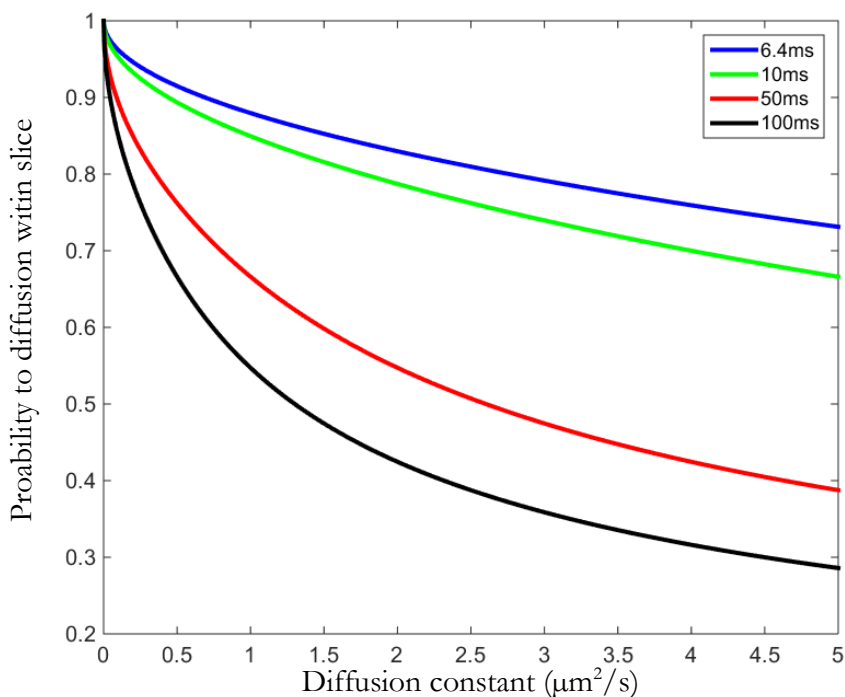


Figure 3: Result of formula 4 for a DOF of 750nm and four different lag times. For a diffusion constant of $2\mu\text{m}^2/\text{s}$ the probability to diffuse inside the DOF of 750nm after 10ms is calculated to be 79%. When two fractions have a different diffusion constant the apparent fast fraction needs to be corrected using equation 7.

In what follows we describe how eq. (6) is used to calculate the actual fraction size from imaging data in the case of multi-modal inhomogeneous diffusion data. By PICS analysis D_i , and the apparent fraction size, α_i , are obtained. Together with eq. (6) the real fraction sizes, β_i , are obtained:

$$\beta_i = \frac{x_i}{\sum_i x_i}, x_i = \alpha_i P_i \quad (7)$$

As required, both real and apparent fraction sizes are normalized quantities $\Sigma\alpha_i = \Sigma\beta_i = 1$.

For a two-component system eq. (7) simplifies to:

$$\beta = \frac{\alpha P_2}{(1 - \alpha)P_1 + \alpha P_2} \quad (8)$$

where β refers to the fraction with diffusion constant D_2 , and $1-\beta$ the fraction with diffusion constant D_1 .

3.3.2 Validation of the correction by simulations

To prove the correction method Monte-Carlo simulations were performed. 3000 molecules were split in two equal fractions, $\beta = 1-\beta = 0.5$. The fractions were characterized by diffusion constants of $D_1 = 2 \text{ pix}^2/\text{frame}$ and $D_2 = 0.05 \text{ pix}^2/\text{frame}$, respectively. Those values were chosen based on values typically found for diffusion of proteins in mammalian cells, and in particular are equivalent to the values for the bound and unbound fraction of the glucocorticoid receptor in the nucleus (2 and $0.5 \mu\text{m}^2/\text{s}$) reported earlier [23]. The objects used in the simulation were free to diffuse for 100 frames in a cube of $100 \times 100 \times 100$ pixels. Periodic boundary conditions were applied. In order to set a DOF, only molecules within a slice of 5 pixel width (i.e. $1 \mu\text{m}$) at the centre of the cube were considered.

Particle image correlation spectroscopy (PICS) utilizes the distance distribution of the diffusing particles. To analyse the simulation the distances originating from fast diffusing objects were summed and divided by the total number of distances found. The observed fractions were extracted for time lags of 1 to 10 frames. Figure 4 shows the result of this analysis (blue data). The apparent fraction size of the fast fraction decreased from 0.46 ± 0.01 at the first time lag to 0.36 ± 0.01 for the 10th time lag. Subsequently eq. (8) was used to correct the data and calculate the real fraction size. Figure 4 shows that our analysis faithfully

3.3 Results

follows the prediction and the real fraction size remains constant at $\beta = 0.500 \pm 0.007$ over the whole range of time lags (green data).

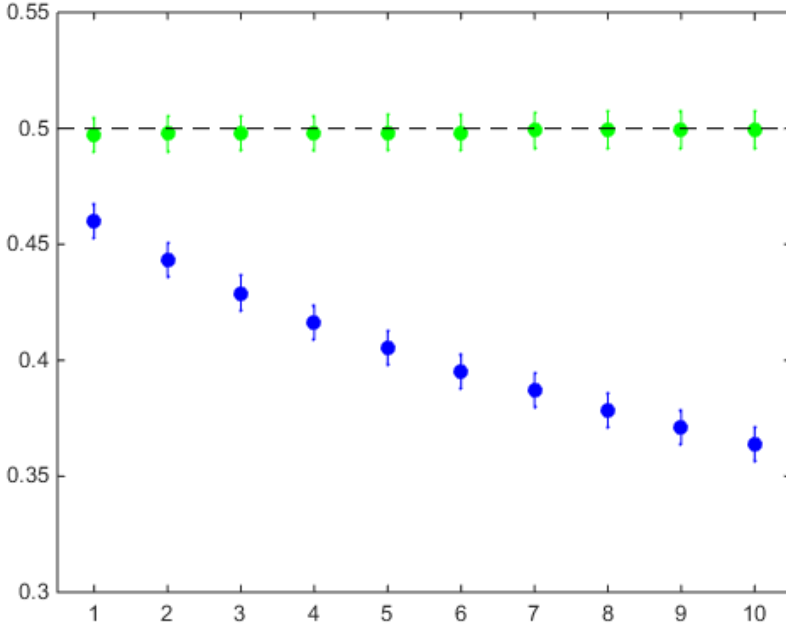


Figure 4: Simulation result that shows depletion of the fast fraction for increasing time lags. The time lag is given by the number of frames between detections. In blue the uncorrected result, in green the result after correction with eq.(8).

3.3.3 Validation of the correction using experimental data

To further prove our correction method we applied the model for the correction of experimentally acquired life-cell data. The diffusion of the glucocorticoid receptor (GR) in live cells is a well-documented example for mobility of multiple fractions in a 3D environment. The GR is an member of the steroid receptor family [29–31]. It mediates the effects of natural as well as synthetic glucocorticoids like dexamethasone and prednisolone, which are drugs known for their anti-inflammatory activity that is beneficial to treat diseases like asthma and rheumatoid arthritis [29]. Upon activation by glucocorticoids the receptor translocates from the cytoplasm to the nucleus. There it acts as a transcription factor. It binds to specific target sequences in the DNA to activate gene transcription.

The targeted search mechanism along DNA that activate or repress gene activation by hormone receptors like the GR has long been studied in theory and experiment [32]. The GR displays long immobilization times (2.3 s). The immobilized fraction probably reflects receptors bound to DNA in order to activate transcription. In addition, the GR is found to also have short immobilization times (0.7 s) [27]. Most likely the short immobilization times represents a search mechanism that includes non-specific DNA binding [31]. Finally, approximately half of the GR population shows fast free 3D diffusion [27].

Here we followed the wide-field single molecule imaging strategy of Groeneweg et al. [27] to analyze the diffusion properties of activated GR and extended our analysis up to 150 ms time-lags. Obviously, our current approach does not discriminate between the short (0.7 s) and long (2.3 s) immobilization times of the receptor due to the short time scale of the experiments. Hence, only two fractions were distinguished, an immobile and a freely diffusing fraction.

Below briefly stated are the steps taken to obtain data on GR mobility, which are also depicted in Fig. 5. COS-1 cells were transfected with a plasmid encoding a YFP-labeled version of the GR. The functionality of the plasmid has been tested previously [27]. Cells were stimulated with 1 μ M of dexamethasone which leads to efficient activation and translocation of the GR to the nucleus. Subsequently, individual YFP-GRs were followed using single molecule microscopy in which a mid-slice of 750 nm thickness of the nucleus was imaged (Fig. 5A; see the DOF subsection in M&M). Individual GRs appeared as diffraction-limited images of a signal of 203 ± 90 counts when illuminated for 3 ms at an intensity of 2 kW/cm² of 514 nm light (Fig. 5B). This signal allowed us to track the receptors at a lateral accuracy of 34 nm. The axial position was lost as the camera imaged the 2D projection of the 3D slice in the nucleus.

3.3 Results

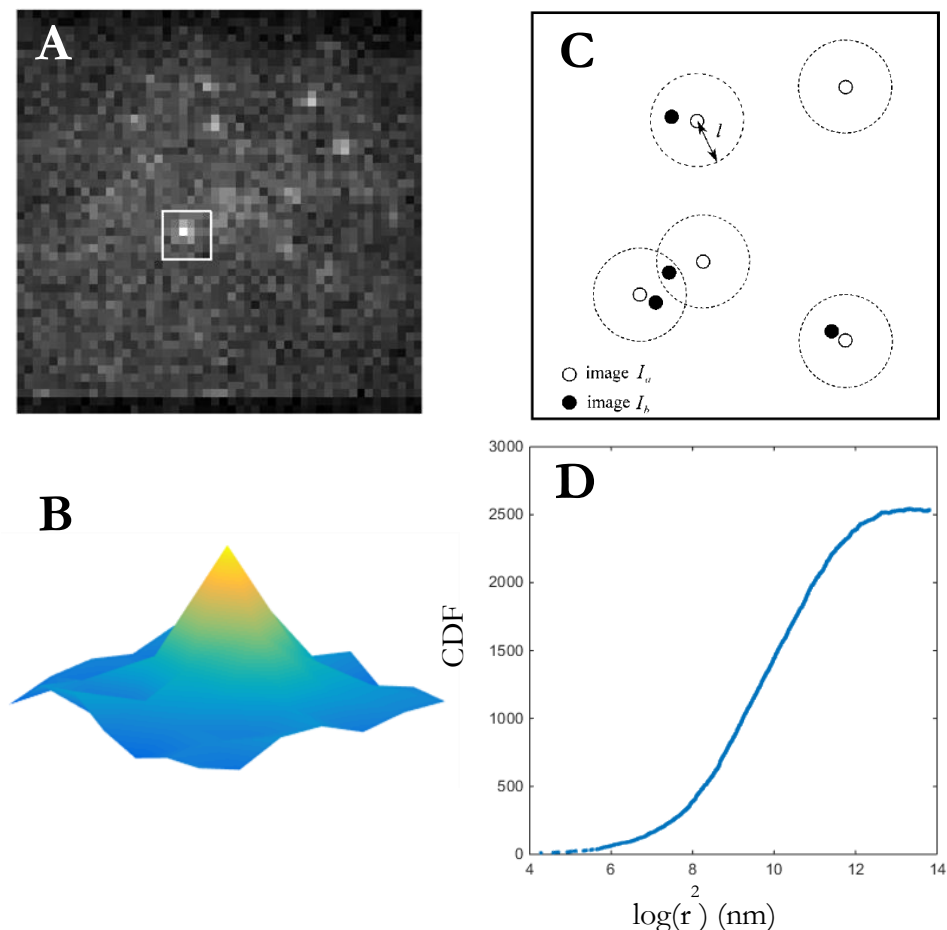


Figure 5: Single molecule imaging and PICS analysis.

A: Signal of individual eYFP-GR molecules on an emCCD camera.

B: The signal of an individual molecule is fitted to a Gaussian yielding the position, the width and the strength of the signal.

C: Distance calculation between molecules in subsequent frames.

D: Cumulative distribution function (cdf) of distances of molecules in subsequent frames correlated by diffusion.

Subsequently PICS analysis was used to analyze the mobility of the GR (fig 5C). In PICS the cumulative squared-distance distributions (cdf) in subsequent frames is calculated from position data (fig 5D). The drop of the cdf at short squared-distances reflects the mobility of the molecules [26]. For diffusion the drop follows an exponential [19]. As has been reported by us earlier [27], the drop is faithfully described by a bi-exponential, which reflects the bi-modal behavior of the receptor: a freely diffusing receptor and a bound receptor.

PICS analysis was performed for time lags between 6.25 and 150 ms. For each time lag the diffusion constant and apparent fraction size of the two components was determined. The diffusion constants were found to be 0.67 ± 0.1 and $0.043 \pm 0.004 \mu\text{m}^2/\text{s}$ for the fast and immobile fraction, respectively. Our data are in excellent agreement to our earlier findings [27], and the prediction for a free diffusion process. It should be noted that the immobile fraction found in single molecule experiments consist of two sub-fractions which can be distinguished only at time-lags beyond 1 s as accessible by fluorescence recovery after photobleaching (FRAP) experiments. In FRAP it was found that those two fractions reflect two binding modes of the receptor to DNA, are equal in size, and are characterized by immobilization times of 0.7 and 2.3 s, respectively [31].

As previously observed [27] the apparent fraction of the fast fraction α dropped from 0.46 ± 0.02 at 6.5 ms to 0.37 ± 0.02 at 150 ms (Fig. 6, blue data). After correction to the real fraction size, as given by eq. (8), it is obvious that the size of the two fractions does not change in the time frame between 6.5 and 150 ms (Fig. 6, green data). The real fraction size is constant and amounts to $\beta = 0.49 \pm 0.02$.

Even though the different mobility modes for various transcription factors have been repeatedly reported, it has remained challenging to address the timescales on which switching between the modes occurs [22,23,27,33–35]. The observed drop in fraction size in the uncorrected data could have been misinterpreted as an indication of switching behavior. However, since in the corrected data the fraction size does not change with increasing time lag, we conclude that switching between the two modes does not occur within the time frame of 150 ms.

3.4 Conclusion

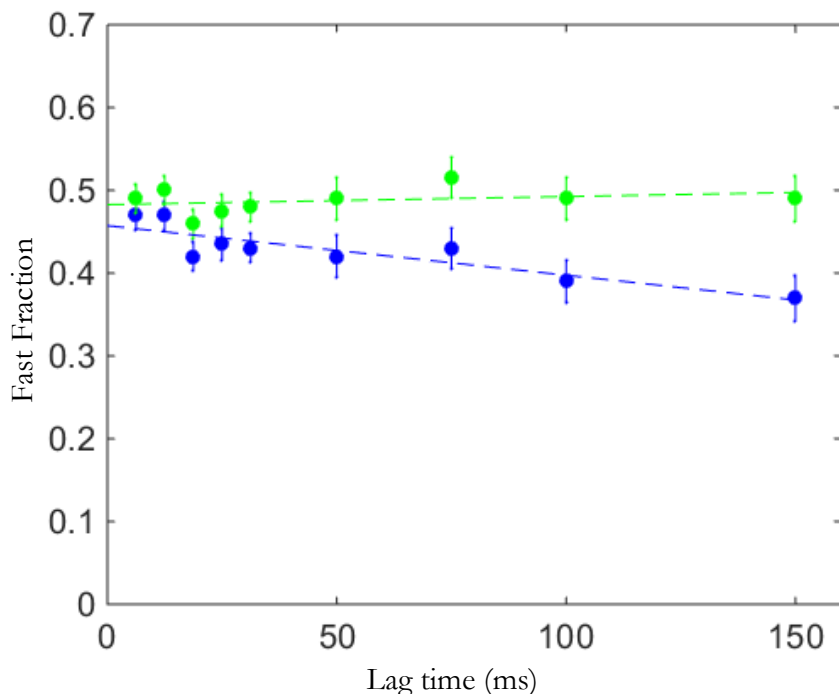


Figure 6: PICS analysis of glucocorticoid receptor at different time lags. In blue the uncorrected result. A decrease of the fast fraction is observed. In green the result corrected by eq.(8) taking into account the DOF. The fast fraction stays constant for time lags at least up to 150 ms. Dashed lines are linear fits to the data. Error-bars represent the standard deviation

3.4 CONCLUSION

We showed that a depletion of fast mobile fractions is observed when multiple diffusive fractions are analysed using imaging methods that have limited axial reach. We developed a mathematical framework to correct for the experimental limitations that allowed us to calculate the real fraction sizes. Results have been validated by simulation and applied to experimental data of the activated glucocorticoid receptor in the cell nucleus. These results show that the reduction of the fast fraction with time lag, observed for the uncorrected data, is faithfully rectified by using the novel correction method. The corrected data indicate that the size of the freely diffusing fraction of dexamethasone-activated glucocorticoid receptors in the cell nucleus is 0.49 ± 0.02 . Since the corrected data show that this fraction size is constant for at least 150 ms we conclude that the receptor does not switch between this freely diffusing and an immobile (DNA-bound) state on this time scale. Thus, our theoretical framework not only allows

the determination of correct fraction sizes, but provides information on potential time scale for exchange between various fractions.

3.5 REFERENCES

- [1] T. Schmidt, G. J. Schütz, W. Baumgartner, H. J. Gruber, and H. Schindler, *Proc. Natl. Acad. Sci. U.S.A.* **93**, 2926 (1996).
- [2] T. Funatsu, Y. Harada, M. Tokunaga, K. Saito, and T. Yanagida, *Nature* **374**, 555 (1995).
- [3] S. Wennmalm, L. Edman, and R. Rigler, *Proc. Natl. Acad. Sci. U.S.A.* **94**, 10641 (1997).
- [4] H. P. Lu, L. Xun, and X. S. Xie, *Science* **282**, 1877 (1998).
- [5] Y. Lill, K. L. Martinez, M. A. Lill, B. H. Meyer, H. Vogel, and B. Hecht, *Chemphyschem* **6**, 1633 (2005).
- [6] G. J. Schütz, G. Kada, V. P. Pastushenko, and H. Schindler, *EMBO J.* **19**, 892 (2000).
- [7] Y. Sako, S. Minoghchi, and T. Yanagida, *Nat. Cell Biol.* **2**, 168 (2000).
- [8] F. Pinaud, X. Michalet, G. Iyer, E. Margeat, H.-P. P. Moore, and S. Weiss, *Traffic* **10**, 691 (2009).
- [9] P.-F. F. Lenne, L. Wawrezynieck, F. Conchonaud, O. Wurtz, A. Boned, X.-J. J. Guo, H. Rigneault, H.-T. T. He, and D. Marguet, *EMBO J.* **25**, 3245 (2006).
- [10] S. Courty, C. Luccardini, Y. Bellaïche, G. Cappello, and M. Dahan, *Nano Lett.* **6**, 1491 (2006).
- [11] G. Giannone, E. Hosy, F. Levet, A. Constals, K. Schulze, A. I. Sobolevsky, M. P. Rosconi, E. Gouaux, R. Tampé, D. Choquet, and L. Cognet, *Biophys. J.* **99**, 1303 (2010).
- [12] M. J. Schaaf, W. J. Koopmans, T. Meckel, J. van Noort, B. E. Snaar-Jagalska, T. S. Schmidt, and H. P. Spaink, *Biophys. J.* **97**, 1206 (2009).
- [13] P. H. Lommerse, B. E. Snaar-Jagalska, H. P. Spaink, and T. Schmidt, *J. Cell. Sci.* **118**, 1799 (2005).
- [14] A. Kusumi, Y. Sako, and M. Yamamoto, *Biophys. J.* **65**, 2021 (1993).
- [15] M. Ueda, Y. Sako, T. Tanaka, P. Devreotes, and T. Yanagida, *Science (New York, N.Y.)* **294**, 864 (2001).
- [16] S. de Keijzer, A. Sergé, F. van Hemert, P. H. Lommerse, G. E. Lamers, H. P. Spaink, T. Schmidt, and B. E. Snaar-Jagalska, *Journal of Cell Science* **121**, 1750 (2008).
- [17] C. Dietrich, B. Yang, T. Fujiwara, A. Kusumi, and K. Jacobson, *Biophys. J.* **82**, 274 (2002).
- [18] T. Kues, R. Peters, and U. Kubitscheck, *Biophys. J.* **80**, 2954 (2001).
- [19] G. J. Schütz, H. Schindler, and T. Schmidt, *Biophys. J.* **73**, 1073 (1997).
- [20] A. Cambi, D. S. Lidke, D. J. Arndt-Jovin, C. G. Figdor, and T. M. Jovin, *Nano Lett.* **7**, 970 (2007).
- [21] S. Coppola, L. C. Estrada, M. A. Digman, D. Pozzi, F. Cardarelli, E. Gratton, and G. Caracciolo, *Soft Matter* **8**, 7919 (2012).
- [22] J. C. Gebhardt, D. M. Suter, R. Roy, Z. W. Zhao, A. R. Chapman, S. Basu, T. Maniatis, and X. S. Xie, *Nat. Methods* **10**, 421 (2013).
- [23] M. E. Van Royen, W. A. van Cappellen, B. Geverts, T. Schmidt, A. B. Houtsmuller, and M. J. Schaaf, *J. Cell. Sci.* **127**, 1406 (2014).

- [24] L. Holtzer, T. Meckel, and T. Schmidt, *Applied Physics Letters* **90**, 053902 (2007).
- [25] B. Huang, W. Wang, M. Bates, and X. Zhuang, *Science* (New York, N.Y.) **319**, 810 (2008).
- [26] S. Semrau and T. Schmidt, *Biophys. J.* **92**, 613 (2007).
- [27] F. L. Groeneweg, M. E. van Royen, S. Fenz, V. I. Keizer, B. Geverts, J. Prins, E. R. de Kloet, A. B. Houtsmuller, T. S. Schmidt, and M. J. Schaaf, *PLoS One* **9**, e90532 (2014).
- [28] W. Demtröder, *Laser Spectroscopy* (Springer, 1988).
- [29] S. C. Biddie, B. L. Conway-Campbell, and S. L. Lightman, *Rheumatology* (Oxford, England) **51**, 403 (2012).
- [30] M. Beato and J. Klug, *Human Reproduction Update* **6**, 225 (2000).
- [31] G. L. Hager, J. G. McNally, and T. Misteli, *Molecular Cell* **35**, 741 (2009).
- [32] J. D. McGhee and P. H. von Hippel, *Journal of Molecular Biology* **86**, 469 (1974).
- [33] M. Becker, C. Baumann, S. John, D. A. Walker, M. Vigneron, J. G. McNally, and G. L. Hager, *EMBO Reports* **3**, 1188 (2002).
- [34] T. Morisaki, W. G. Müller, N. Golob, D. Mazza, and J. G. McNally, *Nature Communications* **5**, 4456 (2014).
- [35] D. Mazza, A. Abernathy, N. Golob, T. Morisaki, and J. G. McNally, *Nucleic Acids Research* **40**, e119 (2012).

3.5 References

CHAPTER 4

DIRECT OBSERVATION OF α -SYNUCLEIN AMYLOID AGGREGATES¹

Abstract

Aggregation of α -synuclein has been linked to both familial and sporadic Parkinson's disease. Recent studies suggest that α -synuclein aggregates may spread from cell to cell and raise questions about the propagation of neurodegeneration. While continuing progress has been made characterizing α -synuclein aggregates *in vitro*, there is a lack of information regarding structure of these species inside the cells. Here, we use confocal fluorescence microscopy in combination with super-resolution microscopy to investigate α -synuclein uptake when added exogenously to SH-SY5Y neuroblastoma cells, and to probe *in situ* morphological features of α -synuclein aggregates with near nanometer resolution. We were able to follow the uptake of α -synuclein aggregates by the cells and their partial degradation at a molecular level. Our data show that the cellular uptake via endocytosis is rapid. Once the aggregates are internalized, they accumulate in lysosomes where they are degraded. No further aggregation was observed inside the lysosomes as speculated in literature, nor in the cytoplasm of the cells. These results show the importance of the lysosome-dependent mechanism for protecting the cells from exposure to potentially toxic α -synuclein.

¹This chapter is based on: Mihaela M. Apetri, Rolf Harkes, Vinod Subramaniam, Gerard W. Canters, Thomas Schmidt and Thijs J. Aartsma, Direct observation of α -synuclein amyloid aggregates in endocytic vesicles of neuroblastoma cells
Submitted to FEBS letters

4.1 INTRODUCTION

Progressive accumulation and deposition of specific protein aggregates is a characteristic of many neurodegenerative disorders, including Parkinson's disease (PD). In PD, α -synuclein (α -syn), a small presynaptic protein (~ 15 kDa), is the main fibrillar component of the intraneuronal protein aggregates (Lewy bodies) that represent the pathological feature of this disease[1]. Although α -syn is predominantly a cytosolic protein, recent studies suggest the protein exerts not only a pathogenic effect inside the cells, but an extracellular pathogenic action as well. Multiple forms of α -syn have been observed in cerebrospinal fluid, blood plasma and more recently, in saliva[2–4]. When applied to cultured cells, α -syn preformed aggregates are internalized via endocytosis and targeted to the lysosomes for degradation[5–9]. The extent of aggregate accumulation inside cells is determined by the cells ability to degrade and remove the aggregates. Few groups reported that α -syn take-up from the extracellular space induces the aggregation of the endogenous protein, leading to the formation of Lewy body-like inclusions[9–12]. Cell to cell transmission of α -syn pathological aggregates has been demonstrated in neuronal cultured cells as well as in animal models[13,14]. They show this is most likely through sequential exocytosis and endocytosis.

At this moment, the fate of the exogeneous α -syn aggregates once they enter the cells is not clear. Are the aggregates degraded in the lysosomes, or do they start growing into larger α -syn aggregates? Do they overload the degradation systems impairing their activity and escape in the cytosol inducing aggregation of the endogeneous protein? In order to address these questions, we followed directly the uptake and fate of α -syn preformed aggregates when added to neuroblastoma cells, SH-SY5Y, by super-resolution microscopy.

While atomic force microscopy (AFM) has been extensively used to obtain the ultrastructure and morphological features of the amyloid aggregates, the technique has the drawback to be applicable only *ex situ*. In contrast, optical microscopy and in particular the new super-resolution methods are powerful and non-invasive techniques for the study of morphological features of the amyloid aggregates with nanometer resolution. In the last years, these optical techniques have been successfully used in several studies to probe the morphology of protein aggregates *in vitro*[15–17] and in cells[18–20].

Here we applied confocal fluorescence microscopy and optical super-resolution microscopy to follow and characterize the fate of small *in vitro* assembled α -syn

fibrils in human neuroblastoma cells. We found that fibrils were partially degraded when trafficked through the lysosomal pathway. Further fibril maturation and formation of long fibrils was not observed. Our study thus highlights the potential role of lysosomal degradation in the prevention of α -syn aggregation in cells.

4.2 MATERIALS AND METHODS

4.2.1 Preparation of labeled α -syn fibrillar seeds

Recombinant human wild type α -syn was expressed and purified as described previously[21]. Fibrils were formed at 37 °C in 1.5 ml Eppendorf tubes under constant agitation (1000 rpm, in an Eppendorf Thermomixer comfort, Eppendorf AG, Germany). 300 μ L of 70 μ M α -syn in phosphate buffer saline (PBS) was incubated for 5 days. The presence of amyloid fibrils was confirmed by thioflavin T fluorimetry and atomic force microscopy. Labeling of α -syn fibrils with the NHS ester (succinimidyl ester) of Alexa Fluor 532 was performed according to the manufacturer's instructions (Life Technologies, USA). Briefly, α -syn fibril solution was incubated for 1 h at room temperature with Alexa Fluor 532 dye in a 1:1 protein/ fluorophore molar ratio. The unbound dye was removed by pelleting the fibrils at 13000 rpm for 15 min in a tabletop centrifuge. The supernatant was discarded and the pellet containing labeled fibrils was resuspended in PBS. The centrifugation/resuspension cycle was repeated twice. Purified labeled α -syn fibrils were divided in 20 μ L aliquots, flash frozen and stored at -80 °C. Fibrillar seeds of α -syn were produced as follows: 20 μ L of labeled fibrils were diluted 10 times in PBS and sonicated 3 \times 5 s with a probe sonicator (Sonics & Materials, Inc., USA) using 50% maximum power, yielding variable fibril lengths of approximately 350 nm. These seeds were added immediately in the culture medium of SH-SY5Y cells at a final concentration of 100 nM, and their uptake by the cells was followed in time using confocal microscopy and direct stochastic optical reconstruction microscopy (dSTORM).

4.2.2 Cell culture

Human neuroblastoma cells, SH-SY5Y, (gift of Mireille M. A. E. Claessens, University of Twente, Netherlands) were grown in 1:1 minimum essential media (MEM) (Gibco by Life Technologies, USA) and nutrient mixture Ham's F-12 (PAN Biotech, Germany) free of phenol red, supplemented with 1% MEM, non-essential amino acids, 2mM Glutamax and 15% fetal bovine serum (Gibco by Life Technologies).

4.2.3 Atomic force microscopy (AFM)

Labeled α -syn fibrillar samples were diluted 5 times into PBS, and 10 μ L were pipetted onto freshly cleaved mica and kept at room temperature for 60 s. The mica surface was then rinsed with Millipore-filtered water (2 \times 50 μ L) to remove loosely bound protein, dried under a stream of nitrogen and imaged immediately.

AFM imaging was performed on a MultiMode Nanoscope IIIa microscope (Digital Instruments, USA) equipped with an E-scanner. All measurements were carried out in the tapping mode under ambient conditions using single-beam silicon cantilever probes with a resonant frequency of 300 kHz (Olympus, Japan). Image analysis was performed using the instrument software.

4.2.4 Co-localization experiments with lysosomes

SH-SY5Y cells were incubated with 50 nM LysoTracker® Deep Red (Life Technologies) for 30 min at 37 °C, then washed and incubated further with 100 nM Alexa532-labeled α -syn sonicated fibrils. Cells were imaged live after α -syn seeds addition, using an adapted confocal spinning-disk setup based on an Axiovert 200 body microscope (Zeiss, Germany) with a spinning disk confocal unit (CSU-X1 Yokogawa, Japan) and a back-illuminated EMCCD camera (iXON 897, Andor, UK) on the side port. The temperature was kept at 37 °C with constant 5% CO₂ concentration in a stage-top incubator (Tokai Hit, Japan). Illumination was performed with two different lasers of wavelength 514 nm (Cobolt, Sweden) and 642 nm (Spectra-Physics, USA).

4.2.5 dSTORM experiments and data analysis

In vitro prepared α -syn fibrils, labeled with Alexa 532, were spin coated onto a glass coverslip in 1% poly vinyl alcohol (Sigma Aldrich) and imaged. Imaging was performed in a switching buffer solution: 100 mM mercaptoethylamine (Sigma Aldrich) in PBS (pH 8.0) [22]. On day before imaging, SH-SY5Y were plated at 10⁵ cells on 35 mm ibidi treated glass bottom dishes (ibidi GmbH, Germany) and then incubated with 100 nM final concentration of α -syn seeds labeled with Alexa 532. Cells were fixed in 4% formaldehyde at different incubation times and then imaged in the switching buffer.

dSTORM set-up

Super-resolution imaging was performed on a home-built wide-field single molecule setup, based on an Axiovert S100 Zeiss inverted wide-field microscope equipped with a 100x 1.4 NA oil-immersion objective (Zeiss, Germany). The Alexa 532 dye was excited using a 532 nm laser (Cobolt, Sweden). A 405 nm laser (CrystaLaser, USA) was used for photo-switching and to adjust the density of visible fluorophores. The light was reflected into the objective by the dichroic mirror ZT405/532/635rpc (Chroma, USA). The fluorescence light in the detection path was filtered using the emission filter ZET532/633m (Chroma, USA). Conversion intensities were in between 0 and 20 W/cm² at 405 nm and

4.2 Materials and methods

the excitation intensity was 3 kW/cm² at 532 nm. For each sample, we acquired 10000 single molecule images with an acquisition time of 10 ms per frame and a frame rate of 87 Hz. The signal of individual dye molecules was captured on a sCMOS Orca Flash 4.0V2 camera (Hamamatsu, Japan) (Fig.1a). The average integrated signal of a single dye molecule was 447 detected photons (Fig.1d), spatially distributed by the 2 dimensional point-spread-function of the microscope of 293 nm FWHM (Fig.1c).

Data analysis

The signal from individual fluorophores (Fig.1c) was fitted with a 2 dimensional Gaussian using a custom least-squares algorithm in Matlab[23]. From the fit we determined the location of each molecule to high accuracy of 11 nm on average (Fig.1b). The localization accuracy coincides with the value predicted from the width of the point-spread-function and the detected number of photons, $293 \text{ nm} / \sqrt{[447]} = 14 \text{ nm}$. Subsequently, the localization data were used to generate super-resolution images. Super-resolution images were obtained by binning localizations into 20x20 nm² bins. For zoom-ins we used probability density maps in which each localization was represented as a normalized Gaussian centered at the position and of width given by the sigma-uncertainty in localization. The pixel size was chosen to represent 1x1 nm².

For analysis of fiber width and length we used line fitting from the raw localization data. We selected a region of interest (ROI) around a fibril. The selected localizations were rotated and subsequently the y-coordinates of the localizations were binned. The full width at half-maximum (FWHM) was calculated from the resulting histogram (see supplemental Fig.S1). Given that localizations in dSTORM experiments had an average positional accuracy of 11 nm (Fig.1b), leading to an apparent FWHM of $11 \times 2 \sqrt{[2 \times \log(2)]} = 26 \text{ nm}$ for any point object. The apparent FWHM of the fiber was therefore de-convolved to give the true fiber width, $\text{FWHM}_d = \sqrt{[\text{FWHM}^2 - (26 \text{ nm})^2]}$.

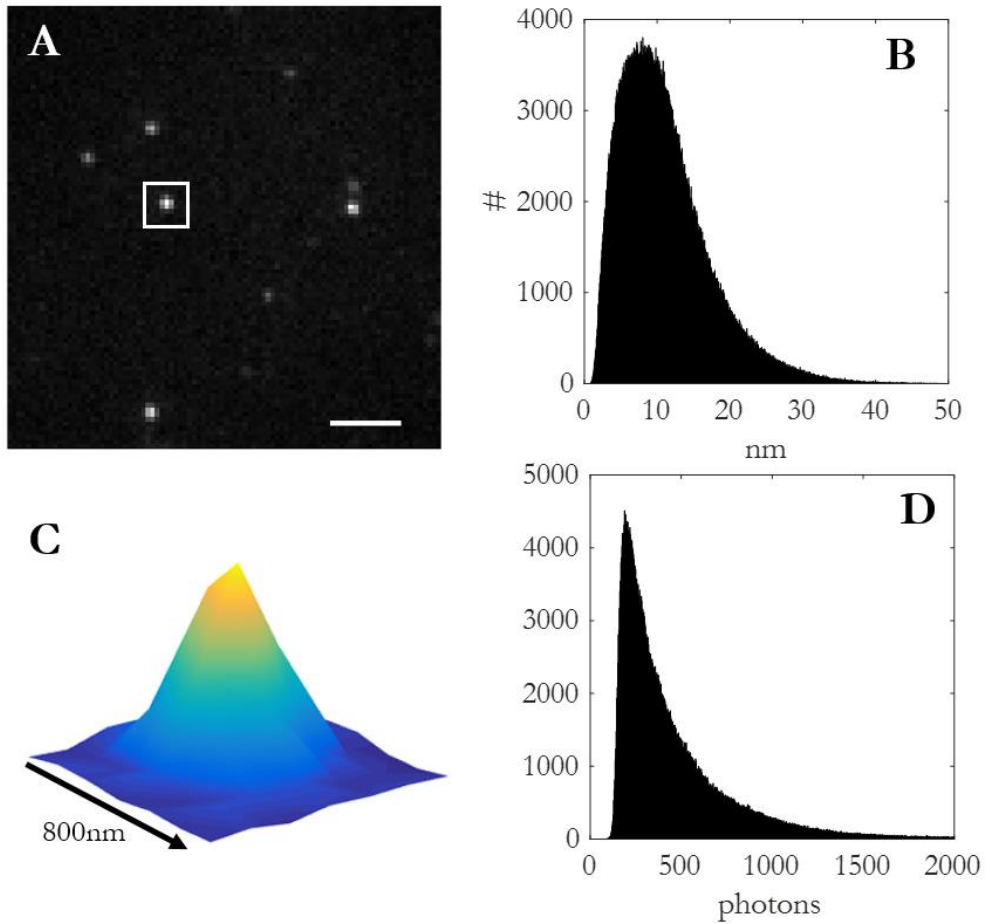


Figure 1: Characteristic properties of the optical setup. (a) Frame with the signal of several Alexa532 molecules. Scale bar = $2\mu\text{m}$. (b) Histogram of the sigma of positional accuracy (Mean: 11 nm). (c) Zoom-in of the white square in figure 1a showing the Gaussian intensity profile. (d) Histogram of the intensity of localizations (Mean: 447 photons).

4.3 RESULTS AND DISCUSSION

4.3.1 Super-resolution imaging of *in vitro* α -syn fibrils

In this study we used direct stochastic reconstruction microscopy (dSTORM) to follow the uptake of α -syn aggregates by SH-SY5Y human neuroblastoma cells. dSTORM has been used in several studies to probe the morphology of protein aggregates such as $A\beta$ -aggregates in Alzheimer's disease[18,19], Huntington's protein aggregates in Huntington's disease[15,24] and α -syn amyloid fibrils in Parkinson's disease (PD) [16]. In relation to earlier studies, we here used direct fluorescence labeling of α -syn by switchable fluorophores. Direct labeling is advantageous when compared to other superresolution methods which typically involve immunofluorescence labeling, the latter leading to substantial increase in structure size due to the antibody size (~ 10 nm) as compared to the small size of fluorescent dyes used in the current study.

We first characterized the properties of α -syn amyloid *in vitro* fibrils prepared in our conditions. Figure 2 shows the morphology of labeled intact α -syn fibrils as obtained by AFM (Fig. 2a) and by dSTORM (Fig. 2b) when deposited at low concentration onto a flat substrate. Individual fibrils were clearly identified in both methods. The overall images appear very comparable. The length of the fibrils clearly exceeded $1 \mu\text{m}$ extending to $10 \mu\text{m}$ and longer. In view of the complex topology of the fibrous network with fiber crossings, a detailed statistical analysis of fiber length was omitted.

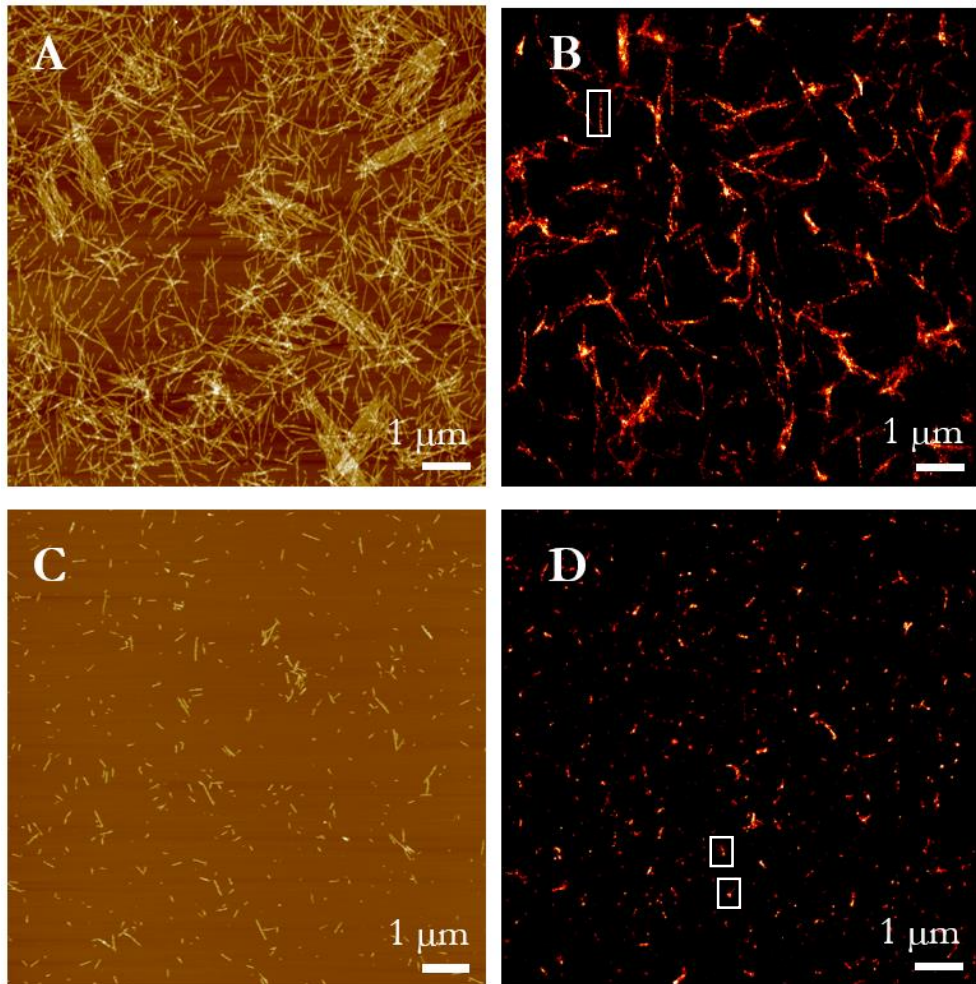


Figure 2: Super-resolution imaging of the *in vitro* prepared α -syn fibrils. (a) AFM and (b) dSTORM images of intact wild-type α -syn fibrils covalently labeled with the NHS derivate of Alexa 532 fluorophore. (c) AFM and (d) dSTORM images of sonicated labeled α -syn fibrils.

The apparent width of the fibers was determined from the dSTORM images as detailed in the materials and methods sub-section. A zoom-in of the fibril marked in figure 2b is shown in figure 3a. From the histogram of localizations (Fig. 3b) the apparent width of the fiber was 47nm FWHM (dashed red line). The distribution of apparent widths for 38 fibrils is shown in figure 3c. The distribution is characterized by a mean of FWHM = 43 ± 12 nm. Deconvolution leads to the real fiber widths of 34 ± 12 nm. This result by optical microscopy was compared to results by AFM experiments. In AFM experiments, we used

4.3 Results and discussion

the height information to estimate the diameter of the labeled α -syn fibrils. The height approach is generally assumed more accurate than measurements of the width as of tip-convolution[25]. The mean height was found to be 8 ± 1 nm for the labeled α -syn fibrils (mean \pm s.e. from 50 fibers, see supplemental Fig.S2). The apparent discrepancy in fiber widths between the two methods seems not too surprising. It is well known that AFM underestimates heights of nanometer size objects such as proteins[26], due to sample deformation and/or dehydration.

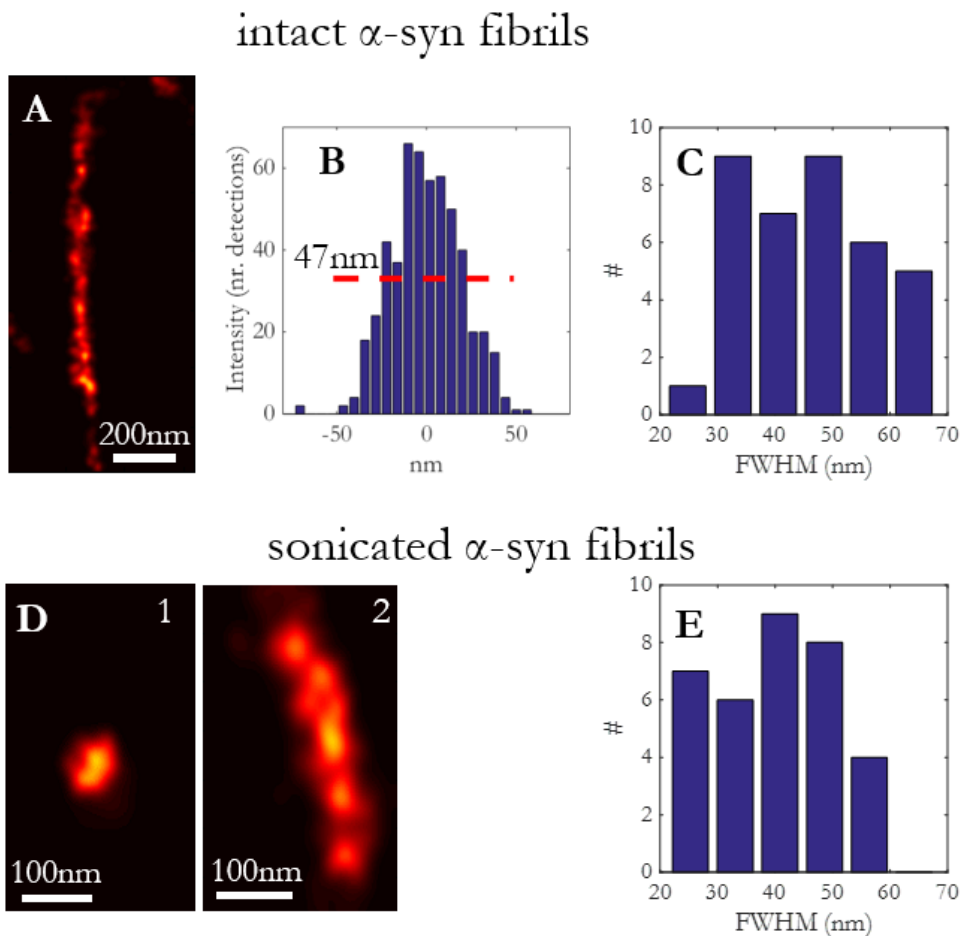


Figure 3: Characterization of different sized α -syn fibrils by dSTORM. (a) Detailed view of an intact α -syn - Alexa532 fibril (the marked fibril from figure 2b). (b) Histogram corresponding to the localization data (see supplementary figure 1 for details on the method). A FWHM of 47nm was calculated. (c) Histogram distribution of FWHM for intact α -syn fibrils. A mean diameter of 43.4 ± 12.3 nm was calculated from FWHM data (> 25 fibrils). (d) dSTORM images of two different sized sonicated fibrils (the marked

sonicated fibrils from figure 2d). (e) Histogram distribution of FWHM for sonicated α -syn fibrils. The mean diameter of α -syn sonicated fibrils was 42 ± 11 nm.

α -Syn aggregates have been reported to be internalized into a variety of cell types, including neurons[7,9,12]. It has been shown that the uptake is more efficient if the aggregates are smaller. For this reason, α -syn fibrils were sonicated prior to their addition to the cells. The effect of sonication on fibril size is already apparent in Figure 2. Whereas fibril length clearly exceeds $1 \mu\text{m}$ for the intact fibrils (Fig. 2a&b), after sonication the length shortened to $<1 \mu\text{m}$ (Fig. 2c&d) independent of the imaging method used. The lengths of the sonicated fibrils determined by AFM were between 50 and 700 nm. The lengths determined by dSTORM were similar, and in the range between 30 and 650 nm. The smaller length fibrils appear as globular (Fig. 3d 1) whereas the longer structures as clear fibrils (Fig. 3d 2). While sonication led to a significant decrease in fibril length, the fibril width was unchanged. The distribution of sonicated fibril width, as shown in Figure 3e, is characterized by a mean of 42 ± 11 nm, which leads, after deconvolution, to a real width of FWHM_d of 32 ± 11 nm.

4.3.2 Internalization of extracellular α -syn fibrils into neuronal cells

Having established that we were able to distinguish small sized α -syn aggregates *in vitro*, we moved further to study the fate of the aggregates once they are exogenously added to cells in culture. We investigated the uptake of the small fibrillar α -syn aggregates labeled with Alexa-532 dye by the SH-SY5Y human neuroblastoma cells using confocal fluorescence microscopy.

The time-course of uptake is seen in figure 4. Sonicated, labeled seeds were added at a concentration of 100 nM to the culture medium and left during the experiment. Their uptake by SH-SY5Y cells was followed in time using confocal microscopy and dSTORM. In the first 2 hours α -syn aggregates were mostly present at the cell membrane resulting in images that resemble typical images of the cell's outline (Fig. 4 left&middle). After 24 hours Alexa532-syn aggregates disappear from the outer cell membrane and localize as granular intracellular deposits mostly close to the nucleus (Fig. 4 right). This observation suggests that fibrils were internalized and probably processed in the endosomal pathway towards perinuclear lysosomes. This interpretation is supported by dual color experiments which showed that the granular deposits (Fig. 4 green) colocalized with a marker for acidic organelles, such as lysosomes (LysoTracker; Fig. 4 red). Hence, our data confirm earlier results which suggested that protein aggregates

4.3 Results and discussion

like α -syn are transported towards the lysosomal compartment for degradation and clearance[6,7].

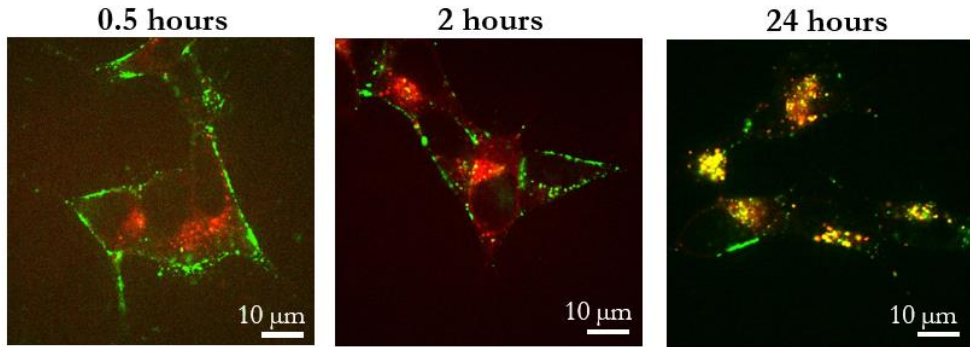


Figure 4: Internalization of α -syn sonicated fibrils in human neuroblastoma cells. Images show co-localization of Alexa 532 labeled α -syn aggregates (green) with the lysosomes labeled with LysoTracker® Deep Red (red). SH-SY5Y cells were treated with 50nM LysoTracker® Deep Red, then washed, incubated further with Alexa532-labeled α -syn sonicated fibrils and imaged live on a confocal microscope.

Subsequently we addressed whether maturation and increase in aggregation of fibrils occurred while transported from the plasma membrane to the endosomes/lysosomes. Whether and how maturation occurs and whether that will lead to some equilibrium distribution of aggregates, monomers and degraded peptide in cells when being continuously exposed to an extracellular concentration is still unclear. One proposed mechanism for maturation, that has been linked to disease, is that fibrils further aggregate inside the acidic endocytic vesicles as the combination of low pH and high effective concentration are favorable conditions for α -syn aggregation[27]. Further it is unclear whether such maturation would lead to the formation of long α -syn fibrils in the cytoplasm of the cells.

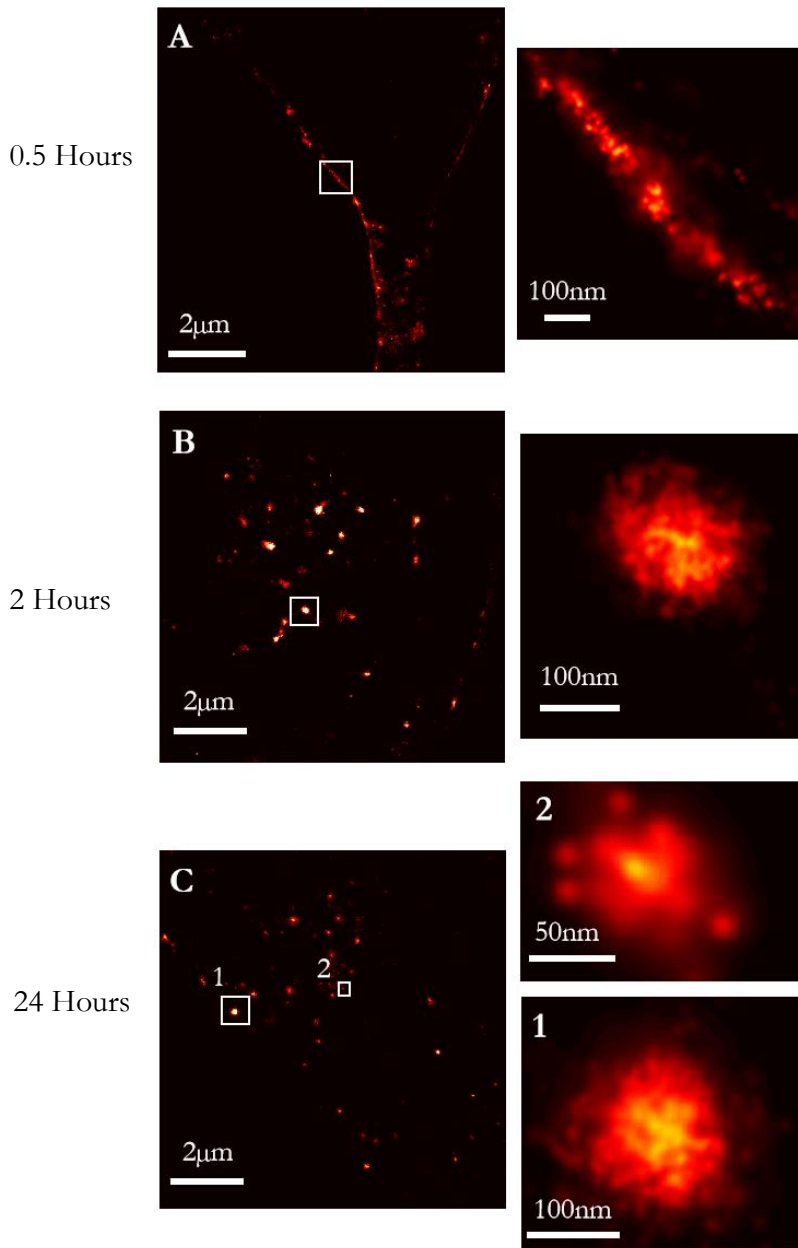


Figure 5: Super-resolution images of internalized α -syn aggregates in endosomal vesicles in time. a) dSTORM image of a cell treated for half an hour with α -syn-Alexa532 aggregates. A detailed view of the aggregates in the cell membrane is shown in the image to the right. (b) After 2 hours of incubation, α -syn aggregates are internalized in vesicles. Detailed view of the aggregates in a vesicle shown in the image to the right b). (c) Internalized α -syn aggregates after 24 hours of incubation, with two different sized clusters shown to the right.

4.3 Results and discussion

To address these questions, we used the super-resolution capability of dSTORM to probe directly the morphology of α -syn aggregates while entering SH-SY5Y cells (Fig.5). The dSTORM images, like the confocal images in figure 4, showed that α -syn aggregates initially associated with, and accumulated at the plasma membrane (Fig.5a). In the course of time cells took up the fibrils and accumulated them in endocytic vesicles (Fig.5b&c). Inside the vesicles the aggregates appeared tightly packed forming bigger clusters. The typical size of those intracellular globular structures stretched from 30 - 150 nm. It is worth mentioning that the small-sized fibrils did not completely lose their morphology even after 72 hours (Fig.5b&c). Endosomes and lysosomes are typically 50–400 nm in diameter and are distributed uniformly throughout the cytosol[28]. Hence, the size of the clusters, as determined by live-cell dSTORM, falls into the small size region expected for endosomes and lysosomes.

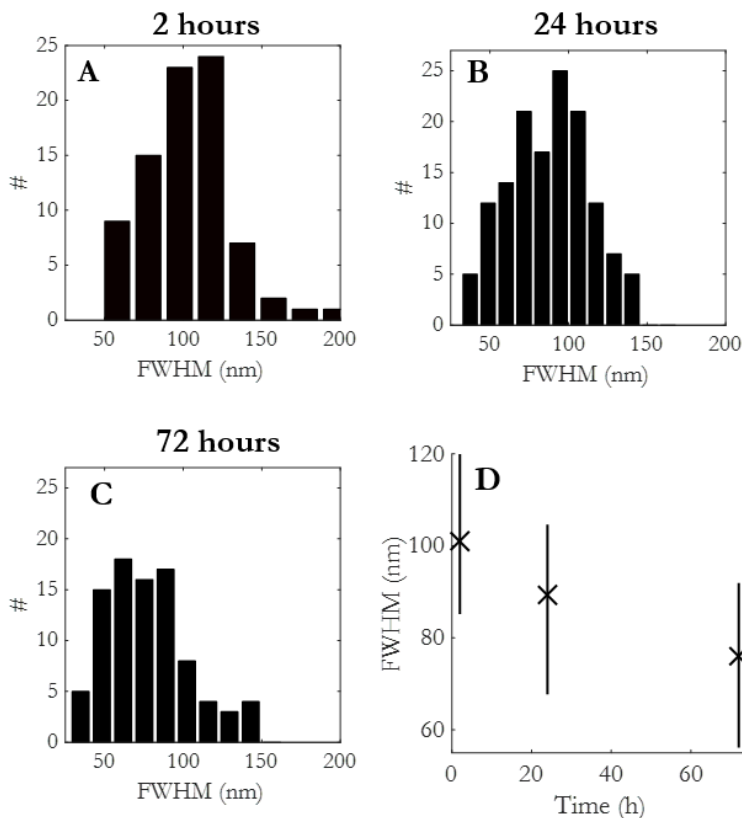


Figure 6: Size distribution of α -syn aggregates in endosomal vesicles in time. (a)-(c) Histogram distribution of intracellular α -syn clusters FWHM in time. (d) A clear decrease in α -syn cluster size is observed in the representation of the mean average FWHM of α -syn clusters in time (x = median - = 50% interval).

The size of the clusters appeared to decrease as proteins moved through the endosomal pathway towards lysosomes (Fig.6). The size decreased from 104 ± 32 nm at 2 h after incubation to 78 ± 28 nm after 72 h. This significant decrease might be interpreted as onset of lysosomal breakdown. It should be stressed that we did not observe maturation and formation of α -syn fibrils in the cytoplasm over a period of 3 days. This is a clear difference from our (see Fig.2) and others *in vitro* results in which long ($> 1 \mu\text{m}$) fibrils were already formed within this time span. It is important to note that, with the exception of Lewy bodies[9,29] there is so-far no clear evidence for the presence of linear α -syn amyloid fibrils within mammalian cells. Hence, our data further refutes the model in which fibril maturation proceeds within the cells and finally will lead to disease in Parkinson's.

In conclusion, our study provides additional evidence in favor of a lysosomal degradation pathway for removal of extracellular α -syn aggregates. Cells internalize extracellular small sized fibrils ($<1 \mu\text{m}$ length). Subsequently the aggregates accumulate in endocytic vesicles and are trafficked towards lysosomes. Fibrils keep their morphology and do not further mature but rather partially degrade as they move through endosomal pathway. As lysosomal malfunction has been linked to neurodegeneration and age-related neurodegenerative disorders[30,31], enhancing lysosomal function may be a potential therapeutic strategy for prevention or treatment of PD. Since our study did not focus on the effect of longer ($>1 \mu\text{m}$) fibers on cellular processes and cell viability, their potential impact of long fibers in disease should not be overlooked.

Acknowledgments

We thank Dr. Mireille M. A. E. Claessens at University of Twente for kindly providing a human neuroblastoma cell line, SH-SY5Y and Nathalie Schilderink for expressing and purifying human wild type α -syn. This work is part of the research program 'Single Molecule Point of View in Aggregation' of the Foundation for Fundamental Research on Matter (FOM), which is part of the Netherlands Organization for Scientific Research (NWO).

4.4 REFERENCES

- [1] M. G. Spillantini, M. L. Schmidt, V. M. Lee, J. Q. Trojanowski, R. Jakes, and M. Goedert, *Nature* 388, 839 (1997).
- [2] R. Borghi, R. Marchese, A. Negro, L. Marinelli, G. Forloni, D. Zaccheo, G. Abbruzzese, and M. Tabaton, *Neurosci. Lett.* 287, 65 (2000).
- [3] I. Devic, H. Hwang, J. S. Edgar, K. Izutsu, R. Presland, C. Pan, D. R. Goodlett, Y. Wang, J. Armaly, V. Tumas, C. P. Zabetian, J. B. Leverenz, M. Shi, and J. Zhang, *Brain* 134, e178 (2011).
- [4] O. M. El-Agnaf, S. A. Salem, K. E. Paleologou, M. D. Curran, M. J. Gibson, J. A. Court, M. G. Schlossmacher, and D. Allsop, *FASEB J.* 20, 419 (2006).
- [5] D. Freeman, R. Cedillos, S. Choyke, Z. Lukic, K. McGuire, S. Marvin, A. M. Burrage, S. Sudholt, A. Rana, C. O'Connor, C. M. Wiethoff, and E. M. Campbell, *PLoS ONE* 8, e62143 (2013).
- [6] H.-J. J. Lee, F. Khoshaghideh, S. Patel, and S.-J. J. Lee, *J. Neurosci.* 24, 1888 (2004).
- [7] H.-J. J. Lee, J.-E. E. Suk, E.-J. J. Bae, J.-H. H. Lee, S. R. Paik, and S.-J. J. Lee, *Int. J. Biochem. Cell Biol.* 40, 1835 (2008).
- [8] J. Y. Sung, J. Kim, S. R. Paik, J. H. Park, Y. S. Ahn, and K. C. Chung, *J. Biol. Chem.* 276, 27441 (2001).
- [9] L. A. Volpicelli-Daley, K. C. Luk, T. P. Patel, S. A. Tanik, D. M. Riddle, A. Stieber, D. F. Meaney, J. Q. Trojanowski, and V. M. Lee, *Neuron* 72, 57 (2011).
- [10] K. M. Danzer, S. K. Krebs, M. Wolff, G. Birk, and B. Hengerer, *J. Neurochem.* 111, 192 (2009).
- [11] K. C. Luk, C. Song, P. O'Brien, A. Stieber, J. R. Branch, K. R. Brunden, J. Q. Trojanowski, and V. M. Lee, *Proc. Natl. Acad. Sci. U.S.A.* 106, 20051 (2009).
- [12] L. A. Volpicelli-Daley, K. C. Luk, and V. M. Lee, *Nat Protoc* 9, 2135 (2014).
- [13] P. Desplats, H.-J. J. Lee, E.-J. J. Bae, C. Patrick, E. Rockenstein, L. Crews, B. Spencer, E. Masliah, and S.-J. J. Lee, *Proc. Natl. Acad. Sci. U.S.A.* 106, 13010 (2009).
- [14] C. Hansen, E. Angot, A.-L. L. Bergström, J. A. Steiner, L. Pieri, G. Paul, T. F. Outeiro, R. Melki, P. Kallunki, K. Fog, J.-Y. Y. Li, and P. Brundin, *J. Clin. Invest.* 121, 715 (2011).
- [15] W. C. Duim, B. Chen, J. Frydman, and W. E. Moerner, *Chemphyschem* 12, 2387 (2011).
- [16] D. Pinotsi, A. K. Buell, C. Galvagnion, C. M. Dobson, G. S. Kaminski Schierle, and C. F. Kaminski, *Nano Lett.* 14, 339 (2014).
- [17] J. Ries, V. Udayar, A. Soragni, S. Hornemann, K. P. Nilsson, R. Riek, C. Hock, H. Ewers, A. A. Aguzzi, and L. Rajendran, *ACS Chem Neurosci* 4, 1057 (2013).
- [18] E. K. Esbjörner, F. Chan, E. Rees, M. Erdelyi, L. M. Luheshi, C. W. Bertocini, C. F. Kaminski, C. M. Dobson, and G. S. Kaminski Schierle, *Chem. Biol.* 21, 732 (2014).

- [19] G. S. Kaminski Schierle, S. van de Linde, M. Erdelyi, E. K. Esbjörner, T. Klein, E. Rees, C. W. Bertocini, C. M. Dobson, M. Sauer, and C. F. Kaminski, *J. Am. Chem. Soc.* 133, 12902 (2011).
- [20] M. J. Roberti, J. Fölling, M. S. Celej, M. Bossi, T. M. Jovin, and E. A. Jares-Erijman, *Biophys. J.* 102, 1598 (2012).
- [21] A. Sidhu, I. Segers-Nolten, and V. Subramaniam, *Biochim. Biophys. Acta* 1844, 2127 (2014).
- [22] M. Heilemann, S. van de Linde, A. Mukherjee, and M. Sauer, *Angew. Chem. Int. Ed. Engl.* 48, 6903 (2009).
- [23] T. Schmidt, G. J. Schütz, W. Baumgartner, H. J. Gruber, and H. Schindler, *Proc. Natl. Acad. Sci. U.S.A.* 93, 2926 (1996).
- [24] S. J. Sahl, L. E. Weiss, W. C. Duim, J. Frydman, and W. E. Moerner, *Sci Rep* 2, 895 (2012).
- [25] C. Bustamante and D. Keller, *Phys. Today* 48, 32 (1995).
- [26] M. E. Fuentes-Perez, M. S. Dillingham, and F. Moreno-Herrero, *Methods* 60, 113 (2013).
- [27] V. N. Uversky and D. Eliezer, *Curr. Protein Pept. Sci.* 10, 483 (2009).
- [28] R. A. Nixon and A. M. Cataldo, *Trends Neurosci.* 18, 489 (1995).
- [29] R. A. Crowther, S. E. Daniel, and M. Goedert, *Neurosci. Lett.* 292, 128 (2000).
- [30] B. A. Bahr and J. Bendiske, *J. Neurochem.* 83, 481 (2002).
- [31] R. A. Nixon, A. M. Cataldo, and P. M. Mathews, *Neurochem. Res.* 25, 1161 (2000).

4.5 SUPPLEMENTARY FIGURES

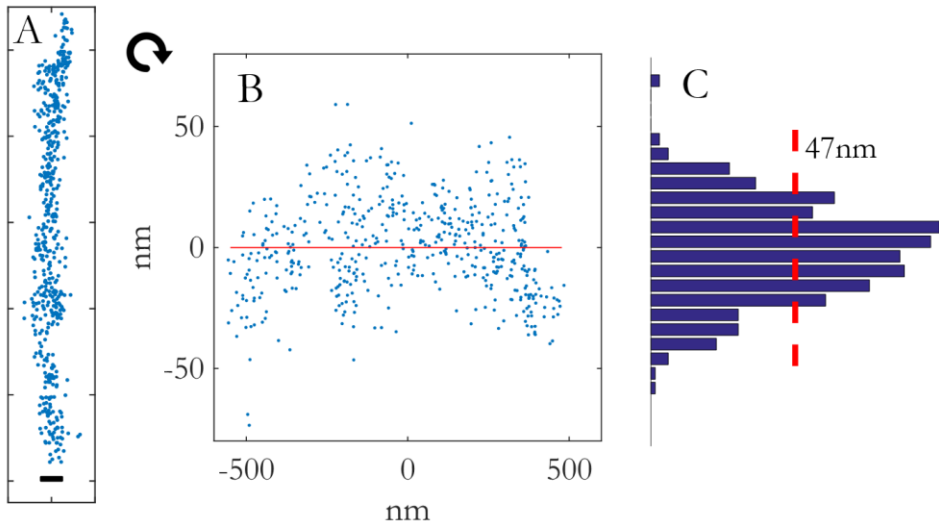


Figure S1: FWHM determination. (a) The 526 localizations of the single fibril from figure 3a. Scale bar = 50nm (b) Locations are rotated so the angle of a linear fit is 0 (red line). (c) Y-coordinates are binned into \sqrt{N} bins. FWHM is determined from linear interpolation of the histogram to be 47nm. (red dashed line)

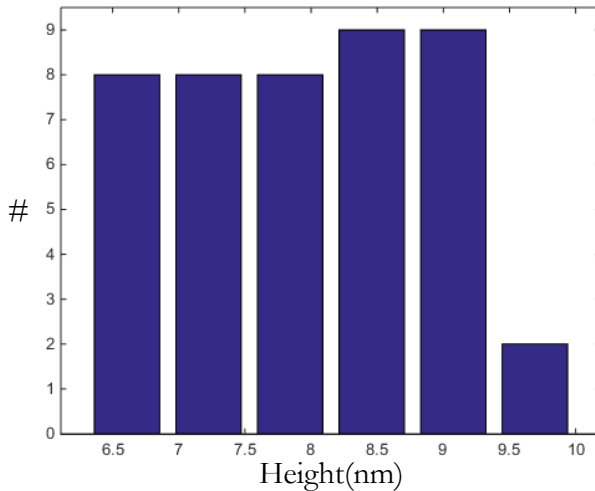


Figure S2: Height distribution of fibrils obtained by AFM.

CHAPTER 5

FORCE SENSING AND QUANTITATIVE DSTORM ON SIGNAL TRANSDUCTION PROTEINS¹

Quantitation in stochastic optical reconstruction microscopy is challenged by variations in the labeling strategies and the complex photophysics of the fluorescence labels. Both contribute to multiple observations of the same molecule, which can lead to imaging artifacts and prevents an easy assignment of a local stoichiometry. Here we developed a method that uses the inherent high spatial accuracy in super-resolution microscopy to determine the local stoichiometry. The methodology is based on analysis of the spatial distance distribution in the images which in turn is used to distinguish between spatially correlated and uncorrelated localizations. Given that fluorescence labeling and photophysics is equivalent for both the spatially correlated and uncorrelated localizations the exact stoichiometry can be determined even without detailed knowledge about the statistics governing the labeling strategy. Simulations show that our method can accurately reproduce the local stoichiometry even at high protein density. The strength of the methodology is demonstrated by addressing the stoichiometry of the protein vinculin in focal adhesion complexes, the dense structures at which cells mechanically interact with the extracellular matrix. When combined with high resolution force measurements we found that the local force developed by a focal adhesion increases on average by 15pN for each vinculin molecule localized to the focal adhesion.

¹This chapter is based on: R. Harkes, H.E. Balcioglu, E.H.J. Danen and T.Schmidt, Force sensing and quantitative dstorm on signal transduction proteins inside the integrin adhesome.

5.1 INTRODUCTION

Quantitative description of processes in biology belongs to the current great challenges in the life sciences. Ultimately one would like to know the composition of all cellular components in space and time and describe their respective interactions. Although such undertaking in general terms appears unreachable, with the developments of single molecule techniques in the 1990's [1,2] it became possible to follow individual molecules in real time at high spatial and temporal resolution [3,4], assess their local stoichiometry [5], and follow their actions [6].

With the further developments of single molecule techniques towards super-resolution imaging in 2006 [7–9] the initial aim came even closer into reach. In particular, super-resolution techniques that utilize single molecule imaging such as photo activation localization microscopy (PALM [8], fPALM [9]) and (direct) stochastic optical reconstruction microscopy (STORM [7], dSTORM [10]) have developed into standard tools in biophysics and cell biology. Those methods produce massive data that contain structural and compositional information [6]. So far mostly the high spatial resolution of the techniques has been utilized. Super-resolution imaging yielded spectacular images of cells leading to new insights into the structure and function of many subcellular components [11].

Since stochastic imaging is based on the observation of individual molecules, it appears tempting to use the technique in the context of quantifying a 'digital stoichiometry' by just counting the number of molecules in a given structure. This approach would complement earlier methods in single molecule microscopy where photon correlation [12], the digital signal level [13,14] and digital photobleaching [15,16] have been used to address the oligomeric state of a protein complex [13,16,17]. However, unlike single molecule microscopy where the concentration of structures is low (or is experimentally adjusted [13]), in super-resolution microscopy the density of molecules is inherently very high with significant spatial overlap of signals. Additionally, photo-unstable molecules are essential for super-resolution imaging to induce the stochastic blinking of the fluorescence labels needed. This inherently results in multiple detections of individual fluorophores within an acquisition cycle.

A second factor that hinders quantitative analysis is the use of antibody labeling in STORM techniques. Typically the protein of interest is first labeled by a primary antibody, that in turn is labeled by multiple (2-4) secondary antibodies, each carrying multiple (~4) fluorophores [18]. Hence, a single protein of interest

is labeled by ~ 10 fluorophores each switched on and off in a stochastic manner. Therefore the number of detections of one protein is typically not equal to the number of proteins in the sample. Quantitative super-resolution microscopy must account for those multi-detections to yield reliable information about the true local stoichiometry in the sample.

An early method to prevent multiple detection of the same fluorophore is a cleaning algorithm that deletes any further detection within a radius Δr for a time span Δt . The choice of the parameters Δr and Δt depends on the photophysical properties of the fluorophore and the characteristics of the setup. Typically Δr is set to the positional accuracy for single molecule detection ($\Delta r = 5\text{-}50\text{ nm}$), and Δt set to a timescale that safely exceeds the photobleaching time of the fluorophores ($\Delta t = 1\text{-}10\text{ s}$). This method is well accepted for PALM imaging where undercounting inherent to the method is acceptable. The method works since, in PALM, each protein of interest is labeled with exactly one fluorescent protein, that bleaches fast and has dark times of about 50 ms [19].

For STORM and dSTORM experiments, that have multiple fluorescent dye molecules per protein of interest, suitable parameters for Δr and Δt are less obvious. Because of this, in STORM data quantitative analysis is often performed using density-based clustering algorithms [20–23]. Here localizations are categorized based on their local density as members of clusters. However, when the underlying structure is densely labeled, this method will not accurately separate individual molecules, and instead be sensitive to local clustering of the protein. Therefore this method is useful primarily for spatial cluster analysis [24,25], and not for counting of molecules.

A technique to quantitatively analyze protein distributions is PC-PALM [26,27]. The method was developed for PALM imaging, but likewise applicable to other stochastic super-resolution techniques. In PC-PALM a pixelated digital image is generated as a starting point for the calculation of a pair correlation function, $g(r)$. The pair correlation function describes how the probability to find a second localization evolves with distance r . Pixelation has to be fine enough to create a true binary image, i.e. each pixel is occupied by either 0 or 1 localization. Hence, the method pretends an accuracy where each localization is centered on a pixel and determined with an accuracy of about half the size of the pixel. This approach will induce ambiguities in $g(r)$ depending on the chosen pixelsize. For dense samples it will result in extremely large images since the pixels must be very small. Therefore the method uses selective regions with a high number of

5.1 Introduction

occupied pixels to determine $g(r)$. This ignores information that might be contained in the less dense regions of the sample.

In what follows we describe a methodology that allowed us to count molecules and determine local densities from stochastic super-resolution data. Analogous to PC-PALM the methodology is based on the high positional accuracy that is a characteristic of super-resolution imaging. The cumulative density function of mutual distances is used to obtain the number of correlated and uncorrelated localizations in a field of view. Given that both depend equally on the underlying photophysical and labeling statistics, both are corrected for using this technique and the number of molecules is derived with minimal assumptions. Our method is an easy real space method, that has similarities to the Fourier ring-correlation analysis developed earlier [28].

Subsequently the strength of the methodology is demonstrated in addressing the stoichiometry of proteins in focal adhesion complexes. Focal adhesions, FAs, are membrane-proximal structures where the mechanical coupling of the cellular cytoskeleton with the extracellular matrix occurs and where mechanical signals are passed from the outside world to the cell's interior and *vice versa*. In what way mechanical signals are translated to a biochemical outcome is not yet well understood. Among the missing information that is required to develop a quantitative model of mechano-reception is a detailed knowledge about the stoichiometry of the proteins localized in FAs. Together with information about the local stress and force fields the stoichiometry permits to create a 'sensitivity map', a measure of how much a particular protein contributes to force sensitivity of the cell.

Recently we developed technology that allowed us to simultaneously measure cellular forces at 500 pN sensitivity together with dSTORM at a resolution of 30 nm to reveal the nanoscale architecture of focal adhesions [29]. In the current report we use this technology to quantitatively investigate the correlation of number of vinculin molecules in a FA in relation to the cellular force generated locally. We found that our method reliably reconstructs the number of molecules even in a dense image. When combined with force measurements we find that each vinculin molecule added, increases the force in a FA by 15pN on average.

5.2 MATERIALS AND METHODS

5.2.1 Cell culture

NIH-3T3 fibroblasts were cultured in medium (DMEM; Dulbecco's modified Eagle's Medium, Invitrogen/Fisher Scientific) supplemented with 10% new born calf serum, 25 U/ml penicillin and 25 $\mu\text{g}/\text{ml}$ streptomycin (Invitrogen/Fisher Scientific cat. # 15070-063).

5.2.2 Sample preparation

Micropillar preparation and cell seeding;

Micropillars were used for cellular traction force measurements according to methodology described previously [29]. A negative silicon master was made using a two-step Deep Reactive Ion Etching (DRIE) process. Two different etching depths were obtained by subsequently applying two masks to the same wafer. A mask with 10x10 mm arrays with circles of 2 μm diameter and 4 μm center-to-center distance in a hexagonal grid was used as a negative for the micropillar arrays. A mask with two rectangular spacers of 10x2 mm was aligned on the sides of the arrays. The etching depth was varied for the micropillar arrays to make pillars of height 6.9 μm . After passivation of the negative silicon master with trichloro silane (Sigma Aldrich), well-mixed PDMS at 1:10 ratio (crosslinker:prepolymer) was poured over the wafer. After 20 hours at 110°C, the PDMS was fully cured. Under these conditions bulk PDMS has a Young's modulus of 2.5 MPa as determined by tensile testing. The pillar array used in the current study has a bending stiffness of 16 nN/ μm as determined by finite element analysis [29]. This can be related to the bending stiffness of a circular area the size of the top of a pillar of a material with a Young's modulus of 11.6 kPa [30]. The effective Young's modulus of the pillar array, E_{eff} , is therefore 11.6 kPa. The individual micropillar arrays were peeled off with two spacers on the sides. Fibronectin stamping was performed using a flat piece of PDMS (1:30 ratio, cured 16 hours at 65°C). Per stamp, a 40 μl mix of 50 $\mu\text{g}/\text{mL}$ unlabeled fibronectin (Sigma Aldrich) and 10 $\mu\text{g}/\text{mL}$ Alexa405 (Invitrogen)-conjugated fibronectin was used. After stamping, the micropillars were blocked with 0.2% Pluronic (F-127, Sigma Aldrich) in PBS for 1 hour at room temperature and washed with PBS. Cells were seeded in single cell density in complete medium and incubated for 5 hours at 37 °C and 5% CO₂.

5.2 Materials and methods

Fixation and immunostaining:

Samples were washed once with cytoskeletal buffer (CB; [31]), subsequently permeabilized and fixated for 10 seconds with 0.1-0.25% Triton-X, 0.4% paraformaldehyde and 1 μ g/mL phalloidin in CB. The triton concentration was adjusted to minimize the background signal without reducing the force application. Samples were finally fixed with 4% formaldehyde in CB, permeabilized with 0.1% Triton-X and blocked with 0.5% BSA in PBS. Immunostaining was performed with a primary mouse antibody against vinculin (Sigma, V-9131), and an Alexa 647 conjugated secondary antibody against mouse IgG (Jackson, 115-605-006) following the protocol suggested by [32].

5.2.3 dSTORM

Super-resolution imaging was performed on a home-built wide-field single molecule setup, based on an Axiovert S100 (Zeiss) inverted microscope equipped with a 100x 1.4NA oil-immersion objective (Zeiss, Germany). Micropillar arrays were inverted onto #0, 25 mm diameter, round coverslips (Menzel Glaser). The micropillar arrays were kept from floating using a support weight made of glass. Imaging was performed in 100 mM mercaptoethylamine (MEA, Sigma Aldrich) in PBS. A 405 nm laser (CrystaLaser, USA) was used for imaging the pillars and photoswitching of the Alexa 647 dye to adjust the density of visible fluorophores. The light was reflected into the objective by a dichroic mirror (ZT405/532/635rpc, Chroma, USA). The fluorescence light in the detection path was filtered using the emission filter ZET532/633m (Chroma, USA). Conversion intensities were between 0 and 250 W/cm² at 405 nm, and the excitation intensity was 5 kW/cm² at 647 nm. For each sample, we acquired 20000 images with an acquisition time of 10 ms per frame and a frame rate of 69 Hz. The signal of individual dye molecules was captured on a sCMOS Orca Flash 4.0V2 camera (Hamamatsu, Japan). The average integrated signal of a single dye molecule was 608 detected photons, spatially distributed by the 2 dimensional point-spread-function of the microscope of 440 nm FWHM.

The signal from individual fluorophores was fitted with a 2-dimensional Gaussian using a custom least-squares algorithm in Matlab [3]. From the fit we determined the location of each molecule to an accuracy of 16 nm on average (Fig.5b). The localization accuracy for an individual fluorophore coincides with the value predicted from the width of the point-spread-function and the detected signal, $440 \text{ nm} / \sqrt{[608]} = 18 \text{ nm}$.

5.2.4 Image analysis

Pillar deflections were determined with approximately 53 nm precision using a specifically designed Matlab script [29]. The pillar locations were determined from the labeled fibronectin fluorescence image using a fit to the cross-correlation function between a perfect binary circle and the local fluorescence of one pillar. Those positions were compared to those of a perfect hexagonal grid used as reference. For an undeflected array the accuracy was found to be 53 nm, this corresponds to a force accuracy of 860 pN on the pillar array of $E_{\text{eff}} = 11.6$ kPa. Masks for adhesions corresponding to individual pillars of interest were manually drawn for each case.

5.3 RESULTS

5.3.1 Analysis framework

The majority of methods that have been developed so far to extract the number of molecules from super-resolution microscopy images focused on the temporal characterization of the blinking and bleaching behavior of the fluorescent molecules [19,33,34]. Here we take a different approach and use the spatial information of imaging methods to obtain a robust estimator for local densities. By such analysis the high spatial resolution, inherent to super-resolution techniques, are most efficiently utilized. The method uses features of particle image correlation spectroscopy (PICS) from single molecule imaging [35] for the determination of spatial correlations, and of number-and-brightness (N&B) analysis in confocal microscopy [36] that accounts for labeling and photophysics of the fluorophores.

Basis of the images in super-resolution imaging are the positions of all localizations including their respective accuracies, $r_i \pm \Delta r_i$. Typically, $N = 10^4$ - 10^6 localizations are used to generate a final super-resolution image. From the position data the two-point spatial correlation function $g(r)$ and subsequently the cumulative distance function, cdf, is calculated that contains spatial information of the image,

$$cdf(r) = \int_0^r g(r') dr'. \quad (1)$$

For discrete 2D position data $r_i = \{x_i, y_i\}$, as obtained in super-resolution microscopy, the cdf is constructed from

$$cdf(r) = 2 \sum_{i=1}^N \sum_{j=i+1}^N (x_i - x_j)^2 + (y_i - y_j)^2 < r^2. \quad (2)$$

The cdf describes the number of mutual distances in a sample of N localizations that are smaller than r .

When a protein is detected multiple times in the image stack, the number of localizations, N , exceeds the number of independent emitters, M . Multi-localizations of individual molecules are correlated in space on short distances.

The correlation length, σ_i , is given by a combination of the localization uncertainty for an individual fluorophore, Δr_i , and the size of a primary and secondary antibody complex that might have been used to label the protein of interest. Typically, both are in the range of 10 nm. Since both detection and labeling originate from statistical processes, we assume that they are Gaussian distributed in space leading to a cdf that reads,

$$cdf(r) = N_c \left(1 - e^{-\frac{r^2}{4\sigma^2}} \right). \quad (3)$$

Here N_c is the total number of correlated distances and σ the mean positional uncertainty for all localizations. In particle image correlation spectroscopy an identical description was found that permits to determine lateral mobility of molecules characterized by their mean squared displacement [35].

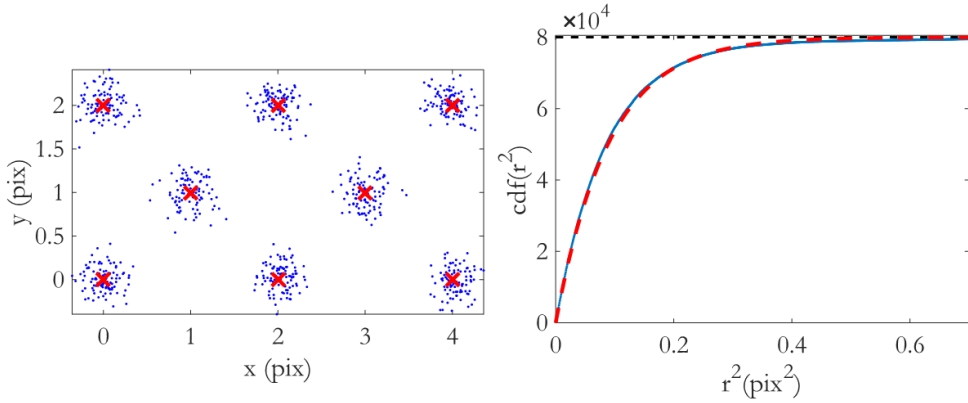


Figure 1: Distance distribution of Gaussian distributed localizations

A) 8×100 Gaussian distributed localizations. $N=8$, $R=100$, $\sigma=0.15$.

B) Cumulative squared distance distribution (CSDD) for A (blue). Asymptote at $N \times (R^2 - R)$ (black dashed line). The distributions follows $1 - \exp(-r^2/4\sigma^2)$ (red dashed line).

The effect of spatial correlation on the cdf is exemplified in the simulation shown in figure 1. Eight emitters were placed into the field of view, each allowed to reappear at random for $n_i = 100$ times at a spatial accuracy of $\sigma = 0.15$. The resulting cdf (Fig.1 right) exactly follows the functional form predicted in eq. (3) on short length scales.

5.3 Results

On length scales longer than the correlation length the cdf is characterized by a distance distribution for uncorrelated molecules. Assuming a homogeneous, random organization of molecules within a given field-of-view of area, A , the cdf of uncorrelated localizations scales quadratically with distance as:

$$cdf(r) = N_u \frac{\pi r^2}{A}. \quad (4)$$

Thus, the general form for the spatial correlation function is a linear combination of the correlated and the uncorrelated part:

$$cdf(r) = N_c \left(1 - e^{-\frac{r^2}{4\sigma^2}} \right) + N_u \frac{\pi r^2}{A} \quad (5)$$

The predicted dependence of cdf on distance (eq. (5)) is seen for a simulation in figure 2. The cdf resembles those reported in studies of protein mobility [35,37,38].

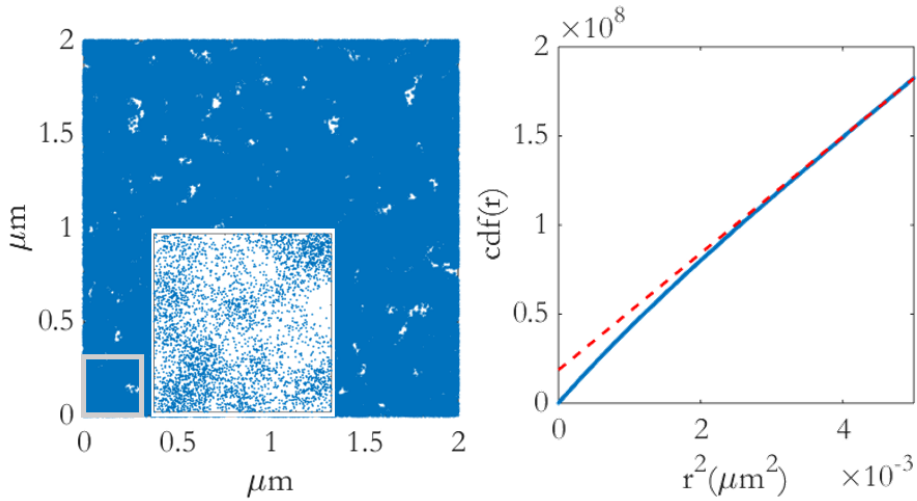


Figure 2: 2048 molecules (blue dots) placed randomly in a $2 \times 2 \mu m^2$ box.

A) Image obtained for a positional accuracy of $\sigma = 20 nm$ and recurrence of the signal of $m_i = 100$. At this density the images of individual molecules overlap completely, see the zoom-in to the gray square.

B) Cumulative distance distribution (CDD). From linear extrapolation to the intersection with the y-axis the number of correlated distances is equal to $N_c = 2 \times 10^7$.

In the simulation 2048 individual molecules were randomly positioned in a box of $2 \times 2 \mu\text{m}^2$ and each molecule was allowed to reappear 100 times. The positional accuracy was set to 20 nm. The resulting distance distribution was calculated. Its dependence on the squared distance, r^2 , is shown in figure 2 (right). For squared distances beyond $4 \times 10^{-3} \mu\text{m}^2$ the $\text{cdf}(r^2)$ became linear as predicted from eqs. (4)&(5). The slope of the linear part equals $\pi N_u/A$. Its intersection with the y-axis equals N_c , the number of correlated distances (see eqs. (4) and (5)). Hence, using the spatial information that is contained in super-resolution images, the number of correlated and uncorrelated distances are obtained.

From those, the number of molecules can be calculated even without any detailed knowledge about labeling statistics and photophysics as shown in the following. The number of localizations, N , originating from M molecules each being observed n_i times is given by

$$N = \sum_{i=1}^M n_i \quad (6)$$

The total number of all mutual distances is equal to $N \times (N-1)$, and using eq. (6)

$$N(N-1) = \left(\sum_{i=1}^M n_i \right)^2 - \sum_{i=1}^M n_i \quad (7)$$

Likewise, the total number of correlated distances per molecule is given by $n_i \times (n_i-1)$, for all molecules this yields:

$$N_c = \sum_{i=1}^M (n_i^2 - n_i) \quad (8)$$

With the definition of the mean $\langle \dots \rangle$, eqs. (7) and (8) yield

$$\frac{N \cdot (N - 1) + N}{N_c + N} = \frac{M^2 \langle n \rangle^2}{M \langle n^2 \rangle} \quad (9)$$

5.3 Results

From this the number of independent molecules M can be calculated

$$M = \frac{N^2}{N_c + N} \cdot \left(1 + \frac{\text{var}(n)}{\langle n \rangle^2} \right) \quad (10)$$

In eq. (10) $\text{var}(n_i) = \langle n_i^2 \rangle - \langle n_i \rangle^2$, is the variance in the number of detections per molecule.

Eq. (10) describes how to obtain the number of molecules in a given super-resolution image from the total number of localizations, N , and the number of correlated distances, N_c . The latter is obtained from a fit to the cumulative distance distribution using eq. (5). The second term in eq. (10) summarizes the properties of the joined statistics of labeling and photophysics of the fluorophores. Its value varies between 1 and 2 depending on which of the various processes dominates the joined statistics. For a typical dSTORM experiment, as used in the remainder of this report, the protein of interest is labeled by a primary antibody. This in turn is labeled by several secondary antibodies, and the latter labeled by 4 fluorophores on average. The value in such a case is close to one (see the supplementary material for a more detailed analysis).

Figure 3 shows that our method reliably extracts the number of molecules even from very dense images. Simulations were performed for densities between 40 and 4000 independent emitters on an area of $2 \times 2 \mu\text{m}^2$. The mean positional accuracy was assumed $\sigma = 20 \text{ nm}$, the mean number of localization per molecule $\langle n \rangle = 100$. At high densities there was significant overlap of molecules within the image (Fig.2). The number of estimated molecules faithfully followed the input within an accuracy of 10%

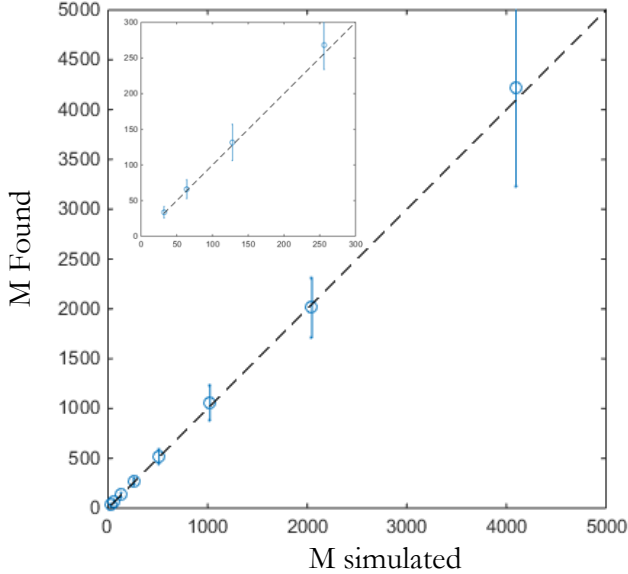


Figure 3: Determination of the number of molecules in simulated results of different densities using formula 7. Figure 2 shows the procedure for $N=2048$. Insert is a zoom-in for small N . This shows the method is accurate for a large range of densities.

In the estimation of the number of correlated distances from eq. (3) it was assumed that all molecules were randomly organized. This restriction is readily lifted by the addition of a second exponential term of size, N_L , that accounts for a length scale, L , that characterizes any spatial structures in real data.

$$cdf(r) = N_c \left(1 - e^{-\frac{r^2}{4\sigma^2}} \right) + N_L \left(1 - e^{-\frac{r^2}{L^2}} \right). \quad (11)$$

For the distinction of the two components, the typical structural length scale should be significantly larger than the positional accuracy, $L > 4\sigma$, typically 40 nm for a positional accuracy of 10 nm. This length scale is smaller than many cellular structures, like large membrane compartments, adhesion clusters, chromosome territories, such that the method described above provides a very general solution for molecule counting in super-resolution microscopy.

5.3.2 Counting molecules in focal adhesions

The strength of the method developed above is demonstrated for the analysis of the stoichiometry in focal adhesions, FAs. A typical image taken on a confocal microscope is shown in figure 4. Focal adhesion molecules (red) were localized in elongated structures. FAs emerged from out the top of pillars (blue, see also zoom in in figure 4). In the following we focused on the FA-protein vinculin. Vinculin is an adapter protein linking other integrin proximal proteins to the actin cytoskeleton. Talin, one such integrin proximal protein, has cryptic vinculin binding sites that unfold under force [39] and has been shown to be important for force-induced adhesion strengthening [39]. Vinculin is recruited to FAs in a force dependent manner [40] and mediates focal adhesion growth through binding to talin and f-actin [41]. By correlation of the number of vinculin molecules in a given FA with the local force that a cell exerts, one would be able to narrow down the force range the prospective vinculin force-sensor/responder would have.

Mouse NIH-3T3 fibroblasts were seeded on an elastic micropillar array of effective Young's modulus, $E_{\text{eff}} = 11.6$ kPa and allowed to spread for 5 h. The pillar-tops were stamped with fluorescence-labeled fibronectin. Unspecific cell adhesion was blocked to study integrin fibronectin interaction. Subsequently, cells were fixed, stained for vinculin and imaged.

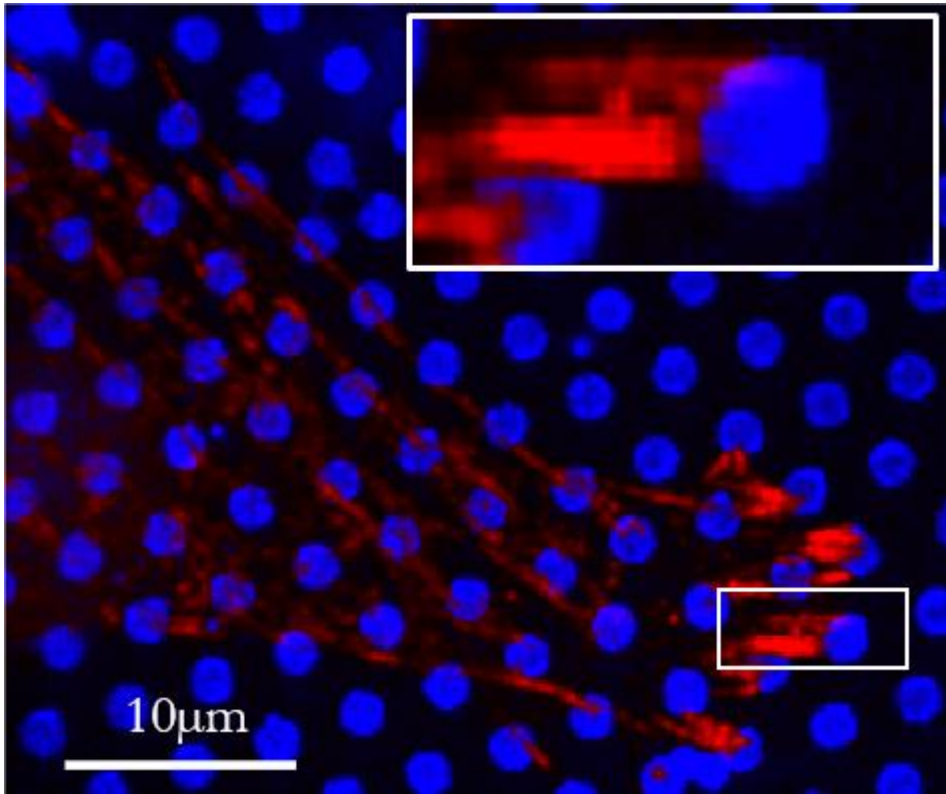


Figure 4: Confocal image of a 3T3 mouse fibroblast on Alexa405-labeled fibronectin coated micropillars. Talin, a FA protein, is immunostained with Alexa647. Zoom in shows a focal adhesion attached to a micropillar.

Super-resolution images were obtained using direct stochastic optical microscopy (dSTORM). Fixed cells were placed into dSTORM switching buffer and imaged on a high-sensitivity microscope where the fluorescence of labeled vinculin was acquired.

A super-resolution image of the organization of vinculin in a FA is shown in figure 5a. The image of size $1 \times 4 \mu\text{m}$ consists of 3616 localizations. Clearly 2 FAs emerged from a single pillar (dashed circle) in this image. FAs were elongated structures of several μm in length and had a width of 70-100 nm.

5.3 Results

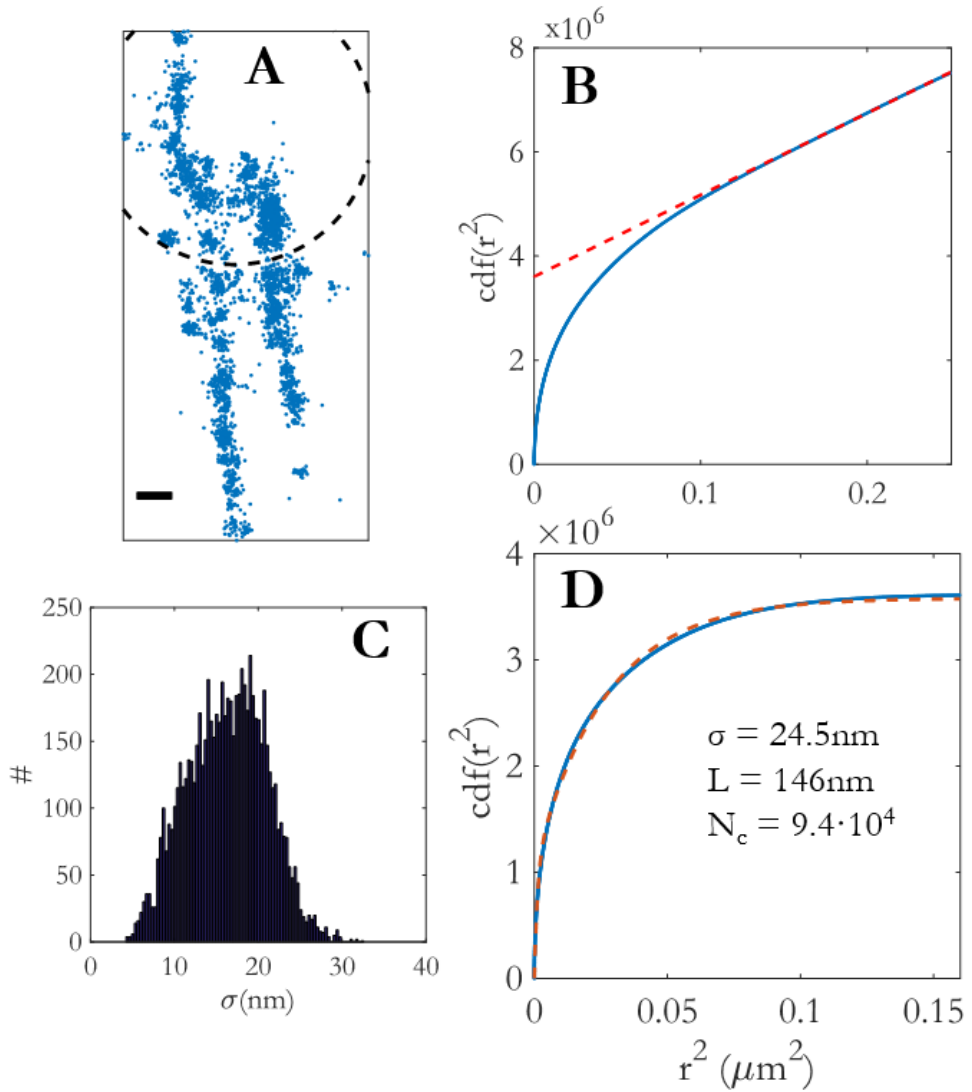


Figure 5: Analysis of a single focal adhesion.

A) 3616 localizations of Alexa647 bound to Vinculin. The dashed circle represents the position of the pillar. Scale bar = 250nm.

B) Cumulative distance function (cdf) of the localizations. From $0.09 \mu\text{m}^2$ to $0.25 \mu\text{m}^2$ the increase is linear, indicating uncorrelated distances that scale with the density.

C) Histogram of the positional accuracy of the localizations in A. Mean value is 16 nm.

D) Cdf from figure 5b with subtracted linear part. In red the double exponential fit of formula 11. The first exponential, consisting of $N_c = 9.4 \times 10^4$ distances, has a sigma close to the positional accuracy. The second exponential can be explained by the structure of the focal adhesion itself. The total number of molecules in figure 5a equals $3616^2 / (3616 + 9.4 \times 10^4) = 134$.

From the position data the cumulative distribution function (cdf) of mutual distances was calculated for squared distances between 0 and $0.3 \mu\text{m}^2$ (Fig. 3b). As predicted from eq. (5) the cdf becomes linear for squared distances beyond $0.1 \mu\text{m}^2$, characteristic for uncorrelated localizations. Extrapolation of the linear part to $0 \mu\text{m}^2$ yields the number of localizations that is correlated due to either multiple localizations or to the FA structure, $N_c + N_L = 5.2 \pm 0.1 \times 10^5$.

Figure 5d shows the cdf up to $0.1 \mu\text{m}^2$. The data were fit to a dual-correlation model (eq. 11), given that a typical length scale reflecting the widths of the focal adhesions was predicted to occur from the image (Fig. 5a). This fit yielded two length scales, one of 24.5 nm predicted for the positional accuracy of 16 nm and the antibody size of 18 nm, and a length scale of $L = 146 \text{ nm}$ set by the widths of the FAs seen in figure 5a. The number of correlated localizations was $N_c = 9.4 \pm 0.1 \times 10^4$. Further assuming that the second term in equation 10 accounting for the photophysics and labeling statistics is close to unity (see supplemental information) the number of vinculin molecules that are distinguished in figure 5a is $M = 3616^2 / (9.4 \times 10^4 + 3616) = 134 \pm 1$.

5.4 DISCUSSION

The use of high accuracy position data that is inherent to super-resolution imaging allowed us to extract the number of molecules in an image in a robust manner. When applied to fixed-cell data for the localization of the protein vinculin we were able to determine the number of vinculin molecules in the highly dense structure of focal adhesions, structures that allow cells to interact mechanically with their environment.

Simultaneously to the localizations of individual vinculin molecules we measured the local force of the cell as reflected by a displacement of the elastomeric pillar from its un-deflected position (data not shown [Harkes&Balcioglu, in preparation]). The pillar that the FA attaches to in figure 5a (indicated by the dotted circle) was deflected by 123 ± 53 nm, equivalent to a force of 2 ± 0.9 nN. Assuming all molecules contributed equally to the buildup of this force we conclude that addition of each vinculin molecule to a FA results in a force increase of 2 nN / 134 vinculin = 15 ± 7 pN/vinculin. Whether this linear relationship, earlier found for bulk parameters like focal adhesion size [29,42,43], holds on a molecular scale will have to be confirmed in future experiments using the methodology developed in the current study.

5.5 OUTLOOK

This method to find the number of proteins should be independent of the antibody staining used. To verify this important property one could express a protein with two different binding epitopes. These can then be labeled with different primary and secondary antibodies. A dual color experiment should show a clear correlation between the found number of molecules. The correlation gives a measure for the difference in affinity of the primary antibody.

5.6 REFERENCES

- [1] WE Moerner and Kador, Phys. Rev. Lett. **62**, 2535 (1989).
- [2] Orrit and Bernard, Phys. Rev. Lett. **65**, 2716 (1990).
- [3] T. Schmidt, G. J. Schütz, W. Baumgartner, H. J. Gruber, and H. Schindler, Proc. Natl. Acad. Sci. U.S.A. **93**, 2926 (1996).
- [4] T. Funatsu, Y. Harada, M. Tokunaga, K. Saito, and T. Yanagida, Nature **374**, 555 (1995).
- [5] G. J. Schütz, H. Schindler, and T. Schmidt, Biophys. J. **73**, 1073 (1997).
- [6] H. P. Lu, L. Xun, and X. S. Xie, Science **282**, 1877 (1998).
- [7] M. J. Rust, M. Bates, and X. Zhuang, Nat. Methods **3**, 793 (2006).
- [8] E. Betzig, G. Patterson, R. Sougrat, O. Lindwasser, S. Olenych, J. Bonifacino, M. Davidson, J. Lippincott-Schwartz, and H. Hess, Science **313**, 1642 (2006).
- [9] ST Hess, T. Girirajan, and MD Mason, Biophysical Journal (2006).
- [10] M. Heilemann, S. van de Linde, M. Schüttpelz, R. Kasper, B. Seefeldt, A. Mukherjee, P. Tinnefeld, and M. Sauer, Angew. Chem. Int. Ed. Engl. **47**, 6172 (2008).
- [11] T. Klein, S. van de Linde, and M. Sauer, Chembiochem **13**, 1861 (2012).
- [12] L. Edman, U. Mets, and R. Rigler, Proc. Natl. Acad. Sci. U.S.A. **93**, 6710 (1996).
- [13] M Moertelmaier and M Brameshuber, Applied Physics ... (2005).
- [14] T. Schmidt, G. J. Schütz, H. J. Gruber, and H. Schindler, Analytical Chemistry **68**, 4397 (1996).
- [15] M. P. Gordon, T. Ha, and P. R. Selvin, Proc. Natl. Acad. Sci. U.S.A. **101**, 6462 (2004).
- [16] S. C. Kohout, M. H. Ulbrich, S. C. Bell, and E. Y. Isacoff, Nat. Struct. Mol. Biol. **15**, 106 (2008).
- [17] G. S. Harms, L. Cognet, P. H. Lommerse, G. A. Blab, H. Kahr, R. Gamsjäger, H. P. Spaink, N. M. Soldatov, C. Romanin, and T. Schmidt, Biophys. J. **81**, 2639 (2001).
- [18] E. A. Greenfield, *Antibodies: A Laboratory Manual (second Edition)* (Cold Spring Harbor Laboratory Press, 2012).
- [19] P. Annibale, S. Vanni, M. Scarselli, U. Rothlisberger, and A. Radenovic, PLoS ONE **6**, e22678 (2011).
- [20] A. Löschberger, C. Franke, G. Krohne, S. van de Linde, and M. Sauer, J. Cell. Sci. **127**, 4351 (2014).
- [21] D. Bar-On, S. Wolter, S. van de Linde, M. Heilemann, G. Nudelman, E. Nachliel, M. Gutman, M. Sauer, and U. Ashery, J. Biol. Chem. **287**, 27158 (2012).
- [22] S. Letschert, A. Göhler, C. Franke, N. Bertleff-Zieschang, E. Memmel, S. Doose, J. Seibel, and M. Sauer, Angew. Chem. **126**, 11101 (2014).
- [23] N. Ehmann, S. van de Linde, A. Alon, D. Ljaschenko, X. Z. Keung, T. Holm, A. Rings, A. DiAntonio, S. Hallermann, U. Ashery, M. Heckmann, M. Sauer, and R. J. Kittel, Nat Commun **5**, 4650 (2014).

5.6 References

- [24] X. Nan, E. A. Collisson, S. Lewis, J. Huang, T. M. Tamgüney, J. T. Liphardt, F. McCormick, J. W. Gray, and S. Chu, *Proc. Natl. Acad. Sci. U.S.A.* **110**, 18519 (2013).
- [25] A. Pezzarossa, F. Zosel, and T. Schmidt, *Biophys. J.* **108**, 1870 (2015).
- [26] P. Sengupta, T. Jovanovic-Talisman, D. Skoko, M. Renz, S. Veatch, and J. Lippincott-Schwartz, *Nat. Methods* **8**, 969 (2011).
- [27] S. L. Veatch, B. B. Machta, S. A. Shelby, E. N. Chiang, D. A. Holowka, and B. A. Baird, *PLoS ONE* **7**, e31457 (2012).
- [28] R. P. Nieuwenhuizen, M. Bates, A. Szyborska, K. A. Lidke, B. Rieger, and S. Stallinga, *PLoS ONE* **10**, e0127989 (2015).
- [29] H. van Hoorn, R. Harkes, E. M. Spiesz, C. Storm, D. van Noort, B. Ladoux, and T. Schmidt, *Nano Lett.* **14**, 4257 (2014).
- [30] M. Ghibaudo, A. Saez, L. Trichet, A. Xayaphoummine, J. Browaeys, P. Silberzan, A. Buguin, and B. Ladoux, *Soft Matter* (2008).
- [31] J. V. Small and A. Sechi, *Cell Biology: A Laboratory Handbook* (1998).
- [32] S. van de Linde, A. Löschberger, T. Klein, M. Heidebreder, S. Wolter, M. Heilemann, and M. Sauer, *Nat Protoc* **6**, 991 (2011).
- [33] S. van de Linde and M. Sauer, *Chem Soc Rev* **43**, 1076 (2014).
- [34] J. Vogelsang, T. Cordes, C. Forthmann, C. Steinhauer, and P. Tinnefeld, *Proc. Natl. Acad. Sci. U.S.A.* **106**, 8107 (2009).
- [35] S. Semrau and T. Schmidt, *Biophys. J.* **92**, 613 (2007).
- [36] J. R. Unruh and E. Gratton, *Biophys. J.* **95**, 5385 (2008).
- [37] X. Xu, T. Meckel, J. A. Brzostowski, J. Yan, M. Meier-Schellersheim, and T. Jin, *Sci Signal* **3**, ra71 (2010).
- [38] T. Kues, R. Peters, and U. Kubitscheck, *Biophys. J.* **80**, 2954 (2001).
- [39] A. del Rio, R. Perez-Jimenez, R. Liu, P. Roca-Cusachs, J. M. Fernandez, and M. P. Sheetz, *Science* **323**, 638 (2009).
- [40] A. M. Pasapera, I. C. Schneider, E. Rericha, D. D. Schlaepfer, and C. M. Waterman, *J. Cell Biol.* **188**, 877 (2010).
- [41] J. D. Humphries, P. Wang, C. Streuli, B. Geiger, M. J. Humphries, and C. Ballestrem, *J. Cell Biol.* **179**, 1043 (2007).
- [42] N. Q. Balaban, U. S. Schwarz, D. Riveline, P. Goichberg, G. Tzur, I. Sabanay, D. Mahalu, S. Safran, A. Bershadsky, L. Addadi, and B. Geiger, *Nat. Cell Biol.* **3**, 466 (2001).
- [43] L. Trichet, J. Le Digabel, R. J. Hawkins, S. R. Vedula, M. Gupta, C. Ribault, P. Hersen, R. Voituriez, and B. Ladoux, *Proc. Natl. Acad. Sci. U.S.A.* **109**, 6933 (2012).
- [44] T. Schmidt, G. J. Schütz, W. Baumgartner, H. J. Gruber, and H. Schindler, *The Journal of Physical Chemistry* **99**, 17662 (1995).
- [45] F. Cichos, V. C. Borczykowski, and M. Orrit, *Current Opinion in Colloid & Interface Science* (2007).

5.7 SUPPLEMENTARY MATERIALS

5.7.1 Relation between variance and squared mean

The second factor in eq. (10) characterizes the joined statistics of the photophysics of the fluorophore and the statistics of labeling of the primary antibody by the secondary antibodies.

$$F = 1 + \frac{\text{var}(n)}{\langle n \rangle^2} = 1 + c_v^2 \quad (\text{s1})$$

It is related to the coefficient of variation c_v of $n = \sigma_n / \langle n \rangle$ in statistics. Values for F vary between 1 and 2 depending on the underlying and dominant statistics.

distribution	mean	variance	F
binomial	$n p$	$n p (1-p)$	$1 + 1/np - 1/n$
Poissonian	λ	λ	$1 + 1/\lambda$
exponential	$1/\lambda$	$1/\lambda^2$	2
Gaussian	μ	σ^2	$1 + \sigma^2/\mu^2$

For all, excluding the exponential distribution, F approaches 1 for large enough n . Exponential statistics would become dominant when single fluorophores are considered. In that case $F = 2$.

5.7.2 Simulation for a combined statistics with secondary antibody labeling

A typical dSTORM experiment involves a dual labeling step where the molecule of interest is first labeled by a highly specific primary antibody, that subsequently is labeled by multiple fluorescence-labeled secondary antibodies. To assess the distribution in this experiment we performed simulations. In those simulations we assumed:

- 1) the number of secondary antibodies bound to a primary antibody is constant, given that all binding sites on the primary antibody will be bound by the excess of secondary antibody.
- 2) the number of fluorophores bound to a secondary antibody is Poissonian distributed with a mean of 4.7 (typical mean value provided by the manufacturer).
- 3) the number of detections per fluorophore follows a single-exponential distribution, typical for photobleaching. The number of detections when a

5.7 Supplementary materials

fluorophore is in the on-state equals $t_{\text{on}} \times \text{framerate}$. Alexa647, as used in the current study is generally assumed to behave according to a four-state molecule characterized by a ground, a fluorescent excited, a non-fluorescent triplet and a long-lived dark state. The latter populated via the excited triplet state [44]. The distribution in such a case is described in terms of a static trap model [45], with on-times following a single exponential distribution.

Figure S1 summarizes the result of this simulation. The factor F (eq. (s1)) is dominated by the number of secondary antibodies. For typical values found in literature as the secondary to primary ratio (4), F is found to be below 1.1. Even in the case of only a single secondary per primary F equals 1.5, still lower than it's maximal value of 2. This is caused by the multiple fluorophores per secondary antibody.

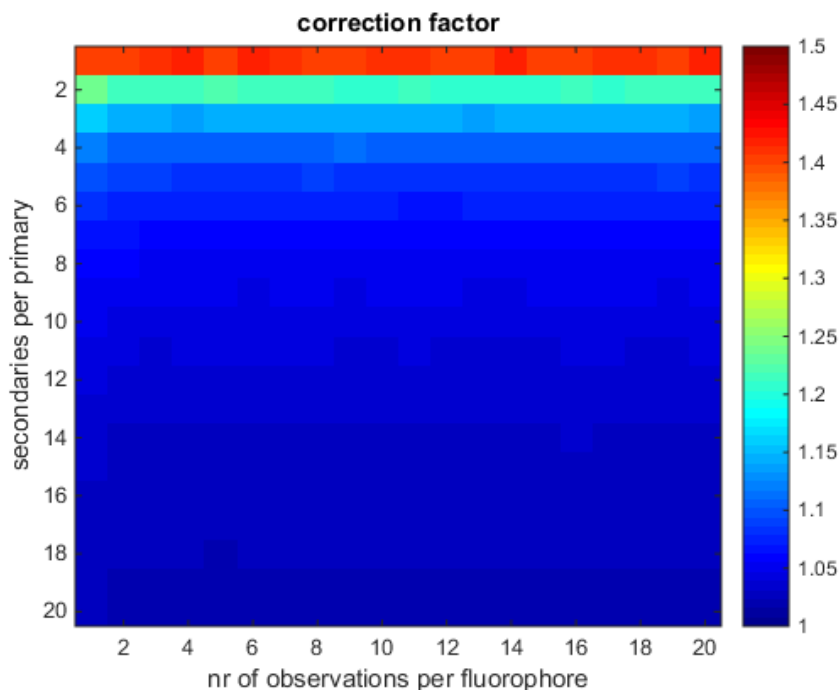


Figure S1: Correction factor F as described in formula S1 for several simulations where the number of observations per fluorophore and the number of secondary antibodies per primary antibody were varied. The number of secondary antibodies per primary dominates the factor F .

5.7.3 Error propagation on squared distances

The squared distance, S , between location i and j is calculated

$$S = (x_i - x_j)^2 + (y_i - y_j)^2 \quad (\text{s2})$$

The error on S is calculated from the errors on the localization

$$dS^2 = \left(dx_i \frac{\partial S}{\partial x_i}\right)^2 + \left(dx_j \frac{\partial S}{\partial x_j}\right)^2 + \left(dy_i \frac{\partial S}{\partial y_i}\right)^2 + \left(dy_j \frac{\partial S}{\partial y_j}\right)^2 \quad (\text{s3})$$

$$\frac{\partial S}{\partial x_i} = \frac{\partial(x_i^2 - 2x_i x_j + x_j^2)}{\partial x_i} = 2x_i - 2x_j \quad (\text{s4})$$

$$dS^2 = 4dx_i^2(x_i - x_j)^2 + 4dx_j^2(x_j - x_i)^2 + 4dy_i^2(y_i - y_j)^2 + 4dy_j^2(y_j - y_i)^2 \quad (\text{s5})$$

$$dS^2 = 4S_x(dx_i^2 + dx_j^2) + 4S_y(dy_i^2 + dy_j^2) \quad (\text{s6})$$

With S_x and S_y the squared distances in x and y respectively.

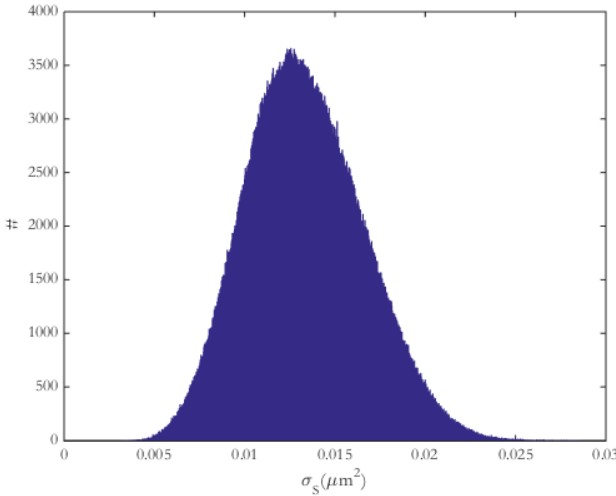


Figure S2: Standard deviation of the calculated squared distances from $0.09 \mu\text{m}^2$ to $0.25 \mu\text{m}^2$ in figure 5B.

SUMMARY

Quantitative Super-Resolution Microscopy

Since the observation of individual fluorescent molecules in the early nineties there has been continuous development in the possibilities to localize single molecules. The wave properties of light however prevent a point-source to be imaged as a perfect point. The resulting image of a point source is called the point-spread-function (PSF). In an optical microscope, the PSF will have the shape of an Airy disk. By fitting the signal, its center can be localized to a high precision, and thus the position of a molecule can be obtained to high precision.

The Airy disk shape of the PSF imposes a limit on the spatial distance at which two point sources can still be spatially separated. This diffraction limit was first stated by Ernst Abbe to be $\lambda/(2 \cdot \text{NA})$, where λ is the wavelength of the emitted light, and NA is the numerical aperture of the optical system. In practice, for two molecules to be observed as individuals, the distance between them must be at least 200 nm. When a random distribution of molecules is assumed, the molecular density must be less than $0.9 \mu\text{m}^{-2}$ to have a smaller than 5% chance of overlapping PSFs. This limit in sampling density in regular single molecule microscopy limits its use as structural imaging tool.

In single molecule localization microscopy (SMLM) only a small subset of molecules is converted into a fluorescent state in which they can be localized as individuals. At high excitation intensity these fluorescent molecules bleach quickly and are no longer fluorescent. By repeatedly converting a small subset of molecules by chemical or photochemical activation into a fluorescent state, all molecules in a sample can be localized to high precision. This process enables a high sampling density and yields high-resolution imaging data.

Chapter 2 demonstrates how SMLM can be used in live cells to look at the spatio-temporal organization of the plasma membrane. The various isoforms of the small GTPase Ras have been shown to organize in different membrane nanodomains. Here, the photoactivatable fluorescent protein mEos2 is used to label the membrane anchor of three different isoforms of the Ras-protein. Live cell SMLM allowed me to image the membrane anchors with a positional

accuracy of 18 nm. Comparison between live-cell and fixed-cell SMLM on the membrane anchor of H-Ras showed broadening of the apparent domain size. I concluded that a domain mobility of $5 \cdot 10^{-4} \mu\text{m}^2/\text{s}$ can quantitatively explain the broadening of the apparent domain size with observation time.

In **Chapter 3** SMLM data was analyzed using particle image correlation spectroscopy (PICS). In PICS the diffusive properties of proteins are extracted from the cumulative squared distance distribution, by analyzing their time-correlated distances. However, in the case of multiple mobilities in the sample, in 3D the fastest fractions will show less correlated distances due to diffusion of molecules out of the focal volume. Here, I developed a method to correct the various fraction sizes. This method I applied to SMLM data from the glucocorticoid receptor (GR). When activated, the GR translocates to the nucleus and binds to the DNA. The correlated distances of the GR in the nucleus can be faithfully described by two fractions, which presumably reflects its bi-modal behavior in the nucleus: a freely diffusing receptor and a DNA-bound receptor. After correction, my analysis showed that over a period of up to 150 ms the fraction size of each population stays constant, proving that there is no exchange between the bound and unbound GR on this time scale.

Chapter 4 shows the result of SMLM on fixed aggregates of α -synuclein. Whereas in the previous chapters I used localization data to obtain information on the dynamic behavior of proteins, in chapter 4 I applied the SMLM technique to obtain super-resolution imaging data. The α -synuclein monomers were directly labeled with an Alexa dye, which allowed me to chemically switch molecules into the fluorescent state. I constructed super-resolution images that showed the spatial distribution of α -synuclein in cells. I was able to follow the uptake of α -synuclein aggregates by the cells and their partial degradation at the molecular level. My results showed the importance of the lysosome-dependent mechanism for protecting cells from exposure to potentially toxic α -synuclein.

In **Chapter 5** I used SMLM to localize vinculin proteins labeled with an Alexa dye in fixed fibroblasts. I combined super-resolution fluorescence imaging with high-resolution cellular force measurements by plating cells on microstructured elastomeric pillar arrays, which provided me with a sensitive force readout. The aim was to correlate the number of vinculin proteins in a focal adhesion protein complex, to the local force generated by the cell via this complex. I developed a robust method to determine the local stoichiometry of molecules by their correlated distances as obtained from SMLM. My analysis yielded a correlation between force and number of vinculin molecules, with a local force increase of 15 pN for each vinculin molecule added to the focal adhesion protein complex.

SAMENVATTING

Kwantitatieve Super-Resolutie Microscopie

Sinds men in de jaren negentig een enkel fluorescerend molecuul kon waarnemen, zijn er continu ontwikkelingen geweest om de positie van fluorescerende moleculen steeds nauwkeuriger te bepalen. Echter, de golfeigenschappen van het licht belemmeren het afbeelden van een puntbron als perfect punt. De afbeelding van een puntbron wordt beschreven door de puntspreidingsfunctie (PSF). In een optische microscoop met ronde openingen heeft de PSF de vorm van een Airyschijf. Door de PSF op de afbeelding te leggen kan het centrum van het signaal gevonden worden met een hoge precisie. Op deze manier kan de positie van het fluorescerende molecuul met hoge precisie worden bepaald.

De vorm van de Airyschijf heeft tot gevolg dat wanneer twee PSF's dicht bij elkaar liggen, ze niet meer van elkaar kunnen worden onderscheiden. Deze diffractielimiet werd voor het eerst beschreven door Ernst Abbe als $\lambda/(2 \cdot NA)$. Hier is λ de golflengte van het uitgezonden licht en NA de numerieke apertuur van het optische systeem. In de praktijk betekent dit dat twee moleculen van elkaar kunnen worden onderscheiden wanneer hun onderlinge afstand meer dan 200 nm bedraagt. Wanneer we een willekeurige verdeling van moleculen veronderstellen op een tweedimensionaal vlak, dan moet de dichtheid van de moleculen kleiner zijn dan $0,9 \mu\text{m}^{-2}$ om minder dan 5% kans te hebben dat PSF's overlappen. Deze limiet in de molecuuldichtheid belemmert het maken van afbeeldingen, omdat te weinig moleculen gelokaliseerd kunnen worden.

Om microscopie met lokalisatie van enkele moleculen (MLEM) mogelijk te maken, wordt een klein deel van de moleculen geconverteerd naar een fluorescerende toestand. Deze worden als enkele moleculen gelokaliseerd. Door ze te exciteren met hoge intensiteit zullen ze snel hun fluorescentie verliezen door een proces dat lichtbleking wordt genoemd. Door herhaaldelijk een klein deel van de moleculen chemisch of optisch te converteren naar een fluorescerende toestand kunnen alle moleculen in het af te beelden object gelokaliseerd worden. Dit maakt het mogelijk een afbeelding te reconstrueren met een zeer hoge resolutie.

Hoofdstuk 2 laat zien hoe MLEM kan worden gebruikt in levende cellen om de organisatie van het plasmamembraan in ruimte en tijd te bestuderen. Het is aangetoond dat verschillende isovormen van het kleine GTP-ase Ras zich organiseren in verschillende membraan nanodomeinen. In deze studie is het fotoactiveerbare eiwit mEos2 gebruikt als label. Hiermee kon ik de positie van het membraananker van drie verschillende isovormen van het Ras-eiwit bepalen met een nauwkeurigheid van 18 nm. Wanneer metingen aan levende cellen werden vergeleken met metingen aan gefixeerde cellen was een verbreding van de waargenomen domeingrootte te zien. Hieruit concludeer ik dat de domeinen in beweging zijn met een diffusieconstante van $5 \cdot 10^{-4} \mu\text{m}^2/\text{s}$. Dit geeft een kwantitatieve verklaring voor de verbreding van de domeingrootte wanneer de domeinen langer geobserveerd worden.

In **hoofdstuk 3** zijn de data van MLEM geanalyseerd met behulp van “particle image correlation spectroscopy” (PICS). Met behulp van PICS worden de diffusieparameters van fluorescerende moleculen gevonden door de distributie van in de tijd gecorreleerde, gesommeerde, kwadratische afstanden te analyseren. Echter, wanneer meer populaties met verschillende diffusie-parameters in drie dimensies diffunderen zal de sneller diffunderende populatie relatief minder tijd-gecorreleerde afstanden laten zien. Dit effect wordt veroorzaakt door diffusie van het molecuul uit het focaal volume. Ik heb een methode ontwikkeld die corrigeert voor dit effect. In dit hoofdstuk pas ik deze methode toe op de MLEM data van de glucocorticoïdreceptor (GR). Bij activatie verplaatst de GR zich naar de celkern en bindt daar aan het DNA. De gecorreleerde afstandsverdeling van de GR in de celkern kan goed beschreven worden met een model voor twee fracties. Dit zou verklaard kunnen worden door het bi-modaal gedrag van de receptor; ofwel ongebonden vrij diffunderend, ofwel gebonden aan het DNA. Na het toepassen van de correctie toont de analyse aan dat gedurende 150 ms de grootte van elke fractie onveranderd is. Dit bewijst dat er geen uitwisseling plaatsvindt tussen de gebonden en de ongebonden fractie van GR op deze tijdschaal.

Hoofdstuk 4 laat de mogelijkheden zien van MLEM op gefixeerde aggregaten van het eiwit α -synucleïne. In de eerdere hoofdstukken werden de localisatiedata gebruikt voor het verkrijgen van informatie over het dynamisch gedrag van eiwitten. In dit hoofdstuk wordt met de localisatiedata een super-resolutie afbeelding gereconstrueerd. De monomeren van α -synucleïne zijn direct gelabeld met een Alexa-fluorofoor die ik chemisch kon schakelen tussen een

fluorescerende en niet- fluorescerende toestand. De door mij gereconstrueerde super-resolutie afbeeldingen toonden de ruimtelijke distributie van α -synucleïne in cellen. Hierdoor was het mogelijk de opname van de aggregaten van α -synucleïne te volgen en hun gedeeltelijke degradatie op moleculair niveau. Mijn resultaten tonen het belang aan van de afbraak via het lysosoom. Dit beschermt de cel tegen de mogelijk toxische invloed van α -synucleïne.

In **hoofdstuk 5** heb ik het eiwit vinculine gelabeld met een Alexa-fluorofoor. Hier worden MLEM data van dit eiwit gecombineerd met krachtmetingen met een hoge resolutie. Bij deze metingen groeien de cellen op elastische micropilaren die vervormen wanneer er kracht op wordt uitgeoefend. Dit gaf de mogelijkheid tot zeer gevoelige bepaling van de kracht die de cel uitoefent. De cel oefent krachten uit op zijn omgeving via het eiwitcomplex dat focale-adhesie wordt genoemd. Het doel was om een correlatie aan te tonen tussen het aantal vinculine-eiwitten in een focale-adhesie enerzijds en de uitgeoefende kracht door de cel anderzijds. Hiervoor heb ik een methode ontworpen waarbij de gecorreleerde afstanden worden gebruikt om de lokale stoichiometrie te analyseren. Mijn analyse toonde de correlatie aan tussen de kracht en het aantal vinculinemoleculen. Per vinculinemolecuul dat werd toegevoegd aan de focale-adhesie vond ik een toename van 15 pN.

PUBLICATIONS

- [1] R. Harkes, V.I.P. Keizer, M.J. Schaaf, and T. Schmidt, Depth-of-Focus Correction in single molecule data allows analysis of 3D diffusion of the glucocorticoid receptor in the nucleus, PLoS ONE 10, e0141080 (2015).
- [2] H. van Hoorn, R. Harkes, E.M. Spiesz, C. Storm, D. van Noort, B. Ladoux, and T. Schmidt, The nanoscale architecture of force-bearing focal adhesions, Nano Lett. 14, 4257 (2014).
- [3] S.H. Askes, N.L.L. Mora, R. Harkes, R.I. Koning, B. Koster, T. Schmidt, A. Kros, and S. Bonnet, Imaging the lipid bilayer of giant unilamellar vesicles using red-to-blue light upconversion, Chem. Commun. (Camb.) 51, 9137 (2015).
- [4] C. Tudor, J. te Riet, C. Eich, R. Harkes, N. Smisdom, J. Bouhuijzen Wenger, M. Ameloot, M. Holt, J.S. Kanger, C.G. Figdor, A. Cambi, and V. Subramaniam, Syntenin-1 and ezrin proteins link activated leukocyte cell adhesion molecule to the actin cytoskeleton, J. Biol. Chem. 289, 13445 (2014).
- [5] M. Apetri, R. Harkes, V. Subramaniam, G.W. Canters, T. Schmidt, and T.J. Aartsma, Direct observation of α -synuclein amyloid aggregates in endocytic vesicles of neuroblastoma cells. (Submitted to PLoS ONE)
- [6] R. Harkes, V.I.P. Keizer, M.J.M. Schaaf, and T. Schmidt, Single molecule study of Ras-membrane domains reveals dynamic behavior. (Submitted to Biophysical Journal)
- [7] R. Harkes, H.E. Balcioglu, E.H.J. Danen, and T. Schmidt, Force sensing and quantitative dstorm on signal transduction proteins inside the integrin adhesome. (In preparation)

CURRICULUM VITAE

Rolf Harkes was born on February 11, 1986 in Wageningen, the Netherlands. He studied Biomedical Engineering at the University of Twente from 2004 to 2010, specializing in biophysics. In 2009 he did his internship at Lambert Instruments in Roden where he worked on the frequency domain fluorescence lifetime imaging attachment LiFA. He joined the group of Prof. dr. Vinod Subramaniam for his master's degree. There he studied the interaction between the actin cytoskeleton and the transmembrane glycoprotein CD166. Förster resonance energy transfer was used to detect changes in fluorescence lifetime. These showed the close proximity of CD166 with mediator proteins Syntenin-1 and Ezrin.

After his graduation in July 2010, Rolf joined the Physics of Life Processes group at Leiden University as a PhD student. Under the guidance of Prof. Thomas Schmidt he worked on the development of super-resolution microscopy by single molecule localization. During his 5 years in Leiden Rolf presented his work at several conferences in the Netherlands, Germany, Spain and the USA. He assisted with different courses such as “physics of life processes 2” and “Experimental Physics”.

As of August 2015, Rolf has started as a high school teacher of physics at the Rijnlands Lyceum in Sassenheim.

ACKNOWLEDGEMENTS

Doing a PhD was a great experience. I have learned a lot about the exciting world of scientific discovery and subsequent communication. At the Physics of Life Processes group the atmosphere has always been one of companionship. Both when I thought myself successful and people would be willing to point out further improvements, and when I was frustrated and people would see opportunity where I saw a failed experiment. The research I have done in the past five years has been a joined effort and I am thankful to many people at Leiden University.

A few people I would like to thank here.

Thomas Schmidt, my supervisor. You have given me the opportunity to work on a project that let me discover the possibilities of single molecule microscopy. Our meetings were always very encouraging and your optimism often helped me to continue improving experimental methods. Sylvie Olthuis, your knowledge of plasmids and cell culture has been essential in my research. Erik Danen and Marcel Schaaf I would like to thank for their helpful discussions on the biological aspects of my thesis.

Hedde van Hoorn, we started our PhD almost at the same time, we worked together on one optical table and together we explored the possibilities of dSTORM. Thank you for all your help and support.

Veer Keizer, you came to me for a little help in using PICS and we ended up writing two papers together. Your enthusiasm for science has been an inspiration and your humor helped me through many dark hours at the microscope.

Mihaela Apetri, thank you for introducing me to α -synuclein and for all the good conversations about kids, jobs, and how fun yet frustrating it all can be.

Wim Pomp, when you started we both wanted to make better microscopy software. Now that I leave we have great software. Working together with you on Labview was a great experience and through joined frustration we always found a solution in the end.

Acknowledgements

Emrah Balcioglu, you helped me with math, chemistry and biology. Never too tired to tell me I was wrong, you always stayed critical in our search of a new molecular counting method. I thank you for the great times we had both in science and in music.

Many thanks for my wonderful colleagues at FvL. The group has been a great place for both social activities and scientific discussions. Dominique, Meng, Lena, Ruth, Bram, Fran-Tso, Anna, Suzanna, John, Ineke, Wietske, Sara, Olga, Artur, Kirsten, Babette, Thomas the Younger, Stefano, Klaas, Joeri and Falko: It has been great to get to know you all.

A special thanks to my students, they did part of the work presented in this thesis. Babette de Jong, Donato Civita, Lucas van der Saag, Elza Lughthart and Floris Stapel.

I would also like to thank the two people who stimulated me to learn and to get where I am today: My parents. You taught me to be curious and always motivated me to keep going. Paula, thank you for all the times we talked about life and science.

Lorijn, thank you for all the times you distracted me with your cries and happy demands. Life is more than work alone. Froukje, you've been my support throughout this PhD and my great love. I dedicate this thesis to you.